Numerical Modelling of Cell Deformation

By Joseph D. Berry

A Thesis submitted to Monash University in fulfillment of the requirements for the degree of

Doctor of Philosophy

Department of Mechanical

& Aerospace Engineering

Monash University

February 2010

TABLE OF CONTENTS

ABSTRACT

This thesis investigates the dynamics of cells in linear shear flow near a plane wall. The first part of the thesis focuses on a two-dimensional model of a tethered cell, to elucidate the effects of cell aspect ratio and cell internal viscosity on cell dynamics. Over the parameter space examined, the cell initially elongates out into the flow, and then slowly pivots towards the wall as the cell relaxes to a steady-state shape. The region of the cell membrane that would come into contact with the wall corresponds with a region of elevated shear stress. The effect of viscosity is found to be negligible at low shear rates, but at high shear rates an increase in internal viscosity leads to an increase in cell deformation and force on the tether. At low shear rates, cells with higher aspect ratios experience less force and deformation. Conversely, at high shear rates cells with higher aspect ratios experience greater force and deformation.

The second part of the thesis presents the results for a three-dimensional model of a single cell moving in close proximity to a wall. The effect of cell height and cell deformability on the dynamics of the cell is determined. The deformability of the cell is controlled by the shear rate, area dilation parameter, and amount of membrane prestress. The shear stress distribution on the vessel wall is described. The presence of a cell has a marked effect on the shear stress distribution, with regions of elevated shear stress apparent both upstream and downstream of the cell. A stiff cell moves slower than a more deformable cell; allowing it to approach the wall more easily. A more deformable cell presents a larger surface to the wall, and creates a larger region of elevated shear stress on the wall immediately upstream.

The effect of the presence of multiple cells on cell dynamics is presented in the third part of the thesis. Cells moving side-by-side have a tendency to move away from one another. The presence of a downstream cell causes the upstream cell to move towards, and below the downstream cell. The presence of a downstream cell also provides a larger region of elevated shear stress on the vessel wall. The presence of multiple cells in the flow increases the slip velocity of both cells markedly, independent of the configuration of the cells.

STATEMENT OF ORIGINALITY

"This thesis contains no material that has been accepted for the award of a degree or diploma in this or any other university. To the best of the candidate's knowledge and belief, this thesis contains no material previously published or written by another person except where due reference is made in the text of this thesis."

Candidate: Joseph Berry

<Submission Date>

ACKNOWLEDGMENTS

Acknowledgments here (don't forget your supervisors!).

CHAPTER 1

INTRODUCTION

1.1 Project Aims

Blood circulates through the body in a closed system of interconnecting blood vessels. Blood vessels range in size from capillaries of diameter 5μm, to arteries of diameter 10mm. The circulating blood contains different types of cells that perform vital functions necessary to sustain life. The most abundant type of cell is the red blood cell, which is primarily responsible for distributing oxygen and removing carbon dioxide from body cells. Blood also contains a class of cells which are responsible for combatting disease, called leukocytes. The smallest cell present in blood, the platelet, is responsible for maintaining the integrity of the vascular system through the arrest of bleeding and the repair of damaged blood vessels.

In order to perform their roles, platelets and leukocytes are required to attach themselves to the vessel wall. The process whereby these cells move from the free-flowing blood to attachment on the vessel wall is called the cell adhesion process. Cell adhesion is a complex, multi-step process, consisting of an interplay of different bonds located on the vessel wall and cell surface. There is considerable evidence to suggest that fluid dynamic forces play a critical role in controlling and influencing the activation of these bonds, and determining when and how the cell approaches the vessel wall. It is also apparent that the deformable nature of cells also plays a critical role in the dynamics of cells and the cell adhesion process.

Numerical modelling can be utilised to provide further insight into the mechanics of cell dynamics and adhesion, and to provide a quantitative and qualitative understanding that cannot be achieved with present measurement techniques. Current models of cells in the literature are highly idealised representations that lack physiological relevance. Therefore, the first aim of this study is to develop a more physiologically consistent

model of a cell.

Recent developments in experimental methods have revealed the existence of platelet and leukocyte tethers that form during adhesion, both *in vitro* and *in vivo*. Of particular interest is the effect of the hydrodynamic forces of blood flow on the formation and deformation of these tethers. Knowledge of the hydrodynamic forces acting on the tethers will help to increase understanding of this complex physical and chemical phenomenon. Current models of tethered cells consider the cell as non-deformable. Hence, another aim of this study is to develop a model of a tethered deformable cell.

It is also apparent that current models of leukocytes and platelets in the literature focus mainly on cells undergoing adhesion. The presence of a cell near a wall creates a disturbance in the flow, which alters the hydrodynamic conditions in the flow. Another aim of this study is to characterise the effect of the hydrodynamic conditions created by the presence of a cell near a wall on the likelihood of adhesion occurring, and to quantify the effect of cell deformation. Hydrodynamic conditions of interest include the velocity of the cell, and the shear stress on the cell and on the vessel wall.

1.2 Thesis Outline

This thesis consists of seven chapters, including the present introduction. Chapter 2 contains a review of the literature relevant to blood cell dynamics and outlines the hypotheses tested in subsequent chapters. Chapter 3 contains the methodology used to obtain the results put forward in this thesis. The following three chapters contain the results. Chapter 4 comprises an investigation of a two-dimensional tethered cell. Chapter 5 presents the results obtained from a model of a three-dimensional cell moving in close proximity to a wall. This model is extended in Chapter 6 to include the effect of two cells moving in a flow near a wall. Finally, the conclusions of the study and the scope for future work are outlined in Chapter 7.

CHAPTER 2

LITERATURE REVIEW

This chapter provides a summary of the current knowledge of cell dynamics and adhesion from a fluid dynamics perspective. A critical analysis of the analytical and numerical models used to shed light on cell dynamics and adhesion is also presented. The first section of this chapter describes the different types of cells present in the circulation system, and outlines some important physical properties of each cell. The second section examines how cells have been modelled and the techniques used. The next section looks at the adhesion process of leukocytes and platelets, and critically analyses the models that have been used to study this phenomenon. The following section describes the dynamics of deformable bodies in unbounded flow, flow bounded by a wall, and flow through a vessel. A critical analysis of the models used to capture deformable body dynamics is also presented. The last section of this chapter contains a summary of the literature review, and presents the hypotheses to be tested in subsequent chapters.

2.1 Cells

Blood consists of a liquid, called plasma, and a suspension of cells that perform functions vital for life. The cells occupy a volume of approximately $40-45\%$ of the total volume of blood. This proportion is known as the haemocrit. There are three types of cells circulating in the blood: red blood cells, leukocytes and platelets.

2.1.1 Red Blood Cells

Red blood cells are non-nucleated, biconcave discs approximately 8μm in diameter, with a thickness of 2μm (Eggleton & Popel 1998) (Figure 2.1). The primary function of these cells is to carry oxygen from the lungs to the body cells, and to transport CO_2 back from the cells to the lungs. The interior fluid of the red blood cell is called the cytoplasm, and is enclosed by a lipid bi-layer membrane. Red blood cells are the most

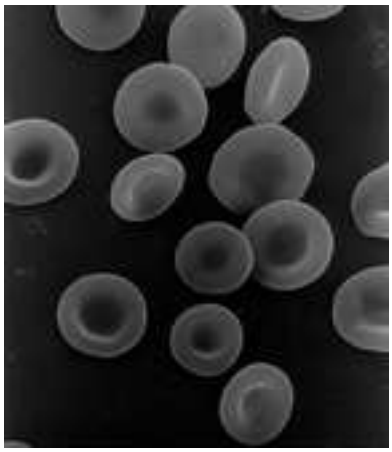

Figure 2.1: Scanning electron micrograph of red blood cells (Byars 1999).

Surface Area	$132 \times 10^{-6}\text{m}^2$	Fung *et al.* (1981)
Volume	$96 \times 10^{-6}\text{m}^3$	Fung *et al.* (1981)
Reduced volume	0.68	Fung *et al.* (1981)
Shear elastic modulus	6×10^{-6} N/m	Waugh & Evans (1979)
Area compressibility modulus	4×10^{-1} N/m	Katnik & Waugh (1990)
Bending modulus	2×10^{-19} N.m	Hwang & Waugh (1997)
Membrane thickness	7.8×10^{-9} m	Hochmuth *et al.* (1983)
Cytoplasm viscosity	$(4 - 17) \times 10^{-3}$ Pa.s	Ross & Minton (1977)

Table 2.1: Mechanical properties of red blood cells.

common cell present in the circulation system, constituting approximately 40% of the total volume.

Deformation of red blood cells is constrained by fixed surface area and fixed volume. Red blood cells display very high resistance to area dilation, with the elastic energies of bending, shear and compression in the ratio of $1 : 50 : 10^6$ (Table 2.1). The biconcave disc shape of the red blood cell means that the ratio of volume to surface area is relatively low, thus maximising surface area for gas transport across the membrane. A measure of this ratio is the reduced volume, defined in equation 2.6 in Section 2.5. A reduced volume of much less than unity indicates that the red blood cell can undergo marked deformation while maintaining a constant surface area.

2.1.2 Leukocytes

Leukocytes are nucleated cells that are formed from stem cells in the bone marrow, and defend the body against infectious organisms and foreign agents. As a consequence, leukocytes are able to adhere to the vessel wall, and pass through the vessel wall, in order to protect the body from infection and disease. Leukocytes occupy less than 1% of

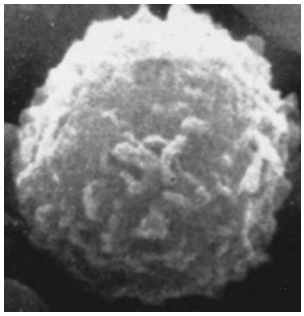

Figure 2.2: Scanning electron micrograph of a leukocyte (Wetzel & Schaefer 1982).

Surface Area	$465 \times 10^{-6}\text{m}^2$	Evans & Yeung (1989)
Volume	$300 - 310 \times 10^{-6}\text{m}^3$	Ting-Beall *et al.* (1993)
Shear elastic modulus	2.4×10^{-6} N/m	Yap & Kamm (2005)
Area compressibility modulus	4×10^{-4} N/m	Needham & Hochmuth (1992)
Bending modulus	2×10^{-18} N.m	Zhelev *et al.* (1994)
Membrane thickness	1×10^{-7} m	Zhelev *et al.* (1994)
Cortical tension	2.4×10^{-5}N/m	Needham & Hochmuth (1992)
Cytoplasm viscosity	$50 - 500$ Pa.s	Peterson & Bronzino (2008)

Table 2.2: Mechanical properties of leukocytes.

the blood's volume. The most common type of leukocyte is the neutrophil, comprising up to 40% of the total number of leukocytes present in the blood. Most of the literature in this area focuses on neutrophils.

In the passive unstressed state, leukocytes are spherical with numerous membrane folds (Figure 2.2). The membrane is highly deformable in shearing and bending, but resists area expansion (Table 2.2). The membrane folds allow the cell to deform without stretching of the cell membrane. Passive leukocytes exhibit viscoelastic properties, and the viscosity of the cytoplasm varies with both deformation and shear rate.

The current understanding of the morphology of a resting leukocyte is that it consists of a cortical shell with constant surface tension enclosing a cytoskeleton and a nucleus immersed in a cytoplasmic non-Newtonian fluid (Kan *et al.* 1998, Tran-Son-Tay *et al.* 1998). During adhesion however, leukocytes undergo an activation process whereby the cytoskeleton rearranges its structure, and the mechanical properties of the cell change (Yap & Kamm 2005).

2.1.3 Platelets

While circulating in the blood, platelets exist in what is called a resting state, the shape of which can be closely approximated as an oblate spheroid with major radius

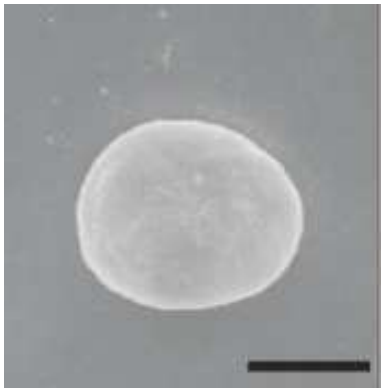

Figure 2.3: Scanning electron micrograph of a platelet (Maxwell *et al.* 2006).

Major Radius	1.5×10^{-6}m	Haga *et al.* (1998)
Minor Radius	0.25×10^{-6}m	Haga *et al.* (1998)
Shear elastic modulus	3×10^{-5} N/m	Haga *et al.* (1998)
Membrane thickness	8×10^{-9}m	Crawford & Taylor (1977)

Table 2.3: Mechanical properties of platelets.

equal to 1.5μm and minor radius equal to 0.25μm (Haga *et al.* 1998) (Figure 2.3). Platelets are responsible for repairing damage to the vessel walls. Circulating platelets will adhere to the vessel wall and form an aggregation plug, called a thrombus, to block the damaged wall section and prevent blood loss. A platelet consists of a plasma membrane supported by a cytoskeleton, which acts as a molecular "strut and girder" system to help maintain the integrity and shape of the resting platelet (Michelson 2002). The cytoskeleton includes a spectrin-based membrane skeleton adherent to the inside of the plasma membrane, a marginal microtubule band, and a sparse rigid actin filament network in the interior of the cell.

The microtubule band resides just beneath the surface membrane of a platelet, along the hemisphere of the disc. The reliance of a platelet on the microtubule band to maintain its discoidal shape was demonstrated by White & Rao (1998). They achieved this by chilling the platelets to 4°C, which resulted in the disassembly of the microtubule band and a corresponding shape change of the platelets to a sphere. When the chilled platelets were rewarmed the microtubule band reassembled and the platelets regained their discoidal shape. Platelets also undergo an activation process, with significant changes in platelet shape and mechanical properties. Table 2.3 provides a summary of the mechanical properties of human platelets.

2.2 Cell Adhesion

A critical function of both leukocytes and platelets is their ability to adhere to the vessel wall. The importance of leukocyte interaction with the vessel wall was first noted by Rudolph Wagner in 1839, as a consequence of the development of intravital microscopy early in the 19th century (Wagner & Frenette 2008). The first evidence of platelet interaction with the vessel wall came later in the 19th century, when the formation of thrombi was observed (Jackson 2007). The adhesion of individual platelets to the endothelium was only documented in 1970 by Begent & Born, due to the relatively small size of the platelet.

The cell adhesion process is extremely complex, and is critically dependent on the shear stress at the vascular wall. For a Newtonian fluid the shear stress is proportional to the shear rate, defined as the velocity gradient of the fluid flow. The shear stress is related to the shear rate by the relation:

$$\tau = -\mu\gamma \tag{2.1}$$

where τ is the shear stress, μ is the viscosity and γ is the shear rate. Typical physiological wall shear rates range from 20s^{-1} in veins to 800s^{-1} in large arteries. Pathological shear rates, caused by vessel blockages called stenoses, can get as high as $10{,}000\text{s}^{-1}$ in stenotic vessels (Kroll *et al.* 1996).

Circulating cells detect damage to vascular walls via surface receptors that recognise exposed sub-endothelial cells. A range of specialised adhesive receptors are inherent in platelets and leukocytes, enabling adhesion to ligands present in damaged vessel walls over a wide range of shear rates. These receptors are responsible for activating cells and for adhering to walls or other cells. Platelets and leukocytes both undergo a similar complex adhesion process, although with different ligand-receptor pairs.

2.2.1 Leukocyte Adhesion Process

Lawrence & Springer (1991) showed that the multistep process by which leukocytes adhere to the vessel wall is initiated by the expression of selectin receptors on the endothelial cells (Figure 2.4). These selectin receptors are characterised by high bond formation rates, resulting in the capture, or initial bond formation, of a leukocyte from the free-flowing blood. These bonds also have high bond rupture rates and as a consequence are short-lived. As a result, the leukocyte "rolls" along the surface,

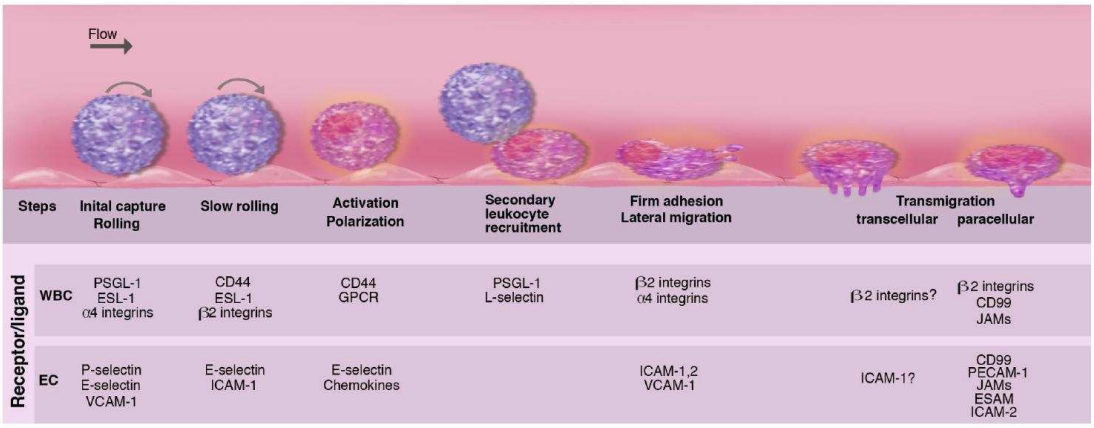

Figure 2.4: The leukocyte adhesion process consists of multiple sequential steps involving different ligand-receptor pairs (Wagner & Frenette 2008). The initial capture of leukocytes is mediated by selectins expressed by the endothelial cells. As the leukocyte rolling velocity decreases, integrin receptors are activated and firm adhesion results. Secondary leukocyte recruitment and cell transmigration through the vessel wall are mediated by other receptor-ligand pairs.

continually forming and breaking bonds, but moving much more slowly than free-flowing cells. Leukocyte rolling velocities have been measured to be in the range of $10 - 40\mu$m/s, and has been found to increase with increasing receptor densities (Lawrence & Springer 1991). Leukocyte adherence decreases with increasing shear rate, with optimal adherence in the shear rate range of $80 - 350$ s^{-1}.

Rolling leukocytes have been observed to detach when the flow is stopped, suggesting that selectin bonds require shear stress to support cell adhesion (Finger *et al.* 1996, Lawrence *et al.* 1997). This observation can be attributed to the catch bond behaviour of selectins, in which the lifetime of the bond increases with increasing shear stress (Marshall *et al.* 2003). This catch bond behaviour allows the leukocyte to bond in regions of high shear, but to move through regions of low shear such as a capillary and thus avoid getting stuck in the smaller vessel.

Firm adhesion of leukocytes is mediated by integrin receptors which are activated during the rolling stage (Lawrence & Springer 1991, Berlin *et al.* 1995). Integrin receptors are characterised by low bond formation and rupture rates. Once the rolling cell has decreased its speed sufficiently, integrin bonds begin to form, and the cell comes to a stable arrest. Integrin-mediated adhesion has been shown to be effective only at shear rates < 80 s^{-1} (Lawrence & Springer 1991).

Membrane tethers have been observed to occur during leukocyte translocation, at shear rates between 50s^{-1} and 800s^{-1} (Schmidtke & Diamond 2000, Ramachandran

et al. 2004) (Figure 2.5). Tethers are long structures that form during adhesion, and appear to involve a significant change to the structure of the cell. Tethers have been observed to last in the order of minutes, and the length and width are significant when compared to the size of the cell. Schmidtke & Diamond (2000) observed tethers of mean length $6\mu m$ in the shear rate range $100-250\text{s}^{-1}$. Ramachandran *et al.* (2004), observed tethers of length $7-12\mu$m and width 2μm at a higher shear rate of 800s^{-1}. The study demonstrated that tether formation coincided with slower, more uniform cell rolling velocities. Larger, more complex tethers formed after longer rolling periods, suggesting that repeated formation and breakage of tethers changes the mechanical properties of the cell.

Heinrich *et al.* (2005) and King *et al.* (2005) used a bio-membrane force probe to extract tethers from leukocytes. Two regimes were found during tether extraction. The initial stages of tether extraction involved a linear elastic extension of the cell membrane. This was followed by a viscous membrane-pulling regime, in which the resistive force of the tether was found to depend on the pulling speed. The transition between the regimes was postulated to be caused by the dissociation of the bond from the cell cytoskeleton.

2.2.2 Platelet Adhesion Process

Savage *et al.* (1996) demonstrated that there are two distinct mechanisms whereby platelets adhere to the endothelial wall (Figure 2.6). At low wall shear rates the adhesion process is governed by the integrin $\alpha_{IIb}\beta_3$ on the platelet surface binding to fibrinogen on the endothelial wall. This process is effective at wall shear rates below $600-900\text{s}^{-1}$ and is immediately irreversible, leading to the conclusion that these bonds have slow bonding kinetics. At higher shear rates, up to 6000s^{-1}, adhesion is critically dependent on the glycoprotein Ibα (GPIbα) binding to von Willebrand Factor (vWF). This interaction is insufficient to firmly adhere the platelets, but allows them to move along the matrix at velocities much slower than bulk flow. The GPIbα-vWF bond acts to slow down the platelet sufficiently so that the $\alpha_{IIb}\beta_3$-fibrinogen bond can form and stably adhere the platelet. An important characteristic of the GPIbα-vWF bond is its rapid formation and dissociation rates, meaning that the platelet moves across the surface as old bonds break and new bonds form. This slow movement across the surface is termed translocation, and is very similar to the rolling of leukocytes observed in ex-

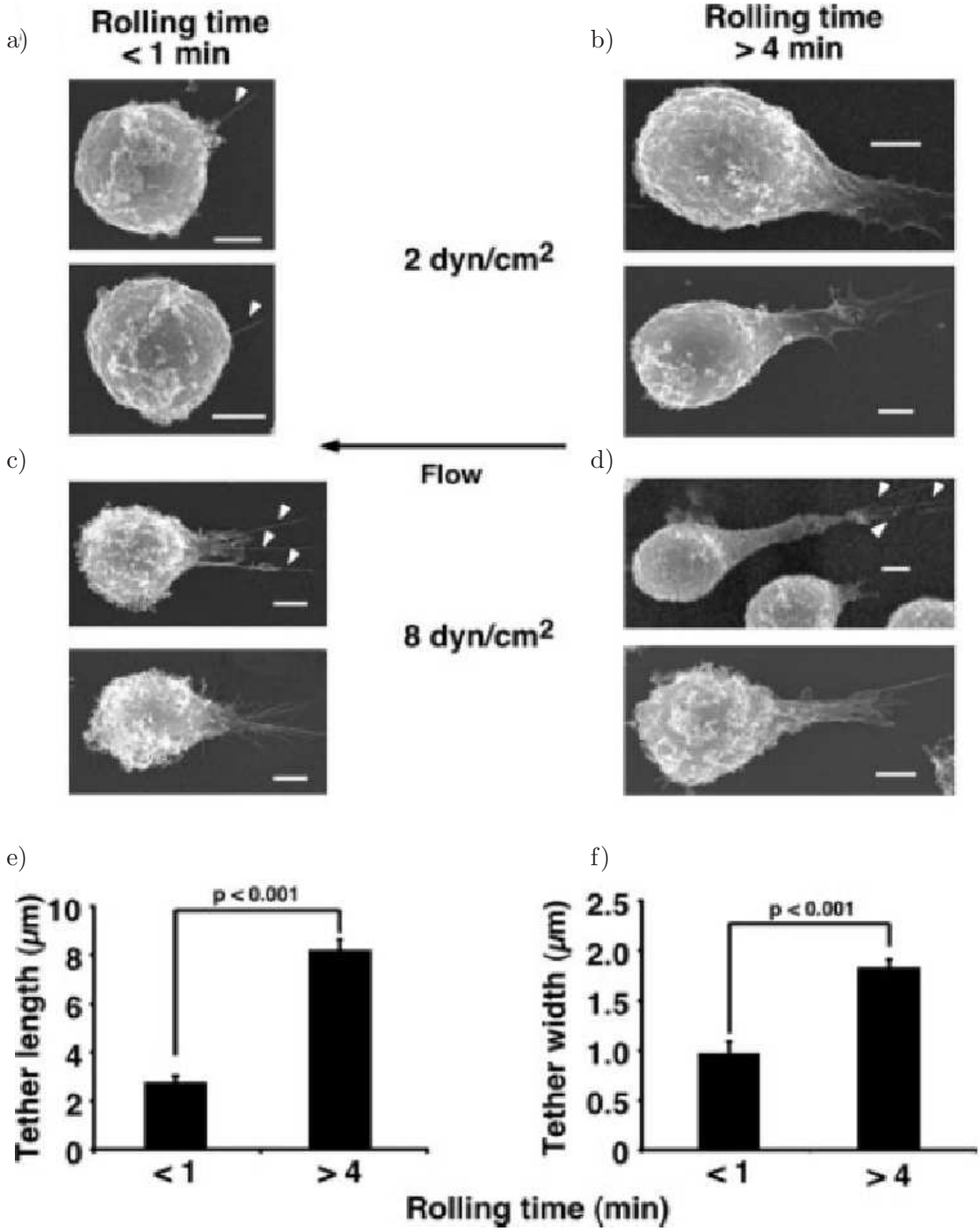

Figure 2.5: Leukocytes observed by Ramachandran *et al.* (2004) undergoing tethering whilst rolling on a P-selectin-infused cover-slip. The leukocytes were rolled for a) < 1 minute at $200s^{-1}$, b) > 4 minutes at $200s^{-1}$, c) < 1 minute at $800s^{-1}$, b) > 4 minutes at $800s^{-1}$. The mean length and width of at least 90 tethers formed at $200s^{-1}$ are shown in e) and f).

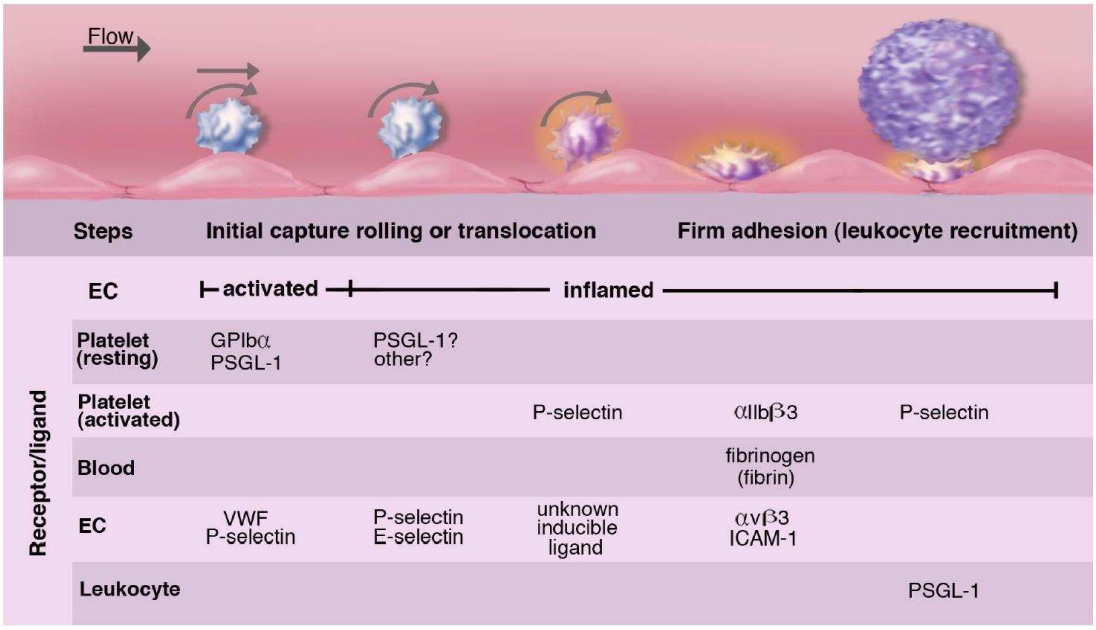

Figure 2.6: The platelet adhesion process is also dependent on multiple sequential steps (Wagner & Frenette 2008). The initial capture of platelets is mediated by vWF receptors expressed by the endothelial cells. Firm adhesion of the platelet is mediated by the $\alpha_{IIb}\beta_3$-fibrinogen bond.

periments both *in vivo* and *in vitro* (Lawrence & Springer 1991). When in the passive state, platelets have been observed to flip, rather than roll, along the endothelium.

As the platelet translocates the cytoskeleton undergoes a transformation called activation. Yuan *et al.* (1999) demonstrated that platelets translocating on vWF undergo cytoskeleton reorganisation that includes the extension of multiple filopodia. These filopodia are dynamic structures that extend from the platelet surface, forming adhesive contacts with the substrate.

Maxwell *et al.* (2006) tested the hypothesis that shape change is the dominant factor in influencing platelet translocation behaviour. It was shown that these morphological changes are critically dependent on the shear rate. At low shear rates the initial shape change involved the extension of tethers and filopodia from the surface of the platelet. At higher shear rates the platelets are spherical and exhibit rolling translocation behaviour similar to leukocytes. An interesting observation of the study was the occurrence of platelet sphereing at very high shear rates in the presence of activation inhibitors, possibly caused by hydrodynamic-induced deformation.

A recent observation in the platelet adhesion process is the presence of membrane tethers being pulled from the surface of the cell (Dopheide *et al.* 2002) (Figure 2.7).

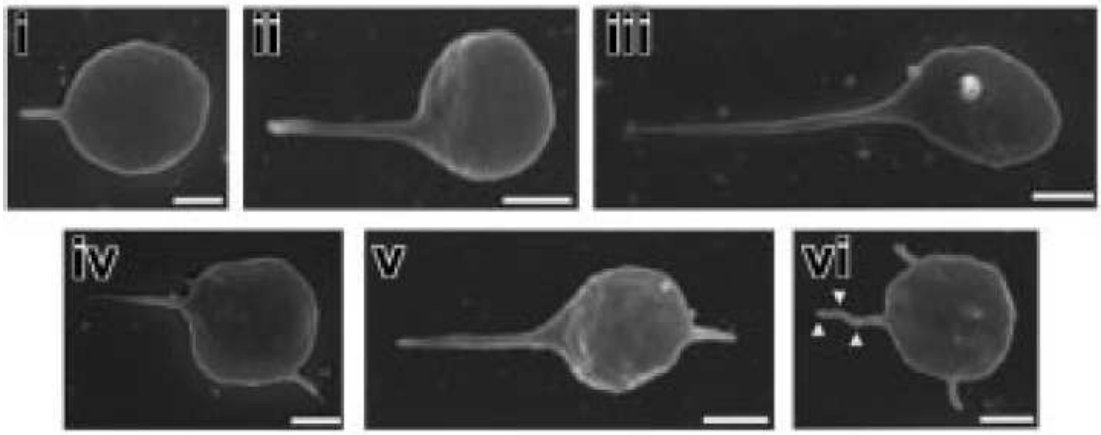

Figure 2.7: Scanning electron micrographs taken by Dopheide *et al.* (2002) of a platelet tether being pulled from the surface of a translocating platelet perfused over a vWF cover-slip at $150s^{-1}$.

Dopheide *et al.* (2002) demonstrated that tether formation is an important factor regulating the dynamics of platelet adhesion. A major finding of the study was that the formation rate, growth rate, size and lifetime of a tether are highly dependent on the shear rate. At a shear rate of $150s^{-1}$ platelets adhered for longer than 10 seconds and a single extension was formed at the trailing edge of the cell, aligned in the direction of the the flow. Less than 5% of platelets formed tethers at $150s^{-1}$, whereas increasing shear rate to $10{,}000s^{-1}$ resulted in nearly all platelets developing tethers. The authors hypothesise that tethering may not be so important at venous shear rates, but could be a critical component of platelet adhesion at high rates of shear.

An important finding of the Dopheide *et al.* (2002) study is that the GPIbα-vWF interaction can support prolonged stationary adhesion through the formation of membrane tethers, despite the inherent rapid kinetics of the bond. Dopheide *et al.* (2002) also established that the platelet tethers were independent of the actin and microtubular parts of the cytoskeleton. They achieved this by treating the platelets with an actin inhibitor, which had only a minimal effect on the formation of tethers.

Nesbitt *et al.* (2009) demonstrated that platelet aggregation is directly regulated by the hydrodynamics of the blood flow. The authors observed that local shear gradients, caused by stenoses or existing thrombii, leads to the development of platelet aggregates. When the platelets were prevented from activating the aggregates continued to form, suggesting that the process is governed primarily by hydrodynamic factors.

2.3 Cell Model Definitions

Models of cells can increase the understanding of cell dynamics whilst circulating or undergoing adhesion. It has been demonstrated in the previous section that the cell adhesion process is an extremely complex multi-step process. It has also been shown that cells consist of complex membranes and, in the case of platelets and leukocytes, an internal structure immersed in a non-Newtonian cytoplasmic fluid. As a consequence, it is necessary to make assumptions in order to numerically model cells. Numerous models, both experimental and numerical, have been used to study cell behaviour. Because the models are so varied, a precise definition of the terms used in the literature is necessary to avoid confusion.

In its simplest form, researchers have considered cells as a *rigid body*. Researchers have also modelled cells as a *drop*, a small volume of liquid bounded by a free surface. Drops exhibit isotropic surface tension, and are prone to breakup under excessive stretching and deformation. Another common cell analogue is a *capsule*. A capsule consists of a body of fluid enclosed in a two-dimensional elastic membrane. In contrast to liquid drops, tensions in an elastic membrane depend on the local strain, not on the local curvature. The tangential stresses present in elastic membranes tend to stabilise the membrane, and breakup is due to mechanical failure. In numerical simulations, the membrane properties are specified using a constitutive strain energy function, which is capable of describing purely elastic, strain hardening, or area incompressible membranes. Skalak *et al.* (1973) defined the strain energy function of a red blood cell based on experimental observations. The elastic tensions in a deformed capsule are formulated by comparing the deformed shape to a reference shape. Typically capsules exhibit minimal resistance to bending. A special type of capsule often studied is the *vesicle*, characterised by an area incompressible membrane, and negligible shear resistance. Vesicles display resistance only to bending. In contrast to capsules, the elastic tensions in the membrane of a vesicle are defined by energy minimisation in numerical simulations. Vesicles are often used to study cell dynamics numerically because of their simple structure and experimentally because of their ease of manufacture.

Analytic models of capsules, vesicles and drops abound in the literature, but are only able to be derived in the small deformation and inertial limits (Leal 1980). Unbounded flow is usually considered, although first order corrections to account for the presence

of a wall are possible. More complicated geometries and large deformations can only be modelled numerically.

Finite element methods and *finite volume methods* have been used previously to model cell dynamics. Both of these methods can be used with a Navier-Stokes formulation where the fluid is treated as a continuum, or with a particle-based method such as the lattice Boltzmann method. Capturing cell dynamics numerically can be very complex since in many cases the boundaries are deformable and move through the computational domain. The cell interface can be tracked implicitly, using a *volume of fluid* or a *level set* method, or explicitly, using an *immersed boundary method*. It is optimal to consider the deformation of a cell with an explicit definition of the exact physical characteristics of the membrane. A major drawback of implicit interface tracking methods is that the interface is not defined, and properties such as curvature and tensions are not able to be extracted. Although the immersed boundary method offers the advantage of an explicit definition of the cell surface, the transferral of properties between the Eulerian and Lagrangian meshes is only accurate to first-order.

The numerical methods outlined above require an Eulerian mesh to describe the computational domain enclosing the cells. *Boundary element methods*, derived from the solution of the Stokes equations, only require the boundaries of the flow to be meshed to determine the motion of the cell. Boundary element methods offer increased computational efficiency because an Eulerian mesh is not necessary. The major drawback of this method is that the effects of inertia are neglected in this method.

Numerical models of cells commonly include either discrete triangulation schemes, structured meshes, or global spectral methods to approximate the cell surface. An unstructured mesh requires averaging over adjacent elements to approximate higher-order quantities such as gradients of tension and curvature. This may lead to smoothing out of any potential instabilities. Structured meshes ensure smoother shapes and stabler computations, however large, singular cell deformations cannot be captured.

2.4 Cell Adhesion Models

The cell adhesion process is still not fully understood. As a consequence it is a very intense area of research. Modelling of the cell adhesion process for leukocytes or platelets can be very useful in determining the primary factors responsible for mediating cell adhesion.

2.4.1 Leukocyte Adhesion Models

Fixed to Surface

The most basic computational studies of leukocyte adhesion examined the drag on bodies fixed to a wall in shear flow. Chapman & Cokelet (1996, 1997, 1998) developed a three-dimensional model to study flow past single and multiple leukocytes adhered to a vessel wall. The studies demonstrated that flow resistance is dependent on the cell to vessel diameter ratio and the number of adherent cells, and that the fluid drag on an individual cell increased as the number of adhered cells increased. Gaver & Kute (1998) calculated the drag on a two-dimensional rigid hemisphere, and showed that drag increased with decreasing vessel size. The models that assume leukocytes are fixed to the wall lack biological relevance due to the dynamic nature of cell adhesion, and neglect the importance of cell deformability.

Adhesion Models

One of the earliest attempts to model a cell, the fluid mosaic model, was proposed by Singer & Nicolson (1972). They modelled the cell membrane as consisting of a phospholipid bilayer containing two classes of proteins. The first type, termed integral proteins, is attached to the underlying cytoskeleton. The second type, termed peripheral proteins, is more loosely attached to the cell. Bell (1978) built upon the fluid mosaic model to provide a means of estimating the rate of bond formation and breakage of bonds between specific molecules. This was the first study to attempt to quantitatively assess the role of specific bonds in mediating cell adhesion. In the study Bell separated the reaction of the ligand and the receptor into two steps. The first step is known as the encounter step, where the ligand and receptor diffuse within bond-forming distance of each other. The second step is termed the reaction step, where a bond forms between the receptor and the ligand.

Dembo *et al.* (1988) extended the work of Bell to develop a model of the physics of cell membrane attachment and reattachment to a surface. Their approach involved coupling the equations of the deformation of an elastic membrane with the bond density kinetic equations developed by Bell. An interesting corollary arising from their model is the existence of catch bonds, which are bonds that do not separate under increasing tension. Catch bonds were validated experimentally by Marshall *et al.* (2003) who showed, using atomic force microscopy, that increasing the force on P-selection bonds

prolonged their lifetime.

A major flaw of the cell adhesion models outlined above is that they are deterministic. This means that a bond is always formed if the distance between the receptor and the ligand is within a specified separation distance. However it is apparent from experimental results that single bond adhesion events are stochastic in nature (Zhu 2000). Receptor-ligand binding has been described as a key-to-lock interaction (Zhu 2000). If the receptor and ligand are not orientated in the correct position no bond will be formed, independent of the distance between the two. Capture of the characteristic "stop and go" cell rolling pattern is not possible using deterministic descriptions of receptor-ligand binding.

A stochastic framework for cell adhesion was first proposed by Cozens-Roberts *et al.* (1990) in an attempt to account for the experimentally observed deviations in deterministic behaviour. In the model the number of bonds formed is described by a discrete, time-varying, random variable which is used to solve a master equation. For simplicity it was assumed that the stresses were distributed evenly over the cell, which leads to the erroneous conclusion that any single bond can keep the cell adhered to the surface regardless of its position along the cell.

An alternative probabilistic model for leukocyte adhesion was used by Hammer & Apte (1992). The leukocyte was modelled as a three-dimensional rigid sphere covered with cylindrical microvilli. The motion of the cell was determined by balancing the hydrodynamic, bonding and colloidal forces and torques at each time step. A Monte Carlo method was used to model the bonds formed between the cell and the vessel wall. Monte Carlo methods allow a system to be sampled in a number of random configurations, which can then be used to describe the system as a whole. An advantage of the Monte Carlo method is that it is easy to implement compared with the master equation method developed by Cozens-Roberts *et al.* (1990), and can be coupled with hydrodynamic equations to provide a more accurate description of cell adhesion. The stochastic method used enabled the model to successfully simulate the experimentally observed jerky motion of rolling cells.

Chang *et al.* (2000) added to the model of Hammer & Apte (1992) to examine the effect of dissociation rate and bond interaction length on the adhesion of a single leukocyte. The study characterised the effect of adhesion biophysical properties on the adhesive dynamics of the cell. The model has also been further developed to include

microvilli deformation (Caputo & Hammer 2005), multiple types of receptors (Bhatia *et al.* 2003), and full spatial resolution of the receptor-ligand bonds (Korn & Schwarz 2008). Caputo *et al.* (2007) examined the shear threshold effect of catch bonds on leukocytes adhering to a surface, and observed the rolling of cells at a shear rate near the threshold of $\sim 100\text{s}^{-1}$. With the shear rate below the threshold, cells were observed to detach and move more quickly

King *et al.* (2005) augmented the model in an attempt to capture the dynamics of leukocyte tethering. A tether was assumed to consist initially of an elastic spring, which then transitioned to a viscoelastic element to simulate cytoskeletal dissociation of the bond. The model was able to capture tether lengths of $\sim 1.5\mu$m. Yu & Shao (2007) included the effect of tether extraction from the vessel wall by considering two linear springs in series.

King *et al.* (2001) and King & Hammer (2001*a*,*b*) extended the work of Hammer & Apte (1992) to examine the hydrodynamic interactions of multiple rolling leukocytes. Slower, more uniform cell rolling became prominent with increasing cell concentration and also decreasing distance between cells.

The adhesion models presented above have been used mainly in an inverse approach to determine single bond parameters from experimental data. Though they are able to replicate many features of cell adhesion, these models fail to capture the deformation of the cell membrane, which has been shown experimentally to play a large roll in cell adhesion.

Deformable Models

Numerous models have been formulated to capture leukocyte morphology. In an attempt to elucidate the dynamics of micropipette aspiration, the leukocyte has been modelled as a Newtonian drop with constant surface tension (Yeung & Evans 1989). Although simple, this model captures some characteristic behaviours of leukocytes undergoing micropipette aspiration (Drury & Dembo 1999). Other models of leukocytes undergoing micropipette aspiration have attempted to capture elastic cytoplasm behaviour using Maxwell fluids or standard linear solid models (Schmid-Schönbein *et al.* 1981, Dong & Skalak 1992).

Models of deformable leukocytes undergoing adhesion include the studies of Dong *et al.* (1999), Dong & Lei (2000) and Lei *et al.* (1999), who modelled the leukocyte as

a two-dimensional viscous liquid drop enclosed in an elastic ring. They demonstrated that as cell deformation increased, drag decreased. Non-physical constraints imposed on the adhesion parameters and initial cell shape limited the effectiveness of this model.

Kan *et al.* (1998, 1999*a*,*b*), Tran-Son-Tay *et al.* (1998), N'Dri *et al.* (2003) and Liu & Wang (2004) studied the effect of the nucleus on deformation using a two-dimensional immersed boundary model of a compound liquid drop. The leukocyte was modelled as a compound drop, with a surface tension interface rather than an elastic membrane. Because of this un-physical simplification the cell shape predictions at large deformations showed poor agreement with experimental results. Yu & Shao (2007) investigated the effect of tether formation on leukocyte adhesion, using a two-dimensional numerical model. The adhesion kinetics used in these models were deterministic, and not able to capture the characteristic "stop and go"nature of the cell rolling pattern.

Three-dimensional deformable models of leukocytes include the work of Jadhav *et al.* (2005), who developed an immersed boundary method simulating a leukocyte as a three-dimensional elastic capsule with stochastic receptor-ligand interaction. It was found that as the cell membrane stiffness increases, the cell-wall contact area decreases, leading to faster and less smooth cell rolling. The model also showed that as membrane stiffness increases, on average fewer bonds per cell form.

Khismatullin & Truskey (2004, 2005) used a volume-of-fluid method with deterministic receptor-ligand interaction to characterise the effects of cell deformability, viscoelasticity and chamber size on leukocyte adhesion, modelling the cell as a compound liquid drop. They compared the results of a Newtonian drop to a viscoelastic drop and showed that without viscoelasticity the cell produced tethers whilst adhering, suggesting that tethers may form due to a failure of the cytoskeleton. Pawar *et al.* (2008) used a three-dimensional model to determine relative importance of cell deformability, microvilli deformability and bonding kinetics on leukocyte recruitment on a surface, finding that more compliant cells rolled at a slower rate compared to stiffer cells. Pappu *et al.* (2008) and Pappu & Bagchi (2008) investigated $O(10)$ leukocytes rolling in parabolic flow in a microchannel using an immersed boundary method, with stochastic receptor-ligand interaction, observing that the cell rolling velocity decreases with separation distance, independent of cell deformability.

2.4.2 Platelet Adhesion Models

Population-type studies of platelets are abundant in the literature, however there is a paucity of models of individual platelets. The first effort at modelling an individual platelet was attempted by Mody *et al.* (2005), who developed a two-dimensional analytical model to describe the flipping motion of a tethered platelet under linear shear flow. They achieved this by decomposing the flipping action into two separate problems: a stationary, rigid inclined fence subjected to shear flow and a flat rigid plate rotating towards a surface in quiescent fluid.

Mody *et al.* (2005) developed an analytical two-dimensional model to determine the motion of a tethered platelet. The platelet was modelled as a thin plate hinged at one end. Good agreement was obtained between the analytical model and experimental results. The authors also implemented a correction factor based on hydrodynamic arguments to account for the slow rotation of the platelet observed to occur near a wall relative to the theoretical results of Jeffery (1922) for an ellipsoidal particle in unbounded shear flow. Pozrikidis (2006) investigated flipping of a platelet modelled as a rigid oblate spheroid along a surface using the boundary element method, demonstrating that the effect of the wall is not as significant as that suggested by Mody *et al.* (2005). The study showed that wall effects alone were not able to explain the slow rotation of platelets observed experimentally, and postulated that a torque arising from cell adhesion to the vessel wall may explain the discrepancy.

2.5 Cell Dynamics

The study of cell dynamics is an extremely active area of research. Rigid particles, drops, capsules, vesicles and cells all display complex behaviour when flowing in unbounded shear flow, or in the presence of boundaries such as walls and channels. The dynamics of drops, capsules and vesicles are governed by the viscosity ratio λ, defined as

$$\lambda = \frac{\mu_2}{\mu_1}, \tag{2.2}$$

where μ_1 is the viscosity of the exterior fluid, and μ_2 is the viscosity of the interior fluid. The dynamics also depend upon the capillary number

$$Ca_D = \frac{\mu_1 U}{\sigma}, \tag{2.3}$$

$$Ca_C = \frac{\mu_1 U}{E}, \tag{2.4}$$

$$Ca_V = \frac{\mu_1 U L^2}{\kappa}, \tag{2.5}$$

where U is the characteristic velocity, L is the characteristic length, σ is the surface tension of the drop, E is the shear modulus of the capsule, and κ is the bending rigidity of the vesicle. The subscripts D, C, and V refer to drop, capsule, and vesicle respectively. The capillary number gives the ratio between the characteristic relaxation time of the body to the time scale of the imposed flow. When the body is not spherical, an extra parameter called the reduced volume ν also governs the dynamics. The reduced volume is defined as

$$\nu = \frac{(4\pi)^{3/2}}{4\pi/3}\frac{V}{S^{3/2}}, \tag{2.6}$$

where V is the volume of the body and S is the surface area of the body. The reduced volume of a sphere is equal to one. Any shape other than a sphere has a reduced volume of less than one.

2.5.1 Unbounded Flow

Jeffery (1922) solved the Stokes equations to determine the motion of a rigid ellipsoid suspended in unbounded shear flow. The resulting particle motion is periodic in nature, and is known as a Jeffery orbit. A Jeffery orbit is characterised by particle rotation about the axis parallel to the vorticity vector. The nature of the Jeffery orbit depends entirely on the initial orientation, the aspect ratio of the particle, and the shear rate.

Red blood cells, vesicles and capsules exhibit rich dynamical behaviour in shear flow. Two types of motion dominate, depending on the ratio of the viscosity of the interior and exterior fluids. It has been shown experimentally that a deformable body with a viscosity ratio of unity suspended in shear flow inclines at a steady angle to the flow, with the membrane rotating about the interior fluid (de Haas *et al.* 1997, Kantsler & Steinberg 2005, 2006). This type of motion is termed tank-treading, and has been widely observed experimentally (Schmid-Schönbein & Wells 1969, Chang & Olbricht 1993, Walter *et al.* 2001). For very low viscosity ratios the capsule bursts at high shear rates (Chang & Olbricht 1993). The burst point is located at the high curvature tip

of the capsule. As the interior fluid becomes more viscous the body begins to tumble, similar to the motion of a rigid body in shear flow described by Jeffery (1922).

Analytic Non-Deformable Models

Keller & Skalak (1982) developed an analytical theory (KS theory) able to explain the tank-treading and tumbling motions of an ellipsoidal deformable body. The body is assumed to be shape-preserving with semi-major and minor axes lengths L and B, and the membrane is assumed to be area incompressible. The authors predict that the time dependent angle $\theta(t)$ between the major axis of the body and the flow direction is governed by the differential equation

$$\dot{\theta} = -\frac{k}{2} - \frac{2LB}{L^2 + B^2}\dot{\phi} + \frac{k}{2}\frac{L^2 - B^2}{L^2 + B^2}cos(2\theta) \tag{2.7}$$

where $\dot{\phi}$ is the tank-treading frequency, given by

$$\dot{\phi} = \frac{kf_3}{f_2 - \lambda f_1}cos(2\theta) \tag{2.8}$$

where f_1, f_2, and f_3 are constants dependent on the ratio L/B. The solution of equation 2.7 predicts tank-treading motion below a critical viscosity ratio λ_c. Above λ_c the tank-treading frequency is zero and the body tumbles. Although able to predict transition from tank treading to tumbling, KS theory is limited by the neglect of shear rate and of cell deformation. KS theory does not capture the transition from tank-treading to tumbling with decreasing shear rate at constant viscosity ratio observed in experiments.

Analytic Deformable Models

Although KS theory provides an accurate description of tank-treading and tumbling at low shear rates, it is less useful when the shear rate is sufficient enough to induce large deformations of the body. At these shear rates, large deformations have been observed experimentally for red blood cells, vesicles and capsules (Abkarian *et al.* 2007). In an attempt to account for the effect of deformation in KS theory, Skotheim & Secomb (2007) introduced an additional term to equation 2.8 representing the effect of the elasticity of the membrane. The model captures the shear-rate transition from tank-treading to tumbling, but is still not able to account for significant deformations of the body.

To account for the effect of the deformation of the body on cell dynamics, many different methods have been used. Researchers have considered analytical models of

small deformations of nearly spherical capsules (Barthés-Biesel 1980, Barthés-Biesel & Rallison 1981). However these analytical models are restricted to small deformations. To capture large deformations, numerical models need to be implemented.

Numerical Models

Capsules undergoing large deformation were initially modelled axisymetrically, using boundary element methods (Li *et al.* 1988, Pozrikidis 1990). These methods were improved upon by extension to three-dimensional boundary-element models, first developed by Pozrikidis (1995) and Zhou & Pozrikidis (1995), and extended by Ramanujan & Pozrikidis (1998). The effect of bending stiffness was included in the boundary element method of Pozrikidis (2001a). Pozrikidis (2003b) improved the method using numerical smoothing on the capsule surface. Lac *et al.* (2007) and Lac & Barthés-Biesel (2008) used a boundary element method to investigate the collision of two elastic capsules in shear flow. Eggleton & Popel (1998) used an immersed boundary method to model spherical, oblate ellipsoidal and biconcave discoidal elastic and Skalak capsules in linear shear flow. The use of an immersed boundary method allowed the authors to include the effects of inertia on the capsule dynamics.

A spectral boundary element method was implemented by Kessler *et al.* (2008) to characterise the orbits of an elastic capsule with bending resistance over a range of viscosity ratios. Tank-treading and tumbling of the cell was observed for different values of shear rate and viscosity ratio. The model was able to predict a transition from tumbling to an oscillatory motion as the shear rate increases sufficiently enough to cause large deformations of the body, previously observed experimentally by Misbah (2006) and Kantsler & Steinberg (2006). This oscillatory motion, sometimes referred to as trembling or vacillating motion, consists of oscillations in the shape and inclination angle of the body.

Lac *et al.* (2004) demonstrated that at low shear rates a buckling instability can be observed in elastic capsules, due to compressive stress acting on the membrane. This instability has not been observed experimentally, suggesting that it may be a direct consequence of neglecting bending resistance. Lac & Barthés-Biesel (2005) managed to suppress this instability by prestressing the capsule membrane, analogous to a pressure difference between the interior and exterior of the capsule. Diaz *et al.* (2000) and Barthés-Biesel *et al.* (2002) compared the effects of different strain energy functions on

the deformation of a capsule in shear flow.

2.5.2 Bounded Flow

The models and observations of cell dynamics outlined above have considered cells in the absence of any boundaries in the flow. To capture more physiologically relevant phenomena, it is necessary to characterise the effect of boundaries on cell dynamics. In arteries, the size of cells is much less than the size of the vessel, and it is sufficient to consider the effect of a single wall on the cell dynamics. In smaller vessels however, it is imperative to study the cell inside an enclosed vessel.

Bodies convected in a flow create a disturbance, which has an effect on the velocity of the body relative to any boundaries present. If inertial effects are considered negligible, it is known that the lateral position, or the distance above a surface, of a solid sphere or a spherical drop does not change (Bretherton 1962). However, the asymmetric deformation of a drop or capsule induced by the flow leads to lateral migration of the drop or capsule even at zero Reynolds number. Both solid and deformable bodies move at a different translational speed relative to boundaries compared to the undisturbed fluid flow. This difference in velocity is defined in the literature as the slip velocity U_{slip}, given by

$$U_{slip} = u^{\infty} - U_{body}, \tag{2.9}$$

where u^{∞} is the undisturbed fluid flow parallel to the boundary, and U_{body} is the velocity of the body parallel to the body.

Presence of a wall

An analytical solution for the slip velocity U_{slip} of a sphere freely suspended in shear flow near a wall was developed by Goldman *et al.* (1967). The solution is given by

$$\frac{U_{slip}}{ka} = \frac{5}{16}\left(\frac{a}{h}\right)^2, \tag{2.10}$$

where k is the shear rate, h is the height above the wall, and a is the radius of the sphere. Pozrikidis (2005*c*) characterised the orbits of freely suspended spheroids suspended in shear flow above a plane wall using a boundary element method. Mody & King (2005) characterised the trajectories of a platelet shaped particle near a wall using a boundary element method, showing that at small particle-wall distances the full orbital motion is suppressed, causing the particle axis to move parallel to the wall. Three distinct regimes

were observed. Platelets further than 1.2 radii from the wall exhibited modified Jeffery orbits. Platelets at heights between 0.75 and 1.1 radii from the wall exhibited flipping behaviour, where the platelet rotated and came into contact with the wall. Platelets at heights below 0.5 radii move in a periodic fashion with the flipping suppressed. The authors found that any initial tilt of the platelet about the flow axis leads to transition to flipping behaviour. The model was extended to investigate the effect of Brownian motion on platelet motion above a wall (Mody & King 2007). Mody & King (2008*a*,*b*) enhanced the model further to investigate the effect of a plane wall on cell-cell collisions, using two ellipsoidal particles. They demonstrated that the presence of a wall in close proximity increases the collision frequency by 25%.

Chaffey *et al.* (1967) determined analytically that the lateral migration U_{migr} of a drop undergoing small deformation decreases inversely with the square of the distance from the wall. Chan & Leal (1979) extended this work to consider drops of arbitrary viscosity ratio. The solution was found to be

$$\frac{U_{migr}}{ka} = Ca_D \left(\frac{a}{h}\right)^2 \frac{3(16+19\lambda)(54\lambda^2+97\lambda+54)}{280(16+16\lambda)(1+\lambda)^2}, \tag{2.11}$$

The slip velocity of a drop undergoing small deformation near a wall was also shown to depend inversely on the square of the distance from the wall (Chan & Leal 1979, Shapira & Haber 1990). The solution is given by

$$\frac{U_{slip}}{ka} = \left(\frac{a}{h}\right)^2 \frac{1+1.5\lambda}{8(1+\lambda)}, \tag{2.12}$$

Uijttewaal *et al.* (1993) and Uijttewaal & Nijhof (1995) used a boundary element method to determine the behaviour of drops undergoing large deformation near a plane wall. They found that at large shear rates, and at close drop-wall distances, the lateral and translational velocities of the drops differ significantly from the analytical predictions.

Olla (1997*b*,*a*) developed an analytical model of a vesicle near a wall in shear flow, and showed that the lateral velocity of the vesicle is of the same form as for a liquid drop. The solution was found to be

$$\frac{U_{migr}}{ka} = C(\nu) \left(\frac{a}{h}\right)^2, \tag{2.13}$$

where C is a constant that depends on the reduced volume of the vesicle. Numerical and experimental studies have confirmed this hypothesis (Sukumaran & Seifert 2001, Abkarian & Viallat 2005). The slip velocity of an elastic body has not been considered in the literature.

Flow in a vessel

Goldsmith & Mason (1962) observed that neutrally buoyant drops suspended in Poiseuille flow through a circular tube rapidly migrated towards the vessel centreline, whereas no migration of rigid spherical particles was observed under the same flow conditions. The existence of lateral migration at very low Reynolds number has also been observed in pulsatile flow (Goldsmith & Mason 1967). There are multiple mechanisms for the lateral migration of a deformable body in a channel, one is due to the hydrodynamic interaction between the body and the wall, another due to interaction between the deformation of the body and the shear rate gradients of the flow (Leal 1980). If the body is not neutrally buoyant then sedimentation also becomes important in determining the rate of body migration. When inertial effects become important, lateral migration of rigid particles has been observed to occur. Segre & Silberberg (1962*a*,*b*) demonstrated that a neutrally buoyant sphere suspended in Poiseuille flow will migrate to an equilibrium position located at 60% of the distance from the centreline to the wall.

When blood flows through vessels less than $\sim 300\mu$m in diameter, complex rheological behaviour has been observed in experiments (Fåhræus 1929, Fåhræus & Lindqvist 1931, Skalak *et al.* 1989). Red blood cells migrate to the centre of the vessel, and consequently move at a higher mean velocity than the mean velocity of the blood (Figure 2.8). This means that the concentration of red blood cells is lower in the vessel than in a larger vessel. This phenomenon is known as the Fåhræus effect (Fåhræus 1929). The distribution of the red blood cells in vessels less than 300μm in diameter causes a cell-free region of fluid to develop next to the vessel wall. This reduces the local viscosity in the region, reducing the resistance to flow (Figure 2.9). This phenomenon is known as the Fåhræus-Lindqvist effect, and has been observed both *in vivo* and *in vitro* (Fåhræus 1929, Goldsmith *et al.* 1989). As the vessel diameter decreases, the apparent viscosity and the cell concentration decrease until the cell diameter and vessel diameter become comparable. As the vessel diameter decreases further, the apparent viscosity and the cell concentration rise due to the occlusion of the vessel by the cells (Secomb 1992). In capillaries, the diameter of a red blood cell or leukocyte is equal to or larger than the diameter of the capillary. Cells are observed to travel in single file through such vessels, with significant deformation from their resting shape (Skalak *et al.* 1989). As the diameter of the vessel widens, the red blood cells form multiple files in the centre of the vessel.

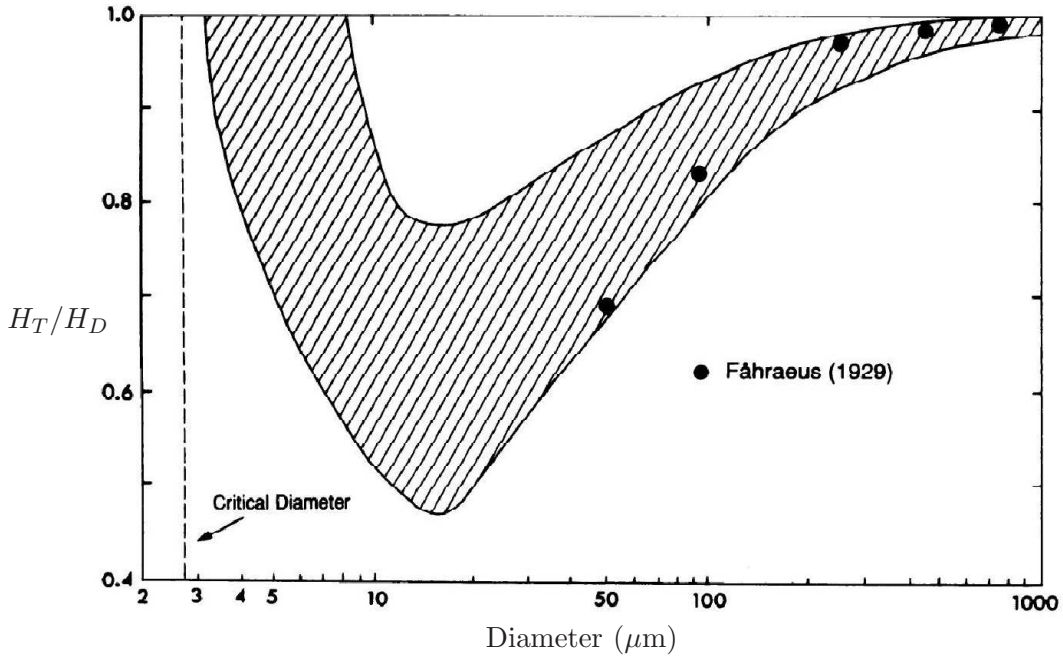

Figure 2.8: Fåhræus effect for red blood cells (Goldsmith *et al.* 1989). H_T is the vessel haemocrit of the cells (percentage of volume occupied by the cells), and H_D is the discharge haemocrit of the cells. The shaded region includes all literature data gathered by Goldsmith *et al.* (1989), and the points indicate the original data of Fåhræus (1929). The critical diameter ($\sim 3\mu$m) is that of the smallest cylindrical vessel through which a red blood cell can flow.

Cells in vessels are not isolated in the fluid, and as such cell-cell interactions play a major role in cell dynamics. The mechanism by which cells approach the vessel wall is caused by the interaction between different cells (Figure 2.10). The presence of red blood cells in the flow push leukocytes and platelets towards the vessel wall, and enhance cell contact with the wall and cell adhesion (Melder *et al.* 2000). This phenomenon is known as margination. Schmid-Schönbein *et al.* (1980) observed 94% margination in a rabbit post-capillary venule of diameter 54 μm. Phibbs (1966) also observed the phenomenon in a much larger vessel of diameter $\sim$ 1mm.

Secomb *et al.* (1986) modelled an axisymmetric cell moving through a capillary using the lubrication approximation of the Navier-Stokes equations. Hsu & Secomb (1989) developed a model of a three-dimensional cell in a capillary using the lubrication approximation. The shape and motion of the cell were prescribed, limiting the effectiveness of the model. A three-dimensional boundary element model of drops moving through a tube was developed by Coulliette & Pozrikidis (1998). Pozrikidis (2005,*a*,*b*) investigated the motion of capsules through capillaries using a three-dimensional boundary

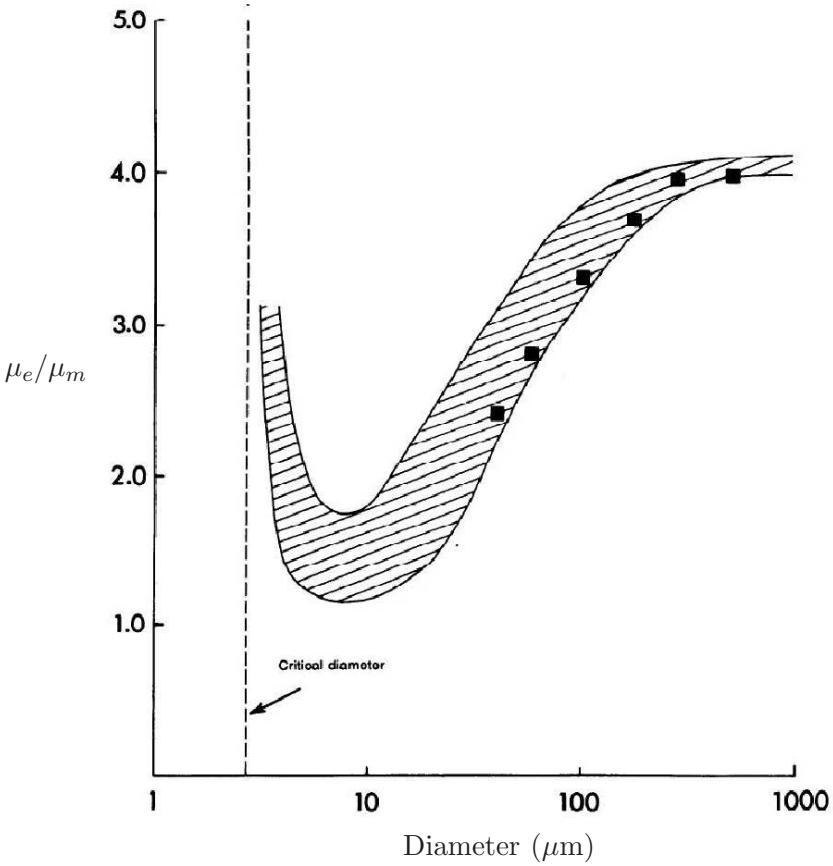

Figure 2.9: Fåhræus-Lindqvist effect for red blood cells (Goldsmith *et al.* 1989). μ_e is the effective viscosity of the suspension, and μ_m is the viscosity of the suspending medium. The shaded region includes all literature data gathered by Goldsmith *et al.* (1989), and the points indicate the original data of Fåhræus & Lindqvist (1931). The critical diameter ($\sim 3\mu$m) is that of the smallest cylindrical vessel through which a red blood cell can flow.

element method. Spherical, oblate ellipsoidal and biconcave elastic capsules were considered, with migration toward the centre-line was observed for all cases. Zhou *et al.* (2007, 2008) studied the transport and deformation of a leukocyte in capillaries and through a contraction with axisymmetric Newtonian and viscoelastic drop models, using an immersed boundary lattice Boltzmann model. The lateral migration of an elastic capsule in a channel was studied by Doddi & Bagchi (2008), using a front-tracking immersed boundary method. The migration velocity of the cell was observed to increase with capillary number and capsule to channel size ratio, but decrease with increasing viscosity ratio.

Sun *et al.* (2003), Sun & Munn (2005) developed a two-dimensional lattice Boltzmann approach to simulate the flow of red blood cells and leukocytes in a vessel. Simulation results obtained using this model suggest that the capillary to venule diameter

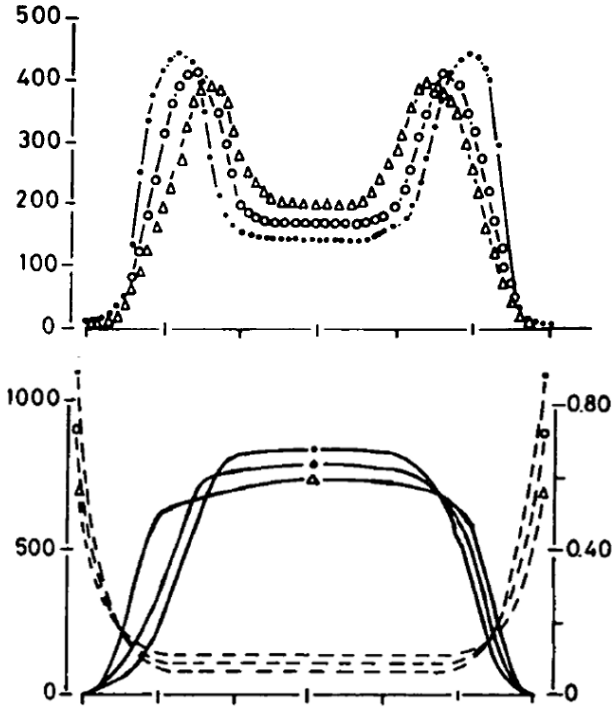

Figure 2.10: Margination of platelets due to the presence of red blood cells in the flow, as observed by Aarts *et al.* (1988). The top figure shows the concentration of platelets as a function of radius in a circular vessel, for three different shear rates. The bottom figure shows the concentration of platelets (dashed lines) in the presence of red blood cells (solid lines).

ratio, cell configuration, and cell shape are critical determinants of the initiation of cell rolling in post-capillary venules. The model was also used to predict that an optimal configuration of the trailing red blood cells is required to drive the white blood cell to the wall.

Bagchi (2007) developed a two-dimensional immersed boundary model of $O(1000)$ red blood cells in a channel. Zhang *et al.* (2007) and Fruend (2007) investigated leukocyte margination in microvessels in the presence of red blood cells using two-dimensional immersed boundary models. Fruend demonstrated that aggregation of red blood cells is not a necessary condition for margination to occur, suggesting that a mismatch of cell size or shape may be primarily responsible. Secomb *et al.* (2007) used a two-dimensional finite-element method to study red blood cell motion in microvessels. The red blood cells were modelled as a set of interconnected viscoelastic elements with incorporated bending resistance. Cell trajectories and shapes compared favourably to experimental data obtained in a rat microvessel (Figure 2.11). Lateral migration away from the wall was observed to occur, caused by the asymmetry in cell shape.

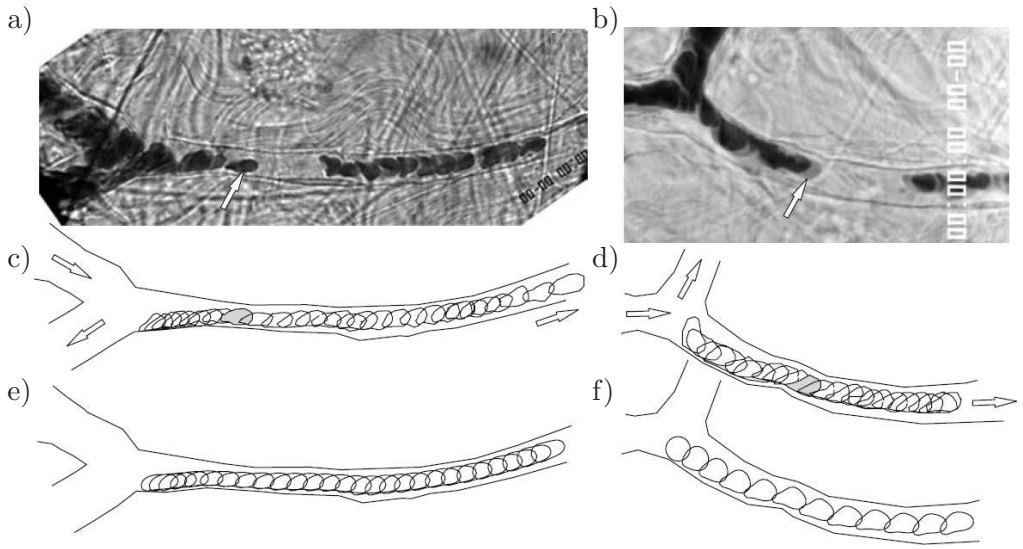

Figure 2.11: Observations and simulations by Secomb *et al.* (2007) of red blood cell trajectories in microvessels. Individual images of the microvessels selected for observation are shown in a) and b), with arrows indicating which red blood cell was tracked. The digitised outlines of the vessel wall and the position of each cell at intervals of 10ms and 20ms respectively are shown in c) and d). The corresponding simulations of a cell moving in a microvessel with the same shape as the experiments are shown in e) and f).

Dupin *et al.* (2007) developed a three-dimensional lattice-Boltzmann method able to model $O(100)$ red blood cells in a capillary. Doddi & Bagchi (2009) developed a three-dimensional immersed boundary method able to model $O(100)$ red blood cells moving in a microvessel. The study yielded a three-layer model of blood flow able to quantitatively predict the size of the cell-free region caused by the Fåhræus effect.

2.6 Summary and Hypotheses

It is apparent from the review of the literature that the modelling of cell behaviour has advanced significantly in the past twenty years with the advent of ever cheaper and faster computational equipment. There are numerous analytical and numerical techniques available to investigate cell dynamics. The adhesion models outlined in this chapter are capable of modelling multiple adhering cells, and are able to capture the essential characteristics of cells moving across a surface. The models of the bonding kinetics rely on empirical measurements of adhesion properties. The models of cell dynamics analysed in this chapter are able to model multiple cells in different types of geometries.

Current models lack the ability to accurately capture specific morphological changes

that cells undergo during the adhesion process. These morphological changes, such as tethering, have been shown to affect the cell's ability to adhere to the vessel wall. Cells have also been shown to actively change their internal structure, leading to a large change in mechanical properties. The amount of deformation of the cell affects the size of the disturbance created by the cell, and this in turn affects the hydrodynamic properties relevant for successful adhesion.

Many different methods have been used to model the cell membrane. Some studies model the cell as area-incompressible, others as purely elastic. Leukocytes are often modelled as compound, non-Newtonian liquid drops. The amount of cell deformation can be controlled by varying the extent of membrane area-incompressibility or membrane prestress. The choice of membrane type affects the way the cell deforms, because the relationship between the flow and the cell deformation is coupled and non-linear. Characterisations of the effect of membrane choice on cell dynamics exist in the literature for unbounded flows, but not in a bounded flow. It would therefore be of interest to determine the effect of cell deformation on the cell dynamics in a bounded flow, and to quantify how cell deformation affects the cell's ability to adhere to the surface.

It is apparent that the numerical models reviewed in this chapter have concentrated mainly on the dynamics of the cell itself. It is also clear that the wall plays an important role with regard to cell adhesion. Receptors on the cell and ligands present on the vessel wall both need to be activated for adhesion to occur. The disturbance created by the presence of a deforming cell in the flow will have an effect on both the shear stress present on the cell and on the vessel wall. The effect of the presence of a cell on the wall shear stress is often overlooked in the literature.

Numerous studies exist in the literature addressing the effect of deformation on the lateral migration, but less emphasis is placed on the slip velocity of the cell. It is clear that the slip velocity of a cell is important in terms of cell adhesion. It is advantageous for a cell to be moving slowly relative to bonds on the vessel wall to enhance the probability of cell adhesion. Analytic derivations and numeric studies of the slip velocity of a rigid sphere and a liquid drop can be found, but no analogous investigation of an elastic body exists.

These shortcomings in current models can be used to formulate hypotheses to be tested in this thesis.

2.6.1 Hypothesis 1

The models of tethered cells in the literature have focused solely on a solid sphere connected to an elastic tether (King *et al.* 2005, Yu & Shao 2007). It is clear however from the observations of Ramachandran *et al.* (2004) and Dopheide *et al.* (2002) that a cell can undergo significant overall deformation when tethered, and this would play a significant role on the dynamics of the cell. The tethered cell models developed have not considered tethering platelets, which are discoidal, and it would be of interest to determine the effect of cell aspect ratio on the tethered cell dynamics. Hence, the first hypothesis is that *the dynamics of a tethered cell are affected by the aspect ratio and the internal viscosity of the cell.*

2.6.2 Hypothesis 2

There is strong evidence to suggest that cells change their mechanical properties during the adhesion process. Yap & Kamm (2005) demonstrated that the shear modulus of a leukocyte changes significantly upon activation, meaning that activated cells undergoing adhesion are more deformable than passive cells. Long membrane extensions called tethers have been observed with adhering leukocytes and platelets (Schmidtke & Diamond 2000, Dopheide *et al.* 2002). Ramachandran *et al.* (2004) showed that tethering leukocytes form longer and wider tethers as rolling time increases due to weakening of the cell structure. It is therefore of interest to quantify the effects of cell deformation on the dynamics of a deformable cell near a wall. Thus, it is predicted that *an easily deformable cell creates hydrodynamic conditions amenable for cell adhesion.*

2.6.3 Hypothesis 3

There is evidence to suggest that the presence of another cell improves the cell adhesion process. King *et al.* (2001), King & Hammer (2001*a*,*b*) and Pappu & Bagchi (2008) demonstrated that slower, more uniform cell rolling existed when multiple cell adhesion was considered for both rigid and deformable cells. These studies focused on adhering cells, not on the hydrodynamic conditions in the lead up to adhesion. It would be of interest to characterise the hydrodynamic effect of multiple deformable cells moving in the presence of a plane wall. Therefore the third hypothesis is that *the presence of multiple cells creates hydrodynamic conditions amenable for cell adhesion.*

CHAPTER 3

METHODOLOGY

This chapter provides an overview of the computational methods used for the simulations conducted for this thesis. The first section will outline the problem, and discuss the assumptions made. Following this, the governing equations and boundary conditions for the two-phase flow of a cell suspended above a wall will be presented. The next section will present a boundary integral formulation of the problem, followed by sections containing a discussion of the techniques used to discretise the boundary integral equations in both time and space. The following section defines the metrics used to quantify the dynamics of the cell. For brevity, the sections on the boundary integral formulation, the numerical methods and the metrics will present only those relevant to the three-dimensional model. The corresponding two-dimensional equations, techniques and metrics are presented in Appendix A. The final section contains the convergence and validation studies carried out in order to confirm the validity and accuracy of the methods presented.

3.1 Problem Statement & Assumptions

As a first approximation, a blood cell can be modelled as an elastic capsule containing a Newtonian fluid of viscosity $\lambda\mu$, suspended in a Newtonian fluid of viscosity μ (Eggleton & Popel 1998, Pappu *et al.* 2008, Pozrikidis 2003*a*). The interior domain is defined as V, and the exterior domain as Ω (Figure 3.1). The interior and exterior domains are separated by the cell interface S. The thickness of the cell membrane is assumed to be negligible, hence the interface can be treated as a two-dimensional elastic sheet. This implies that all elastic stresses are in the plane of the membrane. The local curvature radius is assumed to be much larger than the thickness of the membrane, meaning that bending resistance can be neglected. The membrane is also assumed to be transversely

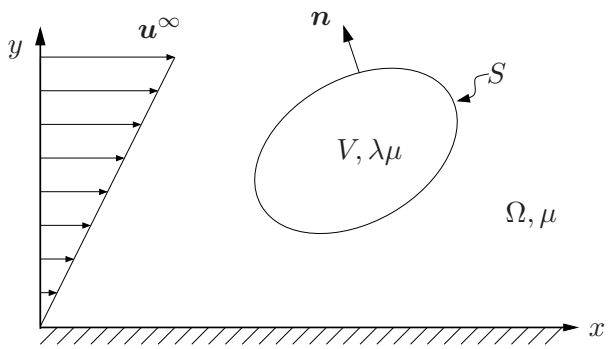

Figure 3.1

isotropic, or unchanged by rotations about the unit normal $\boldsymbol{n}$ in its local plane surface.

A major assumption made is that the size of the blood vessel is much greater than the size of the blood cell. Typical blood vessel sizes range from capillaries of diameter $O(10^{-6})$m to arteries of diameter $O(10^{-2})$m. Given that all blood cells are of size $O(10^{-6})$m, this is a reasonable assumption for most types of blood vessels, but not capillaries. This assumption allows the ambient flow $\boldsymbol{u}^\infty$ through a vessel to be approximated as linear shear flow over a plane wall. This can be written as

$$\boldsymbol{u}^\infty = (ky, 0, 0), \tag{3.1}$$

where k is the shear rate.

The cell is assumed to be neutrally buoyant, with negligible gravitational effects. The validity of this assumption can be tested by dividing the characteristic Bond number by the characteristic capillary number. The Bond number measures the relative importance of gravitational forces to elastic forces, whereas the capillary number measures the relative importance of viscous forces to elastic forces. Thus, the division of the Bond number with the capillary number yields

$$\frac{Bo}{Ca} = \frac{g\Delta\rho L^2/E}{\mu U/E} = \frac{g\Delta\rho L^2}{\mu U}, \tag{3.2}$$

where g is the gravitational constant, U is the characteristic velocity, $\Delta\rho$ is the difference in density between the fluid and the cell, L is the characteristic length, and μ is the fluid viscosity. Equation 3.2 yields a dimensionless number measuring the relative importance of gravitational forces to viscous forces. With g of $O(10)$kg.m/s^2, a density difference of $O(10^{-4})$kg/m^3 (Ratner *et al.* 1996), the characteristic length as the cell diameter of $O(10^{-6})$m, μ of $O(10^{-3})$Pa.s, and characteristic velocity of blood in an

artery of $O(10^{-6})$m, Equation 3.2 yields a Bo/Ca of $O(10^{-2})$. This indicates that the gravitational effects can be ignored when considering physiological cell dynamics.

Typical biological flows are characterised by extremely high viscous force effects relative to the influence of inertial forces. This ratio is measured by the Reynolds number, defined as

$$Re = \frac{\rho U L}{\mu} \tag{3.3}$$

where ρ is the density of the fluid, U is the characteristic velocity, L is the characteristic length and μ is the viscosity. A typical Reynolds number for cell adhesion in a blood vessel can be calculated, with the characteristic length as the cell diameter of $O(10^{-6})$m, the characteristic velocity of blood in an artery of $O(10^{-2})$m/s, density of blood plasma of $O(10^{3})$kg/m^3, and viscosity of blood plasma of $O(10^{-3})$Pa.s (Mody & King 2005). This leads to a Reynolds number of $O(10^{-2})$, highlighting that inertial effects can be considered negligible when considering physiological cell dynamics.

3.1.1 Governing Equations

If inertial effects are considered negligible, then the flow in the exterior and interior of the cell is governed by the Stokes flow equations (Leal 1992)

$$\mu \nabla^2 \boldsymbol{u} = \boldsymbol{\nabla} p, \qquad \boldsymbol{\nabla} \cdot \boldsymbol{u} = 0, \tag{3.4}$$

$$\lambda \mu \nabla^2 \hat{\boldsymbol{u}} = \boldsymbol{\nabla} \hat{p}, \qquad \boldsymbol{\nabla} \cdot \hat{\boldsymbol{u}} = 0, \tag{3.5}$$

where $\boldsymbol{u}$ and p are the velocity and pressure fields in the exterior domain Ω, $\hat{\boldsymbol{u}}$ and $\hat{p}$ are the velocity and pressure fields in the interior domain V, and λ is the viscosity ratio of the interior to exterior fluid.

The boundary conditions are such that the velocity is continuous across the interface, and that the normal stress at the interface is balanced by elastic tensions in the membrane. The first condition gives

$$\boldsymbol{u} = \hat{\boldsymbol{u}}, \qquad x \in S. \tag{3.6}$$

The second condition can be written as (Pozrikidis 2001*b*)

$$\Delta \boldsymbol{f} = (\boldsymbol{\sigma} - \hat{\boldsymbol{\sigma}}) \cdot \boldsymbol{n} = (\boldsymbol{I} - \boldsymbol{nn}) \cdot \boldsymbol{\nabla} \cdot \boldsymbol{T}, \tag{3.7}$$

where $\boldsymbol{\sigma}$ is the stress tensor, $\Delta \boldsymbol{f}$ is the stress discontinuity across the interface, $\boldsymbol{n}$ is the unit normal vector to the interface pointing into the exterior fluid, $\boldsymbol{T}$ is the membrane tension tensor, and $\boldsymbol{I}$ is the identity tensor. The term $(\boldsymbol{I} - \boldsymbol{nn}).\boldsymbol{\nabla}$ is the surface divergence operator.

3.2 Boundary Integral Equation

The boundary integral equation is formed by seeking solutions to the singularly forced Stokes flow equations (Pozrikidis 1992)

$$\mu\nabla^2\boldsymbol{u} = \boldsymbol{\nabla}p - \boldsymbol{g}\,\delta(\boldsymbol{x}-\boldsymbol{x}_0), \qquad \boldsymbol{\nabla}\cdot\boldsymbol{u} = 0 \tag{3.8}$$

where δ is the three-dimensional delta function, $\boldsymbol{x}$ is the observation point, $\boldsymbol{x_0}$ is the source point, and $\boldsymbol{g}$ is an arbitrary constant vector. By introducing the velocity Green's function G_{ij} and the stress Green's function T_{ijk}, the solution to equation 3.8 can be written as (Pozrikidis 1992):

$$u_i(\boldsymbol{x}) = \frac{1}{8\pi\mu}G_{ij}(\boldsymbol{x},\boldsymbol{x}_0)g_j \tag{3.9}$$

$$\sigma_{ik}(\boldsymbol{x}) = \frac{1}{8\pi}T_{ijk}(\boldsymbol{x},\boldsymbol{x}_0)g_j \tag{3.10}$$

Physically, equation 3.9 and equation 3.10 express the flow field produced by a concentrated point force of strength $\boldsymbol{g}$ located at source point $\boldsymbol{x}_0$. The form of the Green's function depends upon whether the fluid is bounded or unbounded. For an unbounded fluid, the Green's functions can be shown to be (Pozrikidis 1992):

$$G_{ij}^{FS}(\boldsymbol{x},\boldsymbol{x}_0) = \frac{\delta_{ij}}{r} + \frac{\hat{x}_i\hat{x}_j}{r^3} \tag{3.11}$$

$$T_{ijk}^{FS}(\boldsymbol{x},\boldsymbol{x}_0) = -6\frac{\hat{x}_i\hat{x}_j\hat{x}_k}{r^5} \tag{3.12}$$

where $\hat{\boldsymbol{x}} = \boldsymbol{x} - \boldsymbol{x}_0$ and $r = |\hat{\boldsymbol{x}}|$.

Other Green's functions have been derived, including those for flow in a semi-infinite domain bounded by an infinite plane wall. These are included in Appendix B.

Using equation 3.9, equation 3.10 and the Lorentz reciprocal relation the boundary integral representation for Stokes flow can be derived (Pozrikidis 1992):

$$\begin{aligned} u_j(\mathbf{x}_0) = -\frac{1}{8\pi\mu}\int_S f_i(\boldsymbol{x})G_{ij}(\mathbf{x},\mathbf{x}_0)dS(\mathbf{x}) \\ + \frac{1}{8\pi}\int_S^{PV} u_i(\mathbf{x})T_{ijk}(\mathbf{x},\mathbf{x}_0)n_k(\mathbf{x})dS(\mathbf{x}) \end{aligned} \tag{3.13}$$

where the traction $\boldsymbol{f}$ is defined as $\boldsymbol{\sigma}\cdot\boldsymbol{n}$. The first and second integrals on the RHS of equation 3.13 are known as the single-layer and double-layer integrals respectively. Depending on the type of boundary conditions specified, equation 3.13 can be used to either describe the disturbance velocity caused by a body of any shape that exerts a nonzero force in a fluid or to describe the hydrodynamic force acting on an arbitrarily

shaped body. Specifying the boundary distribution of the velocity $\boldsymbol{u}$ reduces equation 3.13 to a Fredholm equation of the first kind for the traction $\boldsymbol{f}$. Specifying the boundary distribution of the traction $\boldsymbol{f}$ yields a Fredholm equation of the second kind for the velocity $\boldsymbol{u}$.

When considering linear shear flow past a deformable interface, equation 3.13 can be used to derive the integral (Pozrikidis 1992):

$$\begin{aligned} u_j(\mathbf{x}_0) = \frac{2}{1+\lambda} u_j^{\infty}(\mathbf{x}_0) - \frac{1}{4\pi\mu_1(1+\lambda)} \int_S \Delta f_i(\mathbf{x}) G_{ij}(\mathbf{x},\mathbf{x}_0) dS(\mathbf{x}) \\ + \frac{1-\lambda}{4\pi(1+\lambda)} \int_S^{PV} u_i(\mathbf{x}) T_{ijk}(\mathbf{x},\mathbf{x}_0) n_k(\mathbf{x}) dS(\mathbf{x}) \end{aligned} \tag{3.14}$$

where μ_1 is the external fluid viscosity, μ_2 is the internal fluid viscosity, and λ is the viscosity ratio μ_2/μ_1.

The type of interface is determined by the specification of the force balance at the surface, denoted by $\Delta f_i(\mathbf{x})$ in equation 3.14. The derivation and calculation of the force balance is discussed in detail in section 3.5.

Non-dimensionalising equation 3.14 with length scale L, velocity scale kL, and stress scale E/L, leads to

$$\begin{aligned} u_j^*(\mathbf{x}_0^*) = \frac{2}{1+\lambda} u_j^{\infty *}(\mathbf{x}_0^*) - \frac{1}{4\pi(1+\lambda)Ca} \int_S \Delta f_i^*(\mathbf{x}^*) G_{ij}^*(\mathbf{x}^*,\mathbf{x_0}^*) dS^*(\mathbf{x}^*) \\ + \frac{1-\lambda}{4\pi(1+\lambda)} \int_S^{PV} u_i^*(\mathbf{x}^*) T_{ijk}^*(\mathbf{x},\mathbf{x_0}^*) n_k^*(\mathbf{x}^*) dS^*(\mathbf{x}^*) \end{aligned} \tag{3.15}$$

where Ca is the capillary number, and E is the elastic shear modulus of the membrane. The superscript * denotes a dimensionless quantity. From hereafter non-dimensionality will apply to all quantities, and the superscript will not be used.

The evolution of the cell interface is governed by the elastic capillary number Ca, representing the ratio of viscous forces to elastic forces, and the viscosity ratio λ. The Capillary number Ca can be considered as the dimensionless shear rate, and is defined as:

$$Ca = \frac{\mu k L}{E}. \tag{3.16}$$

3.3 Surface Discretisation

The initial cell interface S is described by a set of N_P marker points, and the surface of the membrane is approximated with an unstructured mesh of N_E quadratic triangular elements, each uniquely defined by three edge nodes and three vertex nodes. The

Mesh coefficient	N_E	N_P
0	20	42
1	80	162
2	320	642
3	1280	2562
4	5120	10242
n	$20(4^n)$	$2N_E + 2$

Table 3.1: Number of points and elements created by subdividing each face of an icosahedron and projecting radially onto a sphere. N_E is the number of elements, and N_P is the number of points.

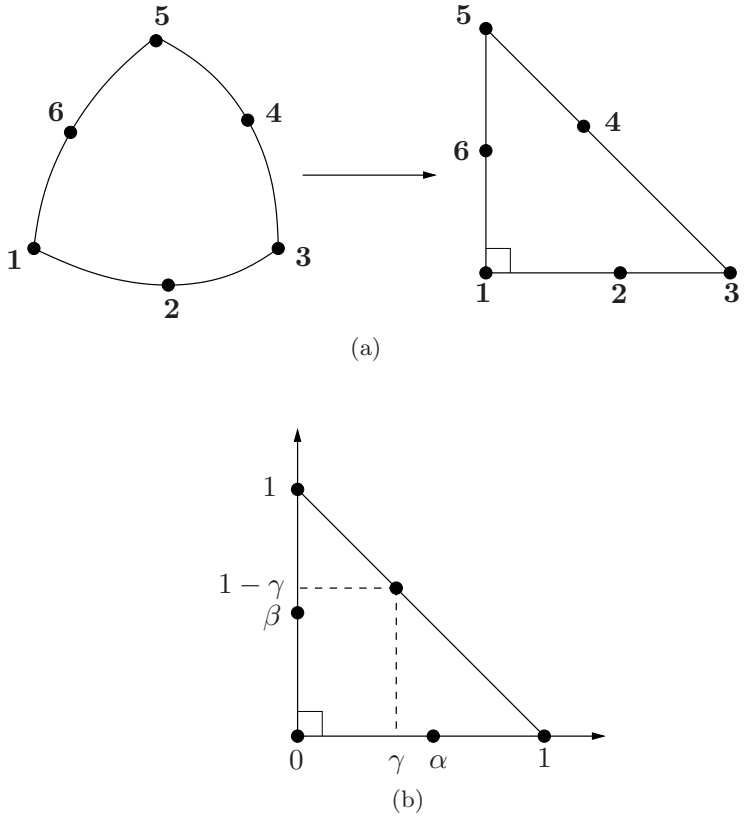

Figure 3.2: a) Mapping of a quadratic triangle in three-dimensional space to a two-dimensional right isosceles triangle. b) Coordinates of points in the $\xi\eta$ plane.

membrane is discretised by subdividing each face of an icosahedron into 4^n elements, and projecting them radially onto a sphere to generate a mesh of $N_E = 20(4^n)$ elements. This results in $N_p = 2N_E + 2$ points on the surface. The amount of mesh refinement is controlled by the mesh coefficient n (Table 3.1). The unstructured nature of the mesh leads to a C^0 continuous surface. Each surface element is mapped to a flat isosceles triangle defined with two parametric coordinates ξ and η, as shown in Figure 3.2. The six element points $\boldsymbol{x}_1$, $\boldsymbol{x}_2$, $\boldsymbol{x}_3$, $\boldsymbol{x}_4$, $\boldsymbol{x}_5$ and $\boldsymbol{x}_6$ are mapped to the points (0, 0), (1, 0), (0, 1), (α, 0), (γ, $1-\gamma$) and (0, β) respectively in the $\xi\eta$ plane. The parametric coordinates

ξ and η vary between 0 and 1. The coefficients α, β and γ are calculated using

$$\alpha = \left(1 + \frac{|\boldsymbol{x}_4 - \boldsymbol{x}_2|}{|\boldsymbol{x}_4 - \boldsymbol{x}_1|}\right)^{-1}, \beta = \left(1 + \frac{|\boldsymbol{x}_6 - \boldsymbol{x}_3|}{|\boldsymbol{x}_6 - \boldsymbol{x}_1|}\right)^{-1}, \gamma = \left(1 + \frac{|\boldsymbol{x}_5 - \boldsymbol{x}_2|}{|\boldsymbol{x}_5 - \boldsymbol{x}_3|}\right)^{-1} \tag{3.17}$$

Any function $h(\boldsymbol{x})$ can be approximated quadratically over an element with

$$h(\xi, \eta) = \sum_{i=1}^{6} h_i \phi_i(\xi, \eta), \tag{3.18}$$

where h_i is the value of h at node i and the nodal shape functions ϕ_i are defined as

$$\begin{aligned}
\phi_2(\xi,\eta) &= \frac{1}{1-\alpha}\xi\left(\xi - \alpha + \frac{\alpha-\gamma}{1-\gamma}\eta\right) \\
\phi_3(\xi,\eta) &= \frac{1}{1-\beta}\eta\left(\eta - \beta + \frac{\beta-\gamma-1}{\gamma}\xi\right) \\
\phi_4(\xi,\eta) &= \frac{1}{\alpha(1-\alpha)}\xi\left(1-\xi-\eta\right) \\
\phi_5(\xi,\eta) &= \frac{1}{\gamma(1-\gamma)}\xi\eta \\
\phi_6(\xi,\eta) &= \frac{1}{\beta(1-\beta)}\eta(1-\xi-\eta) \\
\phi_1(\xi,\eta) &= 1 - \phi_2 - \phi_3 - \phi_4 - \phi_5 - \phi_6
\end{aligned} \tag{3.19}$$

Equation 3.18 can be used to approximate the position, tangent and normal vectors on each element according to

$$\boldsymbol{x}(\xi,\eta) = \sum_{i=1}^{6} x_i \phi_i(\xi,\eta) \tag{3.20}$$

$$\frac{\partial \boldsymbol{x}}{\partial \xi}(\xi,\eta) = \sum_{i=1}^{6} x_i \frac{\partial \phi_i}{\partial \xi}(\xi,\eta) \tag{3.21}$$

$$\frac{\partial \boldsymbol{x}}{\partial \eta}(\xi,\eta) = \sum_{i=1}^{6} x_i \frac{\partial \phi_i}{\partial \eta}(\xi,\eta) \tag{3.22}$$

$$\boldsymbol{n}(\xi,\eta) = \frac{1}{h_s}\left(\frac{\partial \boldsymbol{x}}{\partial \xi} \times \frac{\partial \boldsymbol{x}}{\partial \eta}\right), \tag{3.23}$$

where h_s is the surface metric, defined as

$$h_s = \left|\frac{\partial \boldsymbol{x}}{\partial \xi} \times \frac{\partial \boldsymbol{x}}{\partial \eta}\right| \tag{3.24}$$

Although the unstructured discretisation presented is less accurate than the structured methods developed by Lac *et al.* (2004) and Kessler *et al.* (2008), a lower-order method has been chosen in an effort to capture large singular deformations suspected to occur when the deformable body is very close to the wall.

3.4 Discretisation of Boundary Integral Equation

Discretising equation 3.15 yields:

$$u_j(\mathbf{x}_0) = \frac{2}{1+\lambda}u_j^{\infty}(\mathbf{x}_0) - \frac{1}{4\pi(1+\lambda)Ca}\sum_{m=1}^{N_E}\int_{E_m}\Delta f_i(\mathbf{x})G_{ij}(\mathbf{x},\mathbf{x}_0)dS(\mathbf{x}) + \frac{1-\lambda}{4\pi(1+\lambda)}\sum_{m=1}^{N_E}\int_{E_m}^{PV}u_i(\mathbf{x})T_{ijk}(\mathbf{x},\mathbf{x}_0)n_k(\mathbf{x})dS(\mathbf{x}) \tag{3.25}$$

Equation 3.25 can be solved to yield the velocity of each marker point, once the traction discontinuity $\Delta\boldsymbol{f}$ and the integrals over each element have been computed. The definition and calculation of the traction discontinuity follow in section 3.5. The singularities that occur when $\boldsymbol{x}$ and $\boldsymbol{x}_0$ are equal need to be dealt with in both the single and double-layer integrals. The methods for dealing with both regular and singular integrals are outlined in section 3.6.

3.5 Elastic Stresses

3.5.1 Definition

To formulate the relationship between the membrane tension tensor $\boldsymbol{T}$ and the deformation of the membrane described in equation 3.7, Barthés-Biesel & Rallison (1981) introduced the surface deformation gradient tensor $\boldsymbol{A}$, defined as

$$\boldsymbol{A} = (\boldsymbol{I} - \boldsymbol{nn}) \cdot \frac{\partial \boldsymbol{x}}{\partial \boldsymbol{X}} \cdot (\boldsymbol{I} - \boldsymbol{NN}), \tag{3.26}$$

where $\boldsymbol{X}$ is the position of a point on the membrane in the reference state, $\boldsymbol{x}$ is the corresponding position in the deformed state, and $\boldsymbol{N}$ is the unit normal vector to the membrane in the reference state (Figure 3.3). Any deformation of a body can be decomposed into a rigid body rotation and a stretching of the body

$$\boldsymbol{A} = \boldsymbol{R} \cdot \boldsymbol{\Lambda}, \tag{3.27}$$

where $\boldsymbol{R}$ is a rotation tensor and $\boldsymbol{\Lambda}$ is a stretch tensor.

The left Cauchy-Green strain tensor $\boldsymbol{B}$ follows as (Pozrikidis 2001*b*)

$$\boldsymbol{B} = \boldsymbol{\Lambda} = \boldsymbol{A} \cdot \boldsymbol{A}^T. \tag{3.28}$$

The eigenvalues of $\boldsymbol{B}$ are λ_1^2,λ_2^2 and 0, where λ_i are the stretch ratios in the principal directions of the deformation. Invariants of the Cauchy-Green tensor can be used to

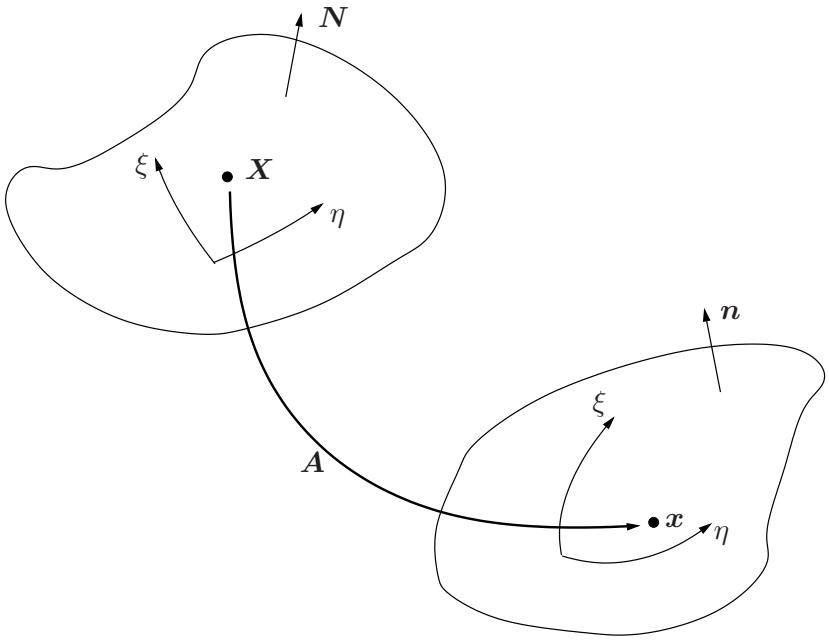

Figure 3.3: The surface deformation gradient tensor $\boldsymbol{A}$ maps the reference state of the membrane to its deformed state.

completely characterise the membrane deformation. These are defined as

$$I_1 = \lambda_1^2 + \lambda_2^2 - 2 \text{ and } I_2 = \lambda_1^2\lambda_2^2 - 1 \tag{3.29}$$

If the membrane elasticity is assumed to be both local and instantaneous, then the mechanical response of the membrane can be characterised by a strain energy function $w = f(\lambda_1, \lambda_2, \lambda_3)$. A further assumption is made that the stretching along $\boldsymbol{n}$, λ_3, is determined locally by the other stretch ratios and thus w is a function of λ_1 and λ_2 only.

This allows the membrane tension tensor $\boldsymbol{T}$ to be related to the membrane deformation by

$$\boldsymbol{T} = \frac{2}{\lambda_1\lambda_2}\left[\frac{\partial w}{\partial I_1}\boldsymbol{B} + \lambda_1^2\lambda_2^2\frac{\partial w}{\partial I_2}(\boldsymbol{I} - \boldsymbol{nn})\right]. \tag{3.30}$$

Equation 3.30 describes arbitrary membrane deformations for a given strain energy function.

The strain energy function w can be chosen to represent different classes of hyperelastic materials, including an elastic neo-Hookean membrane

$$w = \frac{G}{2}\left(\lambda_1^2 + \lambda_2^2 + \frac{1}{\lambda_1^2\lambda_2^2}\right), \tag{3.31}$$

or a biological-like membrane, known as the Skalak law (Skalak *et al.* 1973)

$$w = \frac{G}{4}\left((\lambda_1^2 - 1)^2 + (\lambda_2^2 - 1)^2 + C(\lambda_1^2\lambda_2^2 - 1)^2\right), \tag{3.32}$$

where G is the surface shear elastic modulus, and CG is the area dilation elastic modulus. The constant C gives a measure of the amount of area dilation allowed by the cell. When $C \gg 1$ the Skalak law models an area incompressible membrane.

3.5.2 Calculation

To calculate the membrane tension tensor $\boldsymbol{T}$ at each point on the cell surface, the surface deformation gradient tensor $\boldsymbol{A}$ is required. The surface deformation gradient tensor $\boldsymbol{A}$ operates on the two surface tangent vectors in the reference state to give the two tangent vectors in the deformed state

$$\boldsymbol{A}.\frac{\partial \boldsymbol{X}}{\partial \xi} = \quad \frac{\partial \boldsymbol{x}}{\partial \xi}, \tag{3.33}$$

$$\boldsymbol{A}.\frac{\partial \boldsymbol{X}}{\partial \eta} = \quad \frac{\partial \boldsymbol{x}}{\partial \eta}. \tag{3.34}$$

$\boldsymbol{A}$ also acts on the reference normal vector in the following manner

$$\boldsymbol{A} \cdot \boldsymbol{N} = \boldsymbol{0}. \tag{3.35}$$

Eq. (3.33), (3.34) and (3.35) allow the surface deformation gradient tensor $\boldsymbol{A}$ at each point on the membrane to be calculated. However, because the mesh is C^0 continuous, $\boldsymbol{A}$ is multi-valued at each marker point. To circumvent this difficulty, the multiple values of $\boldsymbol{A}$ are averaged at each node, weighted by the area of the elements sharing the point. The normal vectors at each point are approximated in the same fashion. Once the surface deformation gradient tensor and the normal vectors are known at each point, the membrane tension tensor follows from Eq. (3.28) and (3.30)

With the membrane tension tensor now known at each node it is possible to determine the corresponding values of the traction discontinuity Δf_i from equation 3.7. However, calculating the surface divergence of the tension tensor on an unstructured grid introduces and amplifies errors, causing the simulation to become unstable (Ramanujan & Pozrikidis 1998). To eliminate the numerical error associated with numerical differentiation on an unstructured grid, the single-layer integral can be approximated with (Ramanujan & Pozrikidis 1998)

$$\int_{E_m} \Delta f_i G_{ij}(\boldsymbol{x}, \boldsymbol{x}_0)\ \mathrm{d}S(\boldsymbol{x}) \approx \langle \Delta f_i \rangle_m \int_{E_m} G_{ij}(\boldsymbol{x}, \boldsymbol{x}_0)\ \mathrm{d}S(\boldsymbol{x}), \tag{3.36}$$

where $\langle \Delta f_i \rangle_m$ is the average surface traction discontinuity over the nth element. Equation 3.36 is in effect a three-dimensional implementation of the trapezoidal rule. The

average traction on an element with area A_m enclosed by contour C_m can be calculated by applying the divergence theorem to equation 3.7 to yield (Ramanujan & Pozrikidis 1998)

$$\langle \Delta f_i \rangle_m = -\frac{1}{A_m} \oint_{C_m} \tau_i b_i \, \mathrm{d}l, \tag{3.37}$$

where $\boldsymbol{b} = \boldsymbol{t} \times \boldsymbol{n}$ is the unit vector pointing outward from the surface, perpendicular to the unit normal vector $\boldsymbol{t}$ to A_m and the unit tangent vector $\boldsymbol{b}$ to C_m. The stress field along the contour of each element is determined by linear interpolation from the nodal values.

With this approximation equation 3.25 becomes

$$\begin{aligned} u_j(\mathbf{x}_0) = \frac{2}{1+\lambda} u_j^{\infty}(\mathbf{x}_0) - \frac{1}{4\pi\mu_1(1+\lambda)} \sum_{n=1}^{N_E} \langle \Delta f_i \rangle_m \int_{E_m} G_{ij}(\boldsymbol{x}, \boldsymbol{x}_0) \, \mathrm{d}S(\boldsymbol{x}) \\ + \frac{1-\lambda}{4\pi(1+\lambda)} \sum_{m=1}^{N_E} \int_{E_m}^{PV} u_i(\mathbf{x}) T_{ijk}(\mathbf{x}, \mathbf{x}_0) n_k(\mathbf{x}) dS(\mathbf{x}) \end{aligned} \tag{3.38}$$

3.6 Integration

3.6.1 Non-Singular Integrals

When the source point $\boldsymbol{x_0}$ does not lie on the element E_m, the integrals are non-singular and can be calculated using an N_Q-point triangular domain Gaussian integration formula (Pozrikidis 2002)

$$\int_{E_m} f(\boldsymbol{x}) \, \mathrm{d}S(\boldsymbol{x}) = \frac{1}{2} \sum_{m=1}^{N_Q} f[\boldsymbol{x}(\xi_m, \eta_m)] h_s(\xi_m, \eta_m) w_m, \tag{3.39}$$

where $f(\boldsymbol{x})$ is the function being integrated, N_Q is the number of quadrature base points, (ξ_k, η_k) are the coordinates of the kth base point in parametric space and w_k is the integration weight corresponding to the kth base point.

3.6.2 Singular Integrals

Single-Layer Integral

The integral over an element can be written as

$$\int_{E_m} G_{ij}(\boldsymbol{x}, \boldsymbol{x}_0) \, \mathrm{d}S(\boldsymbol{x}) = \int_0^1 \int_0^{1-\xi} G_{ij}[\boldsymbol{x}(\xi, \eta), \boldsymbol{x}_0] h_s(\xi, \eta) \, \mathrm{d}\eta \, \mathrm{d}\xi \tag{3.40}$$

When the source point $\boldsymbol{x_0}$ lies on the element E_m, the integrand G_{ij} exhibits a singularity of $O(1/r)$. The singularity prevents the accurate use of Gaussian quadrature,

but can be dealt with by using a polar coordinate system with the origin located at the singular point (Figure 3.4). The transformation is given by

$$\eta - \eta_0 = r' \cos\theta,\ \xi - \xi_0 = r' \sin\theta, \tag{3.41}$$

where (ξ_0,η_0) is the position of the singular point. If the singular point is located at $\boldsymbol{x}_1$ then equation 3.40 can be written as

$$\begin{aligned} &\int_0^1 \int_0^{1-\xi} G_{ij}[\boldsymbol{x}(\xi,\eta),\boldsymbol{x}_0] h_s(\xi,\eta)\,\mathrm{d}\eta\,\mathrm{d}\xi \\ &= \int_0^{\pi/2} \int_0^{\frac{1}{\cos\theta+\sin\theta}} G_{ij}[\boldsymbol{x}(\xi(r',\theta),\eta(r',\theta)),\boldsymbol{x}_0] h_s(\xi(r',\theta),\eta(r',\theta)) r'\,\mathrm{d}r'\,\mathrm{d}\theta, \end{aligned} \tag{3.42}$$

where r' is the Jacobian of the transformation. The presence of r' in the integral means that the integral is now non-singular and can be integrated using Gauss-Legendre quadrature in both polar coordinates. If the singular point is located at $\boldsymbol{x}_2$ or $\boldsymbol{x}_3$, then equation 3.42 can be used if the nodes are temporarily relabelled to ensure that the singular point is located at $(0,0)$ in the $\xi\eta$ plane. If the singular point is located at $\boldsymbol{x}_5$, equation 3.40 can be written as

$$\begin{aligned} &\int_0^1 \int_0^{1-\xi} G_{ij}[\boldsymbol{x}(\xi,\eta),\boldsymbol{x}_0] h_s(\xi,\eta)\,\mathrm{d}\eta\,\mathrm{d}\xi = \\ &\int_{3\pi/4}^{\pi+\tan^{-1}(\frac{1-\gamma}{\gamma})} \int_0^{\frac{-\gamma}{\cos\theta_1}} G_{ij}[\boldsymbol{x}(\xi(r_1',\theta_1),\eta(r_1',\theta_1)),\boldsymbol{x}_0] h_s(\xi(r_1',\theta_1),\eta(r_1',\theta_1)) r_1'\,\mathrm{d}r_1'\,\mathrm{d}\theta_1 \\ &+ \int_{\pi+\tan^{-1}(\frac{1-\gamma}{\gamma})}^{7\pi/4} \int_0^{\frac{\gamma-1}{\sin\theta_2}} G_{ij}[\boldsymbol{x}(\xi(r_2',\theta_2),\eta(r_2',\theta_2)),\boldsymbol{x}_0] h_s(\xi(r_2',\theta_2),\eta(r_2',\theta_2)) r_2'\,\mathrm{d}r_2'\,\mathrm{d}\theta_2, \end{aligned} \tag{3.43}$$

and evaluated with Gauss-Legendre quadrature. If the singular point is located at one of the other two edge nodes, $\boldsymbol{x}_4$ or $\boldsymbol{x}_6$, the points can be temporarily relabelled to enable equation 3.43 to be used.

Double-Layer Integral

The $O(1/r)$ singularity of the double-layer integral can be removed by rewriting it in the form (Pozrikidis 2002)

$$\begin{aligned} &\int_{E_m}^{PV} u_i(\mathbf{x}) T_{ijk}(\mathbf{x},\mathbf{x}_0) n_k(\mathbf{x}) dS(\mathbf{x}) = \\ &\qquad \int_{E_m} [u_i(\boldsymbol{x}) - u_i(\boldsymbol{x}_0)] T_{ijk}(\mathbf{x},\mathbf{x}_0) n_k(\mathbf{x}) dS(\mathbf{x}) + 4\pi u_j(\boldsymbol{x}_0). \end{aligned} \tag{3.44}$$

The integral on the RHS of equation 3.44 can then be computed using Gaussian quadrature.

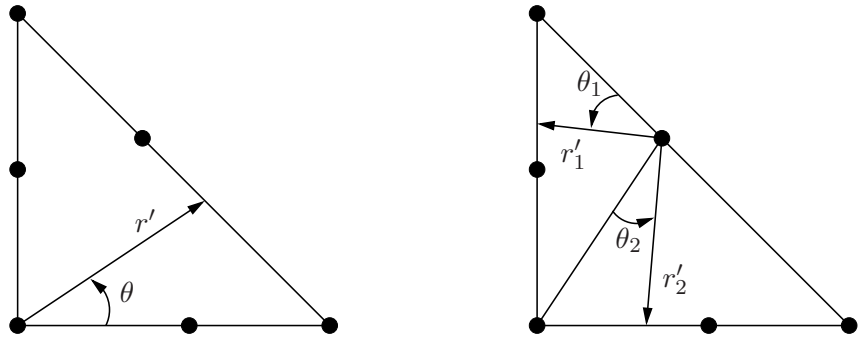

(a) (b)

Figure 3.4: Transformation to polar coordinates for accurate integration of singular integrals

3.7 Cell Prestressing

At shear rates below $Ca \sim 0.3$, a cell with a purely elastic membrane undergoes a buckling instability (Lac *et al.* 2004). The buckling instability is caused by the presence of compressive tensions in the membrane, and is only present due to the neglect of bending resistance. The implementation of bending resistance into an unstructured boundary-element implementation is extremely difficult, and places severe constraints on the size of the time step. A more amenable method of stabilising the membrane at low shear rates is to prestress the membrane (Lac & Barthés-Biesel 2005). The amount of membrane prestress α is defined as

$$\alpha = \frac{a}{a_0} - 1, \tag{3.45}$$

where a is the radius of the shape of the cell at $t = 0$, and a_0 is the radius of the reference shape of the cell.

3.8 Matrix Inversion

If the viscosity ratio is not equal to one, the velocities of the marker points cannot be found explicitly. As a consequence a linear set of $3N_P$ equations need to be solved. The LAPACK routine *dgesv* can be used to solve the linear set of equations using LU decomposition to yield the velocities of the marker points.

3.9 Parallelisation

The computation of equation 3.25 is very amenable to parallelisation, especially with a viscosity ratio of one. MPI functions can be used to implement code parallelisation.

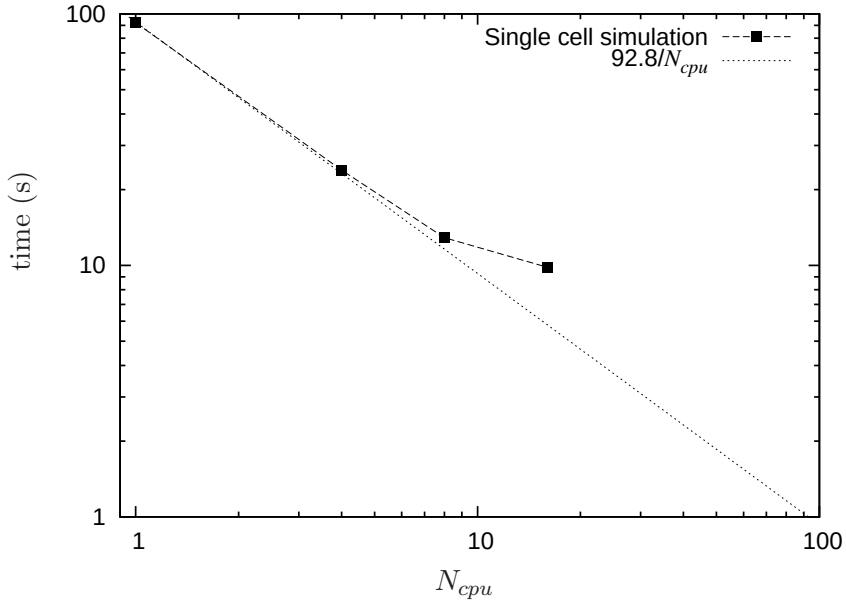

Figure 3.5: System time per simulation time step as a function of number of processors used N_{cpu} for a cell with 1280 elements. Also shown is the line of best fit for a function that scales inversely with the number of processors used.

At each time step, the master processor calculates the tension tensor at each node, and following this the average traction discontinuity on each element. The node list is then divided evenly amongst the n processors, and each processor then calculates the velocity of each of the assigned nodes. The velocities are then collected by the master processor, and the solution is integrated forward in time.

The system time for one simulation time step is shown in Figure 3.5. Ideally, the system time should scale inversely with the number of processors used. It is apparent however that the improvement in system time decreases significantly as the number of processors used changes from eight to sixteen. As a result, all three-dimensional results presented in this thesis are from simulations run on eight processors.

3.10 Time-stepping

Once the velocities of the particle have been found via the solution of the boundary-integral equations, a time-stepping routine needs to be employed to determine the new position and shape of the cell membrane. The differential equation to be solved to determine the new position of the membrane is given by

$$\frac{d\boldsymbol{x}_i}{dt} = \boldsymbol{u}_i \tag{3.46}$$

To solve equation 3.46, the Runge-Kutta-Fehlberg (RKF45) method is used (Math-

ews & Fink 1999). In the RKF45 method, Equation 3.46 is solved using a 4th order Runge-Kutta method. Based on the local truncation error, the time step for the next integration is adjusted to ensure optimal time step size. An approximation of the local truncation error is obtained by comparing the solution given by the 4th order Runge-Kutta method to that given by a 5th order Runge-Kutta method. Each time step requires six velocity evaluations, given by

$$\begin{aligned}
k_1 =& u\left(t^{(n)}, x^{(n)}\right)\Delta t,\\
k_2 =& u\left(t^{(n)} + \frac{1}{4}\Delta t, x^{(n)} + \frac{1}{4}k_1\right)\Delta t,\\
k_3 =& u\left(t^{(n)} + \frac{3}{8}\Delta t, x^{(n)} + \frac{3}{32}k_1 + \frac{9}{32}k_2\right)\Delta t,\\
k_4 =& u\left(t^{(n)} + \frac{12}{13}\Delta t, x^{(n)} + \frac{1932}{2197}k_1 - \frac{7200}{2197}k_2 + \frac{7296}{2197}k_3\right)\Delta t,\\
k_5 =& u\left(t^{(n)} + \Delta t, x^{(n)} + \frac{439}{216}k_1 - 8k_2 + \frac{3680}{513}k_3 - \frac{845}{4104}k_4\right)\Delta t,\\
k_6 =& u\left(t^{(n)} + \frac{1}{2}\Delta t, x^{(n)} - \frac{8}{27}k_1 + 2k_2 - \frac{3544}{2565}k_3 + \frac{1859}{4104}k_4 - \frac{11}{40}k_5\right)\Delta t.
\end{aligned} \tag{3.47}$$

The solution to equation 3.46 can then be obtained using a 4th order Runge-Kutta method

$$x^{(n+1)} = x^{(n)} + \frac{25}{216}k_1 + \frac{1408}{2565}k_3 + \frac{2197}{4101}k_4 - \frac{1}{5}k_5. \tag{3.48}$$

Another solution can be obtained using a 5th order Runge-Kutta method

$$\hat{x}^{(n+1)} = x^{(n)} + \frac{16}{135}k_1 + \frac{6656}{12825}k_3 + \frac{28561}{56430}k_4 - \frac{9}{50}k_5 + \frac{2}{55}k_6, \tag{3.49}$$

in order to obtain an estimate of the local truncation error.

The time step size Δt can then be controlled using the quantity

$$s = \left(\frac{\frac{1}{2}\epsilon}{\left|\hat{x}^{(n+1)} - x^{(n+1)}\right|}\right)^{\frac{1}{4}} \tag{3.50}$$

where ϵ is the specified error control tolerance on the time step size, and the denominator is the local truncation error estimate. If s is greater than 1.5, then the time step is doubled. If s is less than 0.75, the time step is halved. The error control tolerance used in all simulations is $\epsilon = 10^{-10}$.

3.11 Cell Metric Definitions

3.11.1 Taylor Deformation Parameter

A common measure of deformation used in the literature is the Taylor deformation parameter D_{ij}, which is defined as

$$D_{ij} = \frac{|l_i - l_j|}{l_i + l_j}, \tag{3.51}$$

where l_i denotes the semi-axis length in the ith direction of an ellipsoid with the same inertia tensor as the cell. The inertia tensor of the cell can be calculated from

$$\begin{aligned} \boldsymbol{I} &= \int_V \rho \begin{bmatrix} y^2+z^2 & -xy & -xz \\ -xy & x^2+z^2 & -yz \\ -xz & -yz & x^2+z^2 \end{bmatrix} dV \\ &= \rho \int_S \begin{bmatrix} \frac{1}{3}(y^3 n_y + z^3 n_z) & -\frac{1}{4}xy(xn_x + yn_y) & -\frac{1}{4}xz(xn_x + zn_z) \\ -\frac{1}{4}xy(xn_x + yn_y) & \frac{1}{3}(x^3 n_x + z^3 n_z) & -\frac{1}{4}yz(yn_y + zn_z) \\ -\frac{1}{4}xz(xn_x + zn_z) & -\frac{1}{4}yz(yn_y + zn_z) & \frac{1}{3}(x^3 n_x + y^3 n_y) \end{bmatrix} dS, \end{aligned} \tag{3.52}$$

where n_i is the ith component of the unit normal vector on the surface of the cell, and ρ is the density. The volume integral in equation 3.52 has been converted to a surface integral using the divergence theorem. The inertia tensor of an ellipsoid is given by

$$\begin{bmatrix} \frac{1}{5}\rho V(l_2^2 + l_3^2) & 0 & 0 \\ 0 & \frac{1}{5}\rho V(l_1^2 + l_3^2) & 0 \\ 0 & 0 & \frac{1}{5}\rho V(l_1^2 + l_2^2) \end{bmatrix}. \tag{3.53}$$

The semi-axis lengths l_1, l_2, and l_3 can be calculated by finding the eigenvalues of the cell inertia tensor and equating them to the eigenvalues of the ellipsoid inertia tensor. The Taylor deformation parameter can then be calculated using equation 3.51.

3.11.2 Cell Velocity

The centre of the cell $\boldsymbol{x}^c$ can be tracked at each time step using the integral equation

$$x_i^c = \frac{3}{4\pi}\int_V x_i \, dV = \frac{3}{8\pi}\int_S x_i^2 n_i \, dS, \tag{3.54}$$

where the volume integral has been converted to a surface integral using the divergence theorem. The velocity of the cell $\dot{\boldsymbol{x}}^c$ can then be calculated by fitting a cubic spline to $\boldsymbol{x^c} = f(t)$ and taking the derivative with respect to time.

The slip velocity of the cell u_{slip} is defined as the difference between the velocity of the undisturbed fluid and the velocity of the cell at the cell centroid

$$u_{slip} = ky^c - \dot{x}^c. \tag{3.55}$$

Projected Area

To calculate the projected area of the cell, the integral equation

$$A_i = \int_S \boldsymbol{x} \cdot \hat{\boldsymbol{e}}_{\boldsymbol{i}}\, dS \tag{3.56}$$

can be used, where A_i is the projected area of the surface on the plane defined by the unit normal vector $\hat{\boldsymbol{e}}_i$.

3.11.3 Shear Stress

The traction discontinuity $\Delta \boldsymbol{f}$ is defined as the stress vector parallel to the unit normal vector of the cell surface equation 3.7. Thus, the magnitude of this vector gives the magnitude of the principal shear stress on the surface of the cell

$$\sigma_{SS} = |\Delta \boldsymbol{f}|\,. \tag{3.57}$$

When the cell is prestressed, the shear stress of the cell is finite in its initial configuration. When this is the case, the increase in shear stress is used, defined as

$$\Delta\sigma_{SS}(t) = \sigma_{SS}(t) - \sigma_{SS}(t=0). \tag{3.58}$$

To calculate the shear stress on the surface of the wall, the velocity of the flow at the vertices of a quadrilateral mesh located in the region above the wall can be calculated using (Pozrikidis 1992)

$$\begin{aligned} u_j(\mathbf{x}_0) = u_j^{\infty}(\mathbf{x}_0) - \frac{1}{8\pi Ca}\int_S \Delta f_i(\mathbf{x}) G_{ij}(\mathbf{x}, \mathbf{x_0}) dS(\mathbf{x}) \\ + \frac{1-\lambda}{8\pi}\int_S^{PV} u_i(\mathbf{x}) T_{ijk}(\mathbf{x}, \mathbf{x_0}) n_k(\mathbf{x}) dS(\mathbf{x}). \end{aligned} \tag{3.59}$$

The velocity gradient tensor $\frac{\partial u_j}{\partial x_i}$ is then calculated using second-order central differences in the interior of the mesh, and first-order one-sided differences on the boundaries. On the wall, the velocity gradient tensor takes the form

$$\begin{bmatrix} 0 & 0 & 0 \\ \frac{\partial u}{\partial y} & 0 & \frac{\partial w}{\partial y} \\ 0 & 0 & 0 \end{bmatrix}, \tag{3.60}$$

due to no-slip and continuity constraints.

With the velocity gradient tensor defined at the wall, the wall stress tensor can be calculated with

$$\sigma_{ij} = \frac{\partial u_i}{\partial x_j} + \frac{\partial u_j}{\partial x_i}, \tag{3.61}$$

yielding

$$\begin{bmatrix} 0 & \frac{\partial u}{\partial y} & 0 \\ \frac{\partial u}{\partial y} & 0 & \frac{\partial w}{\partial y} \\ 0 & \frac{\partial w}{\partial y} & 0 \end{bmatrix}. \tag{3.62}$$

Hence, the principal wall shear stress can be calculated with

$$\sigma_{SS} = \sqrt{\left(\frac{\partial u}{\partial y}\right)^2 + \left(\frac{\partial w}{\partial y}\right)^2}. \tag{3.63}$$

3.12 Convergence and Validation

3.12.1 Mesh Resolution

Two-Dimensional Model

To ensure that the results gained were mesh-independent, a grid resolution study was undertaken. The force on the tether of a cell with aspect ratio $a/b = 1$ at a shear rate of $Ca = 0.25$ and a viscosity ratio of $\lambda = 1$ is shown in Figure 3.6 over a range of mesh sizes. As the mesh resolution increases, the force on the tether decreases monotonically. The order of accuracy of the method for this case can be estimated as $O(N_E^{-1.45})$. The difference over the range of mesh sizes considered is 3.4%. Increasing the mesh size from 256 elements to 320 elements changes the value by less than 0.5%, suggesting that convergence has been reached. Figure 3.6 also shows the force on the tether of a cell with aspect ratio $a/b = 0.25$ at a shear rate of $Ca = 0.25$ and a viscosity ratio of $\lambda = 10$. The order of accuracy of the method for this case can be estimated as $O(N_E^{-2.45})$, and the solution difference over the range of mesh sizes is 0.5%. Hence, in all two-dimensional simulations, the mesh resolution is set at 256 elements.

The variation of the force on the tether as the number of integration quadrature points is increased is shown in Table 3.2. Differences of less than 0.1% can be observed, and the number of Gauss-Legendre points is set at $N_{GL} = 6$ for all two-dimensional simulations.

Three-Dimensional Model

Figure 3.7 shows the change with mesh size of the maximum deformation parameter D_{12}^{MAX} for a cell at initial wall height $h/a = 1.2$ with shear rate $Ca = 0.90$ and area dilation parameter $C = 2.5$. The difference over the range of mesh resolutions is $\sim 1.6\%$, suggesting convergence has been reached. The order of accuracy of the method can be

b)

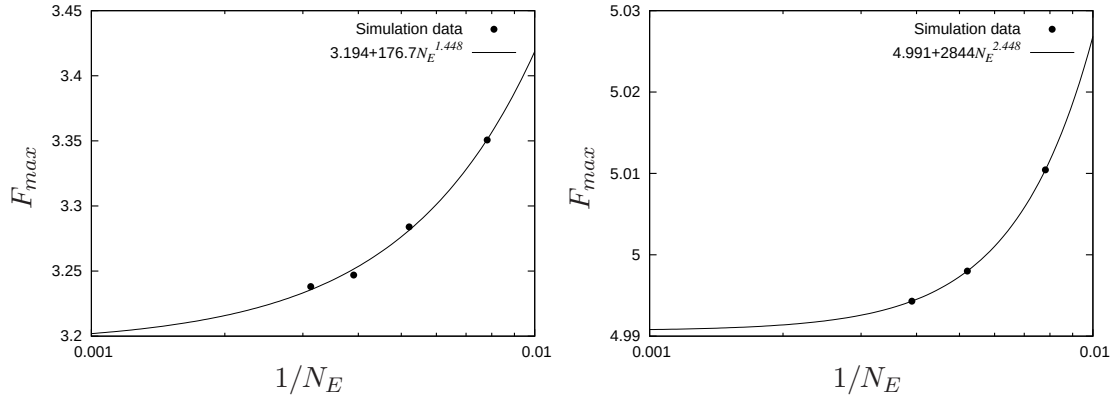

Figure 3.6: Effect of mesh size N_E on the maximum force acting on the tether for a two-dimensional cell with a) aspect ratio $a/b = 1$, shear rate $Ca = 0.25$ and viscosity ratio $\lambda = 1$, and b) a) aspect ratio $a/b = 0.25$, shear rate $Ca = 0.25$ and viscosity ratio $\lambda = 10$. Also shown are the lines of best fit of the form $F_{max} = \hat{F}_{max} + C(N_E)^{\alpha}$, where $\hat{F}_{max}$ is the mesh-independent solution, C is a constant, and α is an estimate of the method's order of accuracy.

N_{GL}	F_{MAX}
5	3.2525
6	3.2469
8	3.2474
12	3.2475

Table 3.2: Effect of number of Gaussian-Legendre quadrature points N_{GL} on the maximum force acting on the tether for a two-dimensional cell with aspect ratio $a/b = 1$, shear rate $Ca = 0.25$ and viscosity ratio $\lambda = 1$

estimated as $O(N_E^{-0.75})$. For all three-dimensional simulations, a mesh size of 1280 elements is used.

The variation of the equilibrium deformation parameter D_{12}^{∞} for a cell in unbounded shear flow at a shear rate $Ca = 1.80$ and membrane prestress $\alpha = 0.025$ with increasing integration quadrature points is shown in Table 3.3. A difference of less than 0.2% can be seen over the range of quadrature points chosen. The number of quadrature points is set at $N_Q = 7$ for all three-dimensional simulations.

N_Q	D_{12}^{∞}
6	0.5378
7	0.5380
9	0.5385
13	0.5387

Table 3.3: Effect of number of Gaussian quadrature points N_Q on the equilibrium Taylor deformation parameter D_{12}^{∞} for a three-dimensional cell in unbounded shear flow with shear rate $Ca = 1.80$ and membrane prestress $\alpha = 0.025$.

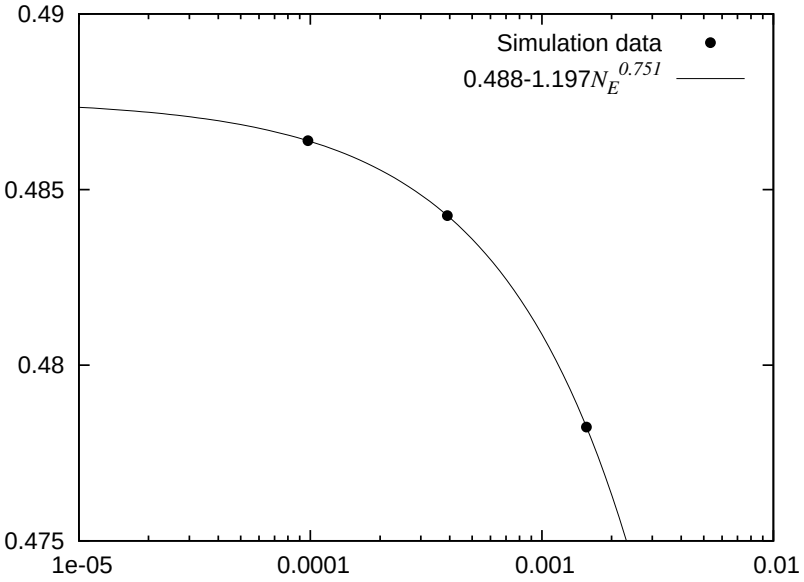

Figure 3.7: Effect of mesh size N_E on the maximum Taylor deformation parameter D_{12}^{MAX} for a three-dimensional cell at initial wall height $h/a = 1.2$ with shear rate $Ca = 0.90$ and area dilation parameter $C = 2.5$. Also shown is the line of best fit of the form $D_{12}^{max} = \hat{D}_{12}^{max} + C(N_E)^{\alpha}$, where $\hat{D}_{12}^{max}$ is the mesh-independent solution, C is a constant, and α is an estimate of the method's order of accuracy.

3.12.2 Validation

Two-Dimensional Model

Figure 3.8 shows a comparison of data from the two-dimensional model with the numerical data of Breyiannis & Pozrikidis (2000). Excellent agreement can be seen over the range of shear rates tested. The difference between the two data sets is below 0.5% for all cases. Accuracy of the method could also be checked by tracking the area of the cell over the length of the simulations. Changes of less than 0.5% were evident in most cases. At a viscosity ratio of $\lambda = 10$, the change in area was less than 1.5%. At higher viscosity ratios the change in area increased significantly, restricting the range of viscosity ratios studied.

Three-Dimensional Model

To validate the three-dimensional simulation, a comparison was made with the numerical data of Lac *et al.* (2004), who used a boundary-element method with a structured mesh discretisation to investigate the effect of shear rate on a capsule in unbounded shear flow (Figure 3.9). The maximum difference between the two data sets was 1.2%, at a shear rate of $Ca = 0.75$. The difference between the two data sets can be explained

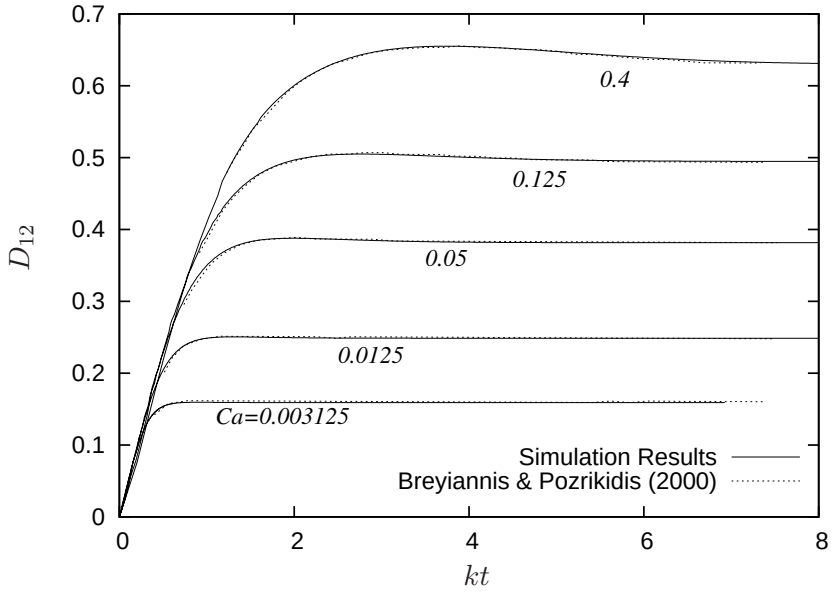

Figure 3.8: Comparison of simulation data at different shear rates with the numerical data of Breyiannis & Pozrikidis (2000)

with an observation by Lac *et al.* (2004), who noted that the values obtained with their procedure yields deformation parameters $\sim 1.3\%$ higher than the unstructured mesh discretisation scheme used by Ramanujan & Pozrikidis (1998).

To ensure the accuracy of the simulation when modelling Skalak capsules under prestress, a comparison was made with the results of Lac & Barthés-Biesel (2005), for a Skalak capsule prestressed at 2.5% in unbounded shear flow at a shear rate of $Ca = 1.80$. The measurements of Lac & Barthés-Biesel (2005) gives an equilibrium deformation parameter $D_{12}^{\infty} = 0.547$. The results of the simulation gives a value of $D_{12}^{\infty} = 0.538$, a difference of 1.6%. A difference of this magnitude can also be explained by the different discretisation schemes used. For all simulations considered, the volume of the capsule changed by less than 0.3%.

It can therefore be concluded that the numerical scheme appears to be implemented correctly, and gives physically meaningful results.

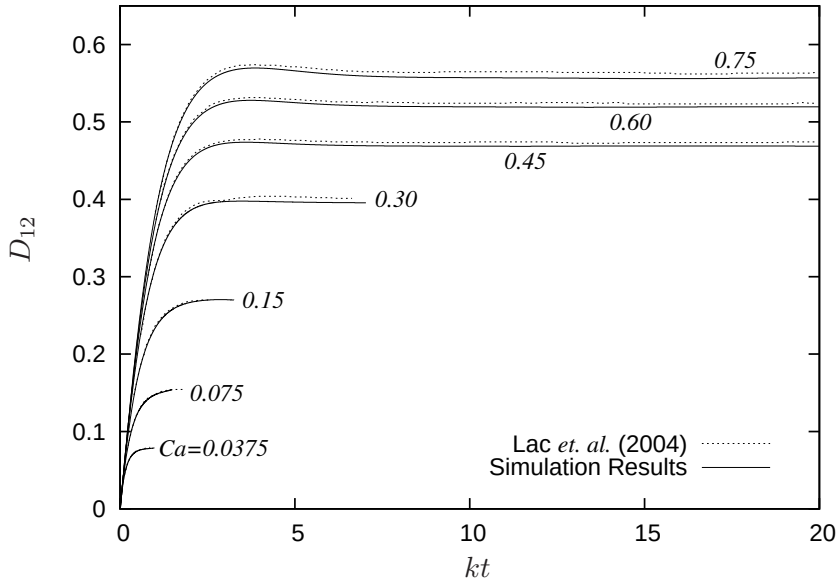

Figure 3.9: Comparison of simulation data at different shear rates with the numerical data of Lac *et al.* (2004)

	2D cell	Single 3D cell	Two 3D cells
No. of points	256	2562	5124
No. of CPUs	1	8	16
Required Memory	34MB	130MB	550MB
No. of time steps	$10,000$	$1,500 - 10,000$	$3,000$
Time per time step	6.9s	12.9s	26.3s

Table 3.4: Computational data for a two-dimensional simulation with one cell, a three-dimensional simulation with one cell, and a three-dimensional simulation with two cells. The simulations were run on 3.0Ghz Intel processors.

CHAPTER 4

TETHERED CELL DYNAMICS

The presence of long, thin membrane tethers extruded from the surface of both leukocytes and platelets undergoing adhesion has been observed in experiments. At a low shear rate of 200s^{-1} the leukocyte membrane tether consists of a single bond, and very little overall cell deformation is observed. However, at a higher shear rate of $800s^{-1}$, membrane tethers consisting of multiple bonds have been observed to form, with length $7-12\mu$m (0.6−1 cell diameters), and width $\sim 2\mu$m (0.17 cell diameters) (Ramachandran *et al.* 2004). Schmidtke & Diamond (2000) observed tethers of mean length 6μm (0.5 cell diameters) over a shear rate range $100 - 250\text{s}^{-1}$ with a growth rate of $6 - 40\mu$m/s. Significant overall cell deformation can be observed when the leukocyte tether consists of multiple bonds. Dopheide *et al.* (2002) observed tether formation in platelets, and observed that the mean tether length ranged from $3 - 16\mu$m ($1 - 5$ cell diameters) over a shear rate range of 150s^{-1} to $10,000\text{s}^{-1}$.

Two regimes were noted during tether formation by Evans *et al.* (2005) and Heinrich *et al.* (2005), who formed leukocyte tethers using a bio-membrane force probe. At first, the tether was extruded with a linear elastic extension of the cell membrane. After this elastic behaviour, a viscous membrane-pulling regime was observed, attributed to the dissociation of the bond from the cytoskeleton. The resistive force of the tether was found to depend on the pulling speed in this regime. The authors postulated that the force on the tether exponentially relaxes to a speed-dependent plateau force.

A model of a cell tether was developed by King *et al.* (2005), who used a boundary element method to model a rigid spherical body connected to a wall with an elastic tether. The initial extraction of the tether was modelled using a linearly elastic spring, and the viscoelastic effect of cytoskeletal dissociation was captured using a phenomenological model in which the force on the tether was proportional to the pulling speed.

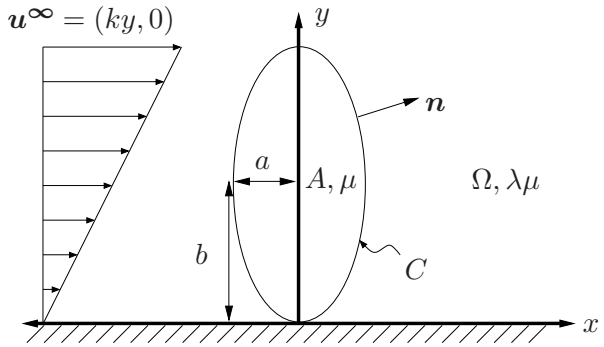

Figure 4.1: Schematic diagram of two-dimensional cell model above a plane wall in linear shear flow. The area A of the cell is kept constant for all cell shapes, and the length scale of the problem is $L = \sqrt{ab}$.

The transition from spring to viscoelastic model was controlled with a stochastic dissociation model. The model was able to capture tether lengths of $\sim 1.5\mu m$, at a dimensionless shear rate of $Ca \sim 10^{-3}$, but neglected overall cell deformation and the effect of cytoplasmic viscosity. A similar model was developed by Yu & Shao (2007) to examine the effect of simultaneous tether extraction from both the cell surface and the vessel wall, demonstrating that deformation of the vessel wall contributes to the length of the tether.

The present study aims to provide some understanding of the effects of membrane elasticity, internal cell viscosity and cell aspect ratio on the deformation and forces experienced by a cell tethered to a surface. Hence, the hypothesis to be tested in this chapter is that *the dynamics of a tethered cell are affected by the aspect ratio and the internal viscosity of the cell.* The stochastic nature of cell adhesion and tether formation is not investigated in this study. The effect of cell deformation on the force, length, deformation and growth rate of a tethered cell will be examined by assuming that a stable tether has been formed at time $t^* = t_0$.

To investigate the effect of cell shape, the deformation of a cell is considered for an initial circular cell, $a/b = 1$, and two initially elliptic cells, $a/b = 0.25$, and $a/b = 0.5$. The aspect ratio a/b is defined in Figure 4.1. To determine the effect of internal cell viscosity, a viscosity ratio range of $1 \leq \lambda \leq 10$ has been chosen. The viscosity ratio of a leukocyte is of the order of 10^5, which is too high to model accurately. However, a trend as λ increases may be able to be discerned, allowing conclusions to be drawn on cells at higher viscosity ratios. The shear rate range chosen is $0.01 \leq Ca \leq 0.25$. Bending resistance is neglected, and the internal area of each cell is kept constant over

the range of aspect ratios, giving a length scale of $L = \sqrt{ab}$. The model used to test the hypothesis in this chapter only captures some of the physics involved with physiological tethered cells, but

4.1 Solution Procedure

To simulate a tether, the node closest to the wall is fixed in position. It was found that imposing shear flow at $t^* = 0$ onto the reference cell with one node fixed was too unstable to generate equilibrium solutions for some of the parameter space examined. In the initial stages of deformation a sawtooth-like instability was observed in the velocities of the marker points immediately upstream of the tether point. The size of the instability increased when a finer mesh was used. The constraint of zero velocity applied to the tether point means that marker points immediately upstream move towards the tether, placing this region of the membrane under compression. The presence of the instability may be explained by the tendency of elastic membranes to exhibit buckling under compression, which causes the oscillations of quantities such as curvature and velocity (Lac *et al.* 2007).

To overcome this problem, the cell was freely suspended at $y = 0.005$ above the wall and allowed to deform to its maximum extent, without fixing the lowest node of the cell. The lowest point of the resulting cell contour was then fixed in position at $(x/L, y/L) = (0, 0.005)$, to represent a tether. Some initial shapes for cells with aspect ratios $a/b = 0.25$, and $a/b = 1$ over a range of shear rates are shown in Figure 4.2.

It is reasonable to assume that the relaxation time for an elastic capsule will scale as some function of the viscosity ratio λ. For a liquid drop at a shear rate $Ca \ll 1$, the characteristic time-scale for relaxation scales with the viscosity ratio function (Leal 2007)

$$f(\lambda) = \frac{(2\lambda + 3)(19\lambda + 16)}{40(\lambda + 1)}. \tag{4.1}$$

For viscosity ratios $\lambda \gg 1$, this function reduces to $f(\lambda) = \lambda$. As a consequence the dimensionless time has been rescaled by λ throughout this study.

4.2 Cell Deformation

The evolution of the cell contour shown in Figure 4.3 is for a cell of aspect ratio $a/b = 1$ and viscosity ratio $\lambda = 1$, for shear rates $Ca = 0.01$ and 0.25. It can be seen that the

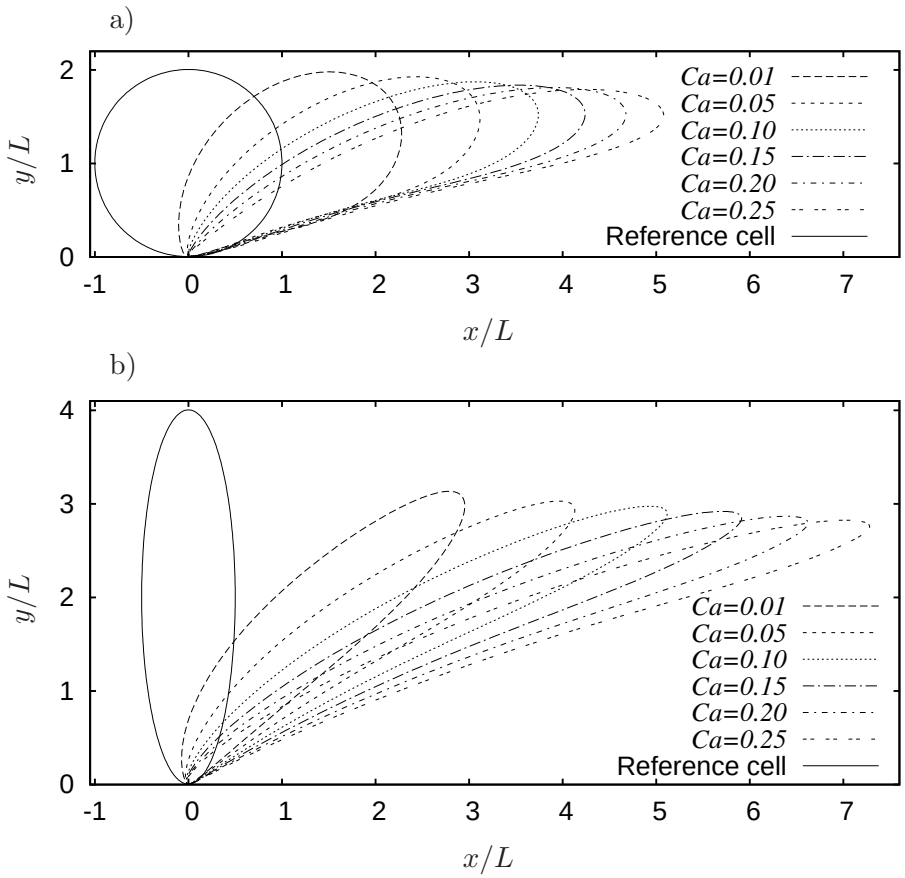

Figure 4.2: Initial cell contours over a range of shear rates for a cell with viscosity ratio $\lambda = 1$ and aspect ratio a) $a/b = 1$, and b) $a/b = 0.25$. Flow is from left to right.

cell pivots around the tether point and moves closer to the wall as time evolves. This suggests that, if the tether does not break, contact with the wall will occur. It is also apparent that at a high shear rate of $Ca = 0.25$ the cell is initially highly deformed, but relaxes as the cell moves closer to the wall.

Figure 4.4 shows a progression of steady-state contours for cells of aspect ratios $a/b = 0.25$ and $a/b = 1$, and a viscosity ratio $\lambda = 1$, for $0.01 \leq Ca \leq 0.25$. It can be seen that the cell is drawn out into a flatter, thinner shape along the wall as the shear rate increases. The elliptic cell is drawn out further along the wall due to its larger initial contour length. It is also apparent that the elliptic cells sit up higher above the wall than the circular cells.

A comparison of cell contours at different viscosity ratios, with aspect ratios $a/b = 0.25$ and $a/b = 1$ at the lowest shear rate of $Ca = 0.01$, and time $k(t - t_0)/\lambda = 10$, is shown in Figure 4.5. It is clear that the choice of scaling function $f(\lambda) = \lambda$ is appropriate at low shear rates, as the circular cell contours over the range of viscosity ratios studied are almost identical. For the elliptic cell some variation can be observed, with the tether becoming thinner as the viscosity ratio increases. Again, it is very clear

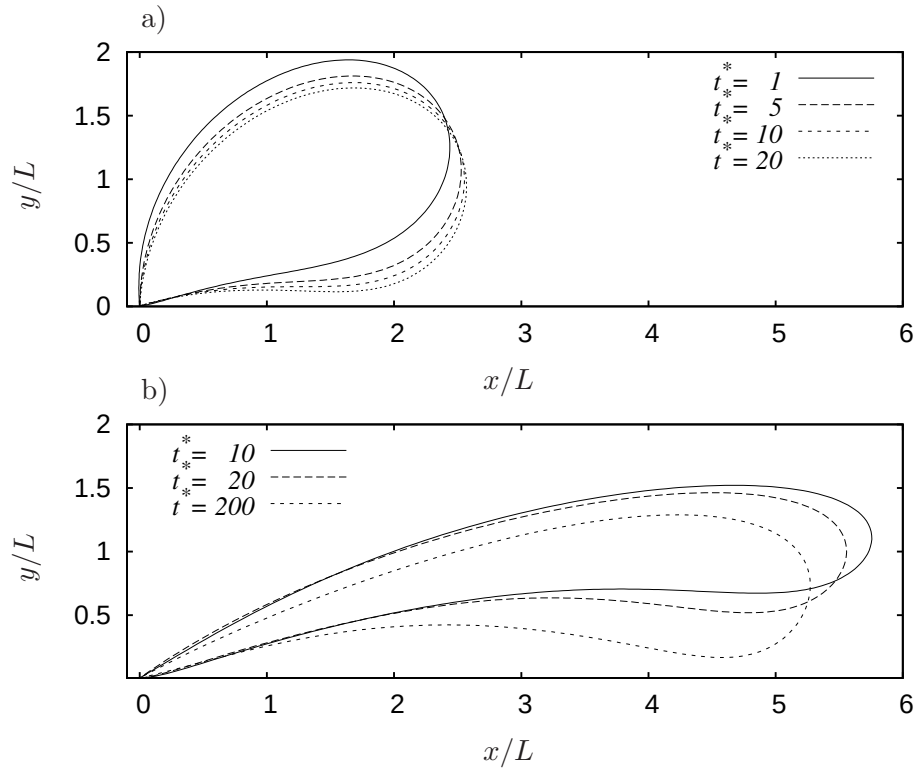

Figure 4.3: Cell contours at different times for a cell with aspect ratio $a/b = 1$ and viscosity ratio $\lambda = 1$ at a shear rate of a) $Ca = 0.01$, and b) $Ca = 0.25$. Flow is from left to right.

that the elliptic cells sit much higher above the wall than the circular cells.

Figure 4.6 depicts the contours of cells with aspect ratios $a/b = 0.25$ and $a/b = 1$ at the highest shear rate of $Ca = 0.25$, and time $k(t - t_0)/\lambda = 200$. Significant variation in cell contour with viscosity ratio can be observed, with a thinner tether forming as the viscosity ratio increases. The cell length in the flow direction also increases with viscosity ratio. As the viscosity ratio increases the cell contours appear to be converging to a λ-independent shape, indicating that the choice of $f(\lambda)$ is also appropriate at high shear rates and high viscosity ratios. The elliptic cells form much thinner tethers, and again can be observed to sit higher above the wall than the circular cells.

The evolution of the normalised cell contour length A/A_0 over a range of shear rates is shown in Figure 4.7 for a cell with aspect ratio $a/b = 1$ at viscosity ratios of $\lambda = 1$ and 10. The normalised cell contour length, defined as the ratio of the contour length A to the reference cell contour length A_0, provides a measure of the overall deformation of the cell. At the lowest shear rate of $Ca = 0.01$, the evolution of the cell deformation reaches a steady-state much quicker than the cells at the highest shear rate of $Ca = 0.25$. This is because, at low shear rates Ca, the cell relaxation time-scale

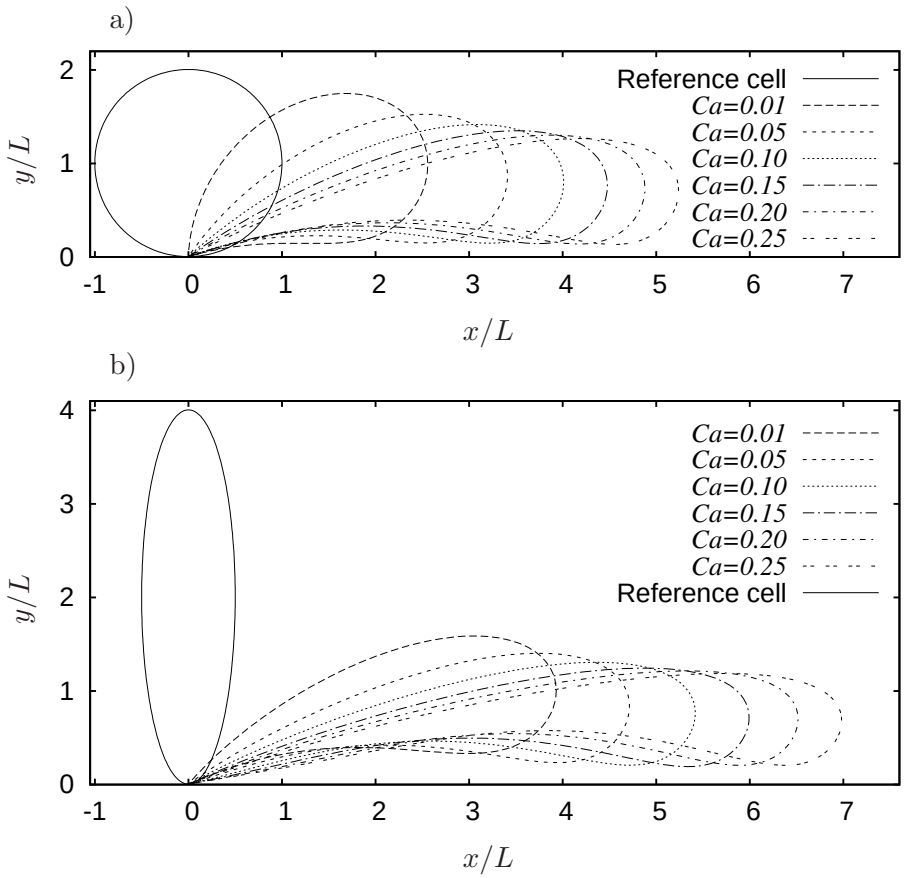

Figure 4.4: Equilibrium cell contours over a range of shear rates for a cell with viscosity ratio $\lambda = 1$ and aspect ratio a) $a/b = 1$, and b) $a/b = 0.25$. The cell is determined to be in an equilibrium state when the L_2-norm of the difference in position between successive time steps falls below 10^{-7}.

is much smaller than the flow time-scale, and the cell shape adjusts to the flow very quickly. It is clear that for the highest shear rate of $Ca = 0.25$, the viscous response of the cell is slower to respond to the initial elastic deformation caused by the tethering of the cell. Immediately after tether formation the cell contour length increases rapidly to a maximum value, an effect that becomes more pronounced as the shear rate increases. Once the maximum value has been reached, the cell contour length decreases slowly thereafter. The behaviour of the evolution of the deformation of the cell is qualitatively similar to that of the model developed by King *et al.* (2005).

The effect of varying the viscosity ratio can be observed in Figure 4.8, which shows the evolution of the normalised contour length for a cell of aspect ratio $a/b = 1$, and varying viscosity ratio. At the lowest shear rate of $Ca = 0.01$, varying the viscosity ratio has very little effect on the magnitude of the cell deformation. However, because the relaxation time-scale for a capsule appears to scale inversely with λ, the cell deforms at a slower rate as the viscosity ratio increases. At the highest shear rate of $Ca = 0.25$,

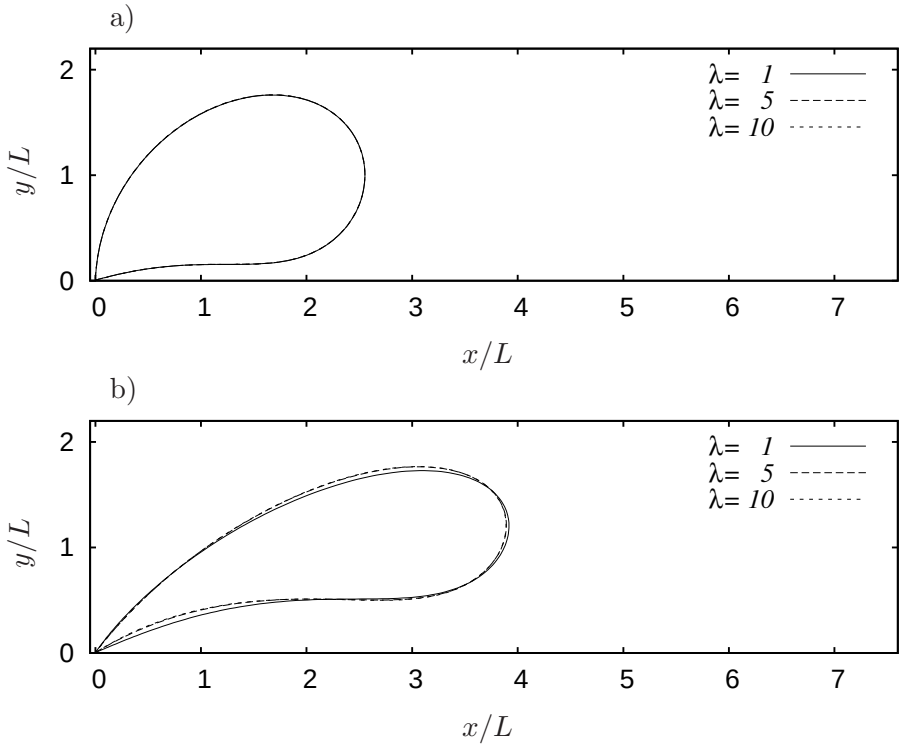

Figure 4.5: Cell contours at shear rate $Ca = 0.01$, and time $k(t - t_0)/\lambda = 10$ for a) aspect ratio $a/b = 1$, and b) aspect ratio $a/b = 0.25$. Flow is from left to right.

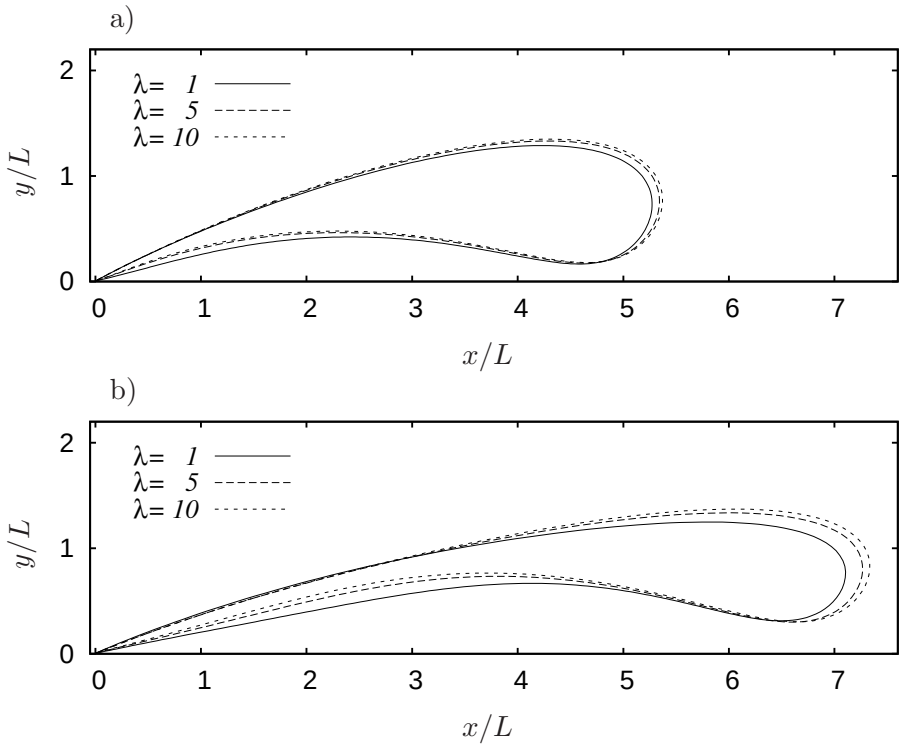

Figure 4.6: Cell contours at shear rate $Ca = 0.25$, and time $k(t - t_0)/\lambda = 200$ for a) aspect ratio $a/b = 1$, and b) aspect ratio $a/b = 0.25$. Flow is from left to right.

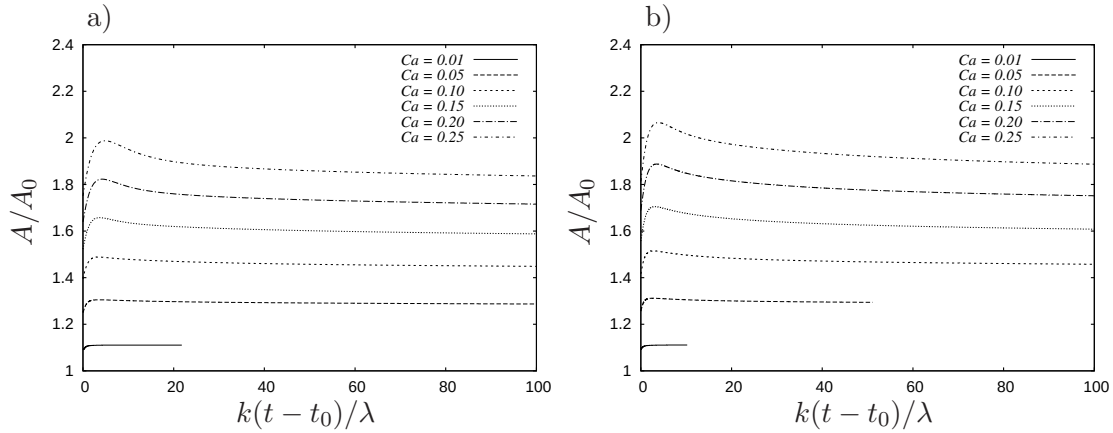

Figure 4.7: Evolution of normalised cell contour length A/A_0 over a range of shear rates for a cell with aspect ratio $a/b = 1$ and viscosity ratio a) $\lambda = 1$, and b) $\lambda = 10$. A is the cell contour length at time $k(t - t_0)/\lambda$, and A_0 is the contour length of the reference cell.

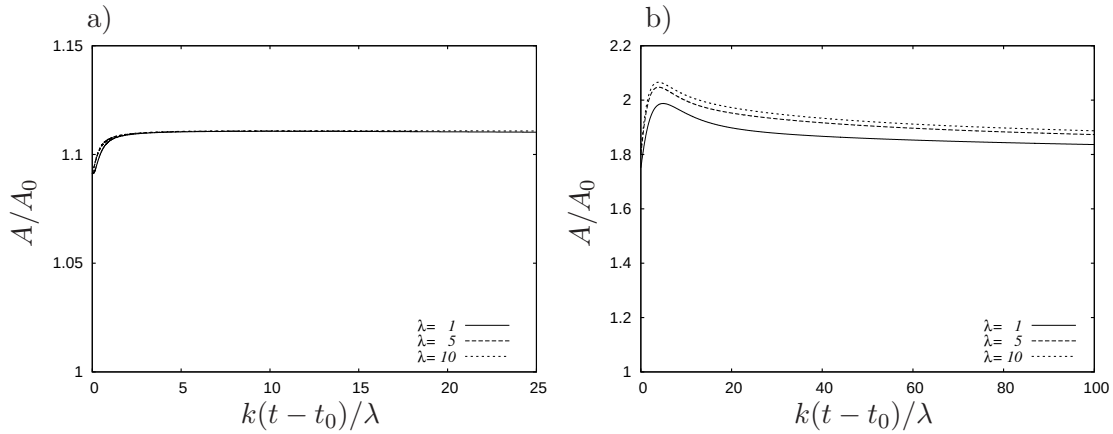

Figure 4.8: Evolution of normalised cell contour length A/A_0 over a range of viscosity ratios for a cell of aspect ratio $a/b = 1$ at a shear rate of a) $Ca = 0.01$, and b) $Ca = 0.25$. A is the cell contour length at time $k(t - t_0)/\lambda$, and A_0 is the contour length of the reference cell.

the cell deformation increases with increasing viscosity ratio.

Figure 4.9 shows the effect of aspect ratio on the normalised cell contour length. At the lowest shear rate of $Ca = 0.01$, the deformation of the cell increases with increasing aspect ratio. As the aspect ratio decreases, the time to maximum cell deformation shortens. At the highest shear rate $Ca = 0.25$, the maximum deformation of the cell increases with decreasing aspect ratio. At longer times however, the deformation of the cells with lower aspect ratios is less than the deformation of cells with higher aspect ratios.

Figure 4.10 shows the maximum normalised cell contour length as a function of shear rate for cells with aspect ratios $a/b = 0.25$, and $a/b = 1$. The overall cell deformation

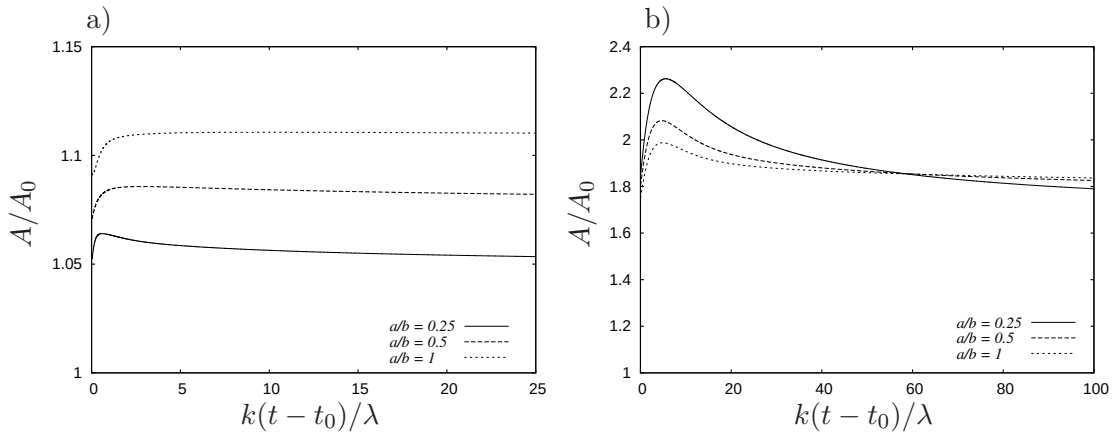

Figure 4.9: Evolution of normalised cell contour length A/A_0 over a range of aspect ratios for a cell of viscosity ratio $\lambda = 1$ at a shear rate of a) $Ca = 0.01$, and b) $Ca = 0.25$. A is the cell contour length at time $k(t - t_0)/\lambda$, and A_0 is the contour length of the reference cell.

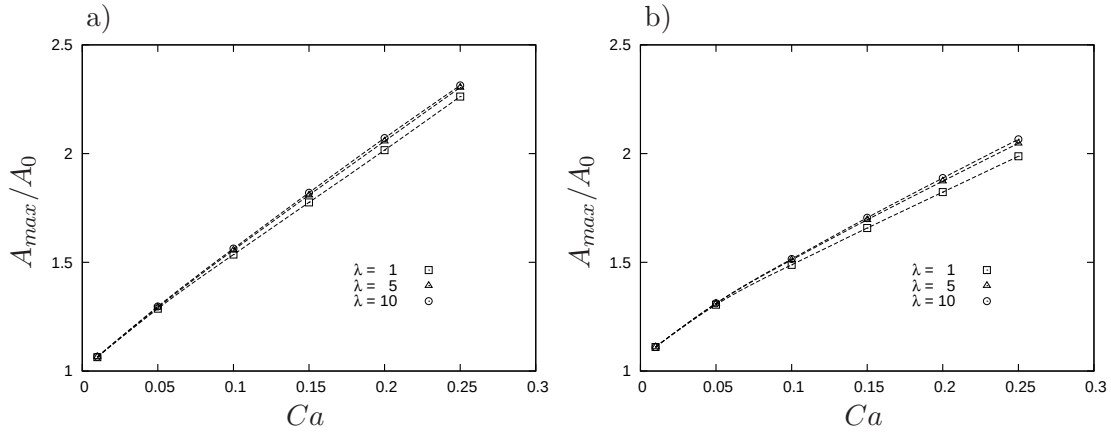

Figure 4.10: Maximum normalised cell contour length A_{max}/A_0 as a function of shear rate for a cell with aspect ratio a) $a/b = 0.25$, and b) $a/b = 1$. A is the cell contour length at time $k(t - t_0)/\lambda$, and A_0 is the contour length of the reference cell.

increases with the shear rate, but the rate of increase lessens as the shear rate increases. The rate of increase of the elliptic cell deformation is greater than that of the circular cell. It is clear that the effect of varying the viscosity ratio only becomes pronounced at shear rates $Ca \gtrsim 0.1$.

4.3 Tether Length

Also of interest is the effect of varying the shear rate, cell shape and viscosity ratio on the length of the cell tether. The length of the cell in the flow direction has been chosen to represent the tether length, as it can be easily measured as

$$L_{cell} = x_{max} - x_{min} \tag{4.2}$$

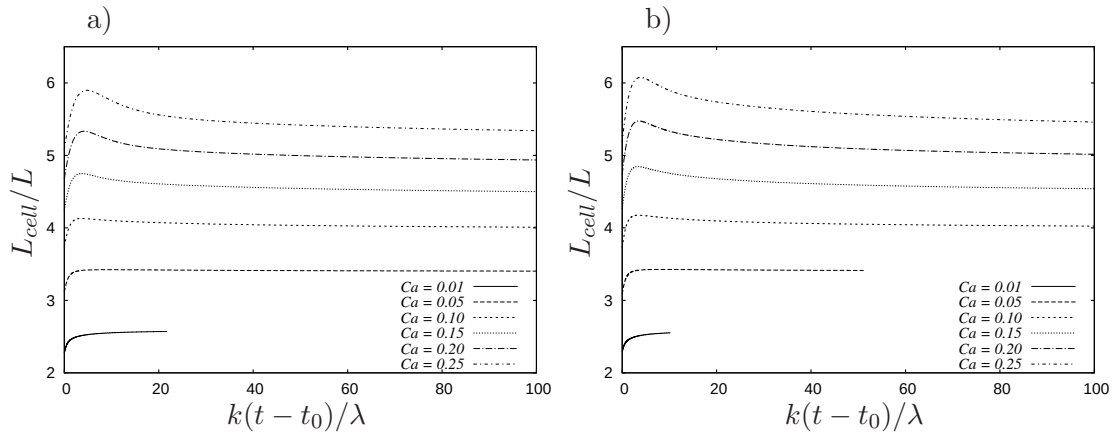

Figure 4.11: Evolution of cell length L_{cell}/L over a range of shear rates for a cell of aspect ratio $a/b = 1$ and viscosity ratio a) $\lambda = 1$, and b) $\lambda = 10$.

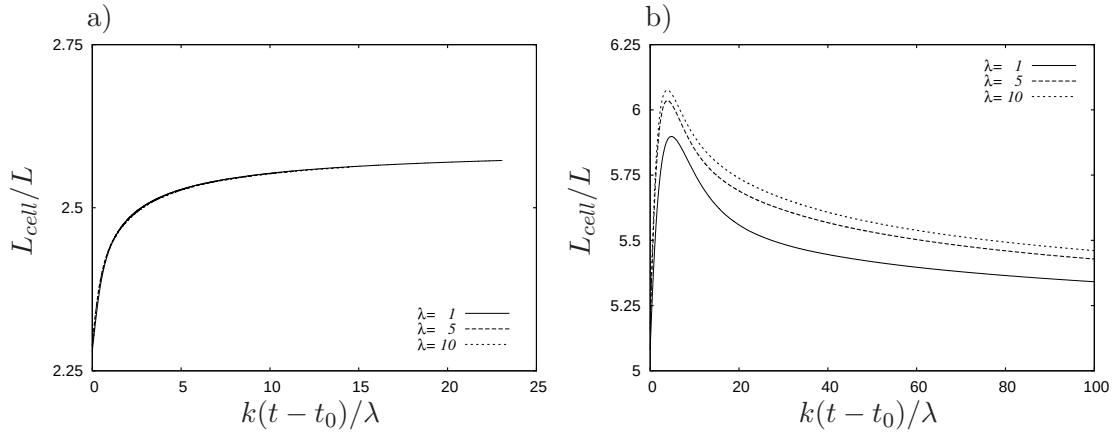

Figure 4.12: Evolution of cell length L_{cell}/L over a range of viscosity ratios for a cell of aspect ratio $a/b = 1$ at a shear rate of a) $Ca = 0.01$, and b) $Ca = 0.25$.

The evolution of the length of the cell in the flow direction shown in Figure 4.11 is for a cell of aspect ratio $a/b = 1$, and viscosity ratios $\lambda = 1$ and 10. The evolution of the cell length is qualitatively similar to the overall cell deformation for all aspect ratios. The length increases to a maximum value, and then decreases slowly as the tether time increases, an effect that becomes more pronounced with increasing shear rate.

The effect of viscosity ratio on the cell length can be seen in Figure 4.12. As observed with the overall cell deformation, the cell length is not affected by the viscosity ratio at a shear rate of $Ca = 0.01$. At the highest shear rate of $Ca = 0.25$, the cell length increases with increasing viscosity ratio.

Figure 4.13 shows the effect of cell aspect ratio on the cell length. At shear rates of $Ca = 0.01$, and $Ca = 0.25$, the cell length increases with increasing aspect ratio. The maximum cell length as a function of shear rate for cells with aspect ratios $a/b = 0.25$, and $a/b = 1$ is shown in Figure 4.14. It is again evident that the viscosity ratio only

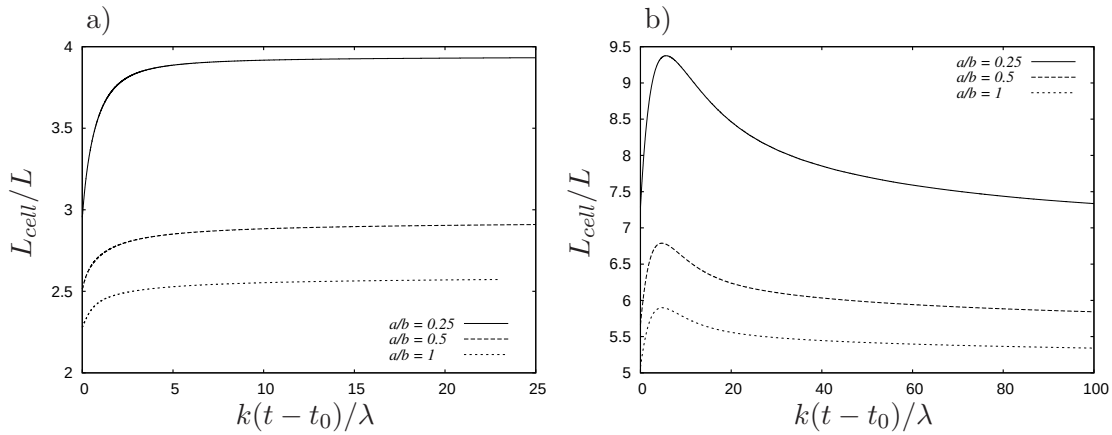

Figure 4.13: Evolution of cell length L_{cell}/L over a range of aspect ratios for a cell of viscosity ratio $\lambda = 1$ at a shear rate of a) $Ca = 0.01$, and b) $Ca = 0.25$.

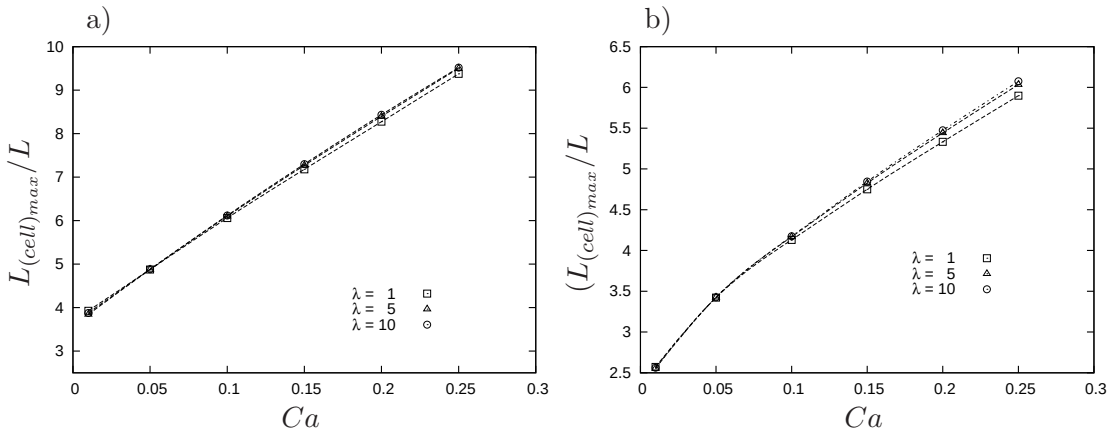

Figure 4.14: Maximum cell length $L_{(cell)_{max}}/L$ as a function of shear rate for a cell with aspect ratio a) $a/b = 0.25$, and b) $a/b = 1$

has an effect at shear rates $Ca \gtrsim 0.1$.

4.4 Force on Tether

Figure 4.15 shows the evolution of the force acting on the tether. The force on the tether increases rapidly to a maximum value for all shear rates, and then decreases as time advances. The evolution of the force is qualitatively similar to the results of the model developed by King *et al.* (2005). The presence of a maximum force soon after tether formation suggests that if the tether were to break then it would happen shortly after formation, and the longer a tether is present the more likely it is that stable adhesion will occur.

Figure 4.16 illustrates the effect of viscosity ratio on the force evolution of a cell with aspect ratio $a/b = 1$. At the lowest shear rate of $Ca = 0.01$, the viscosity ratio has no effect on the force evolution. At the higher shear rate of $Ca = 0.25$, the force on

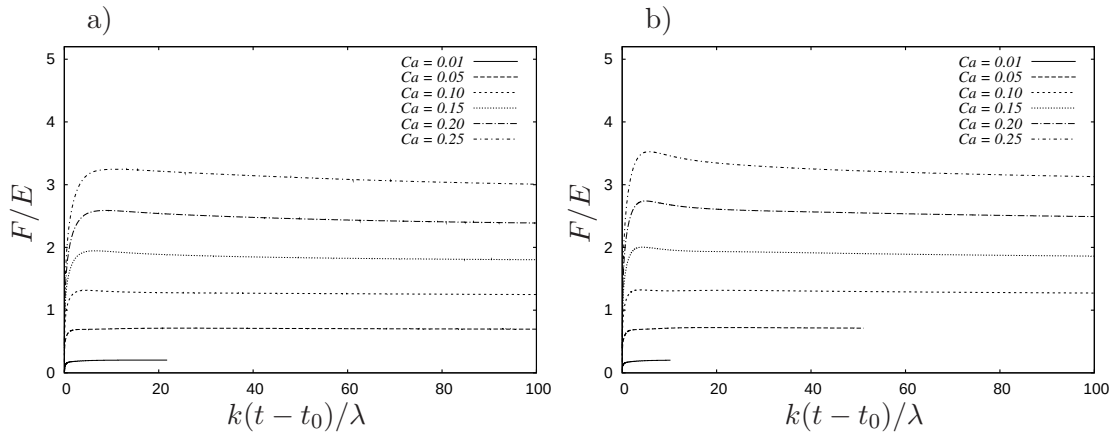

Figure 4.15: Evolution of force on tether F/E over a range of shear rates for a cell with aspect ratio $a/b = 1$ and viscosity ratio a) $\lambda = 1$, and b) $\lambda = 10$.

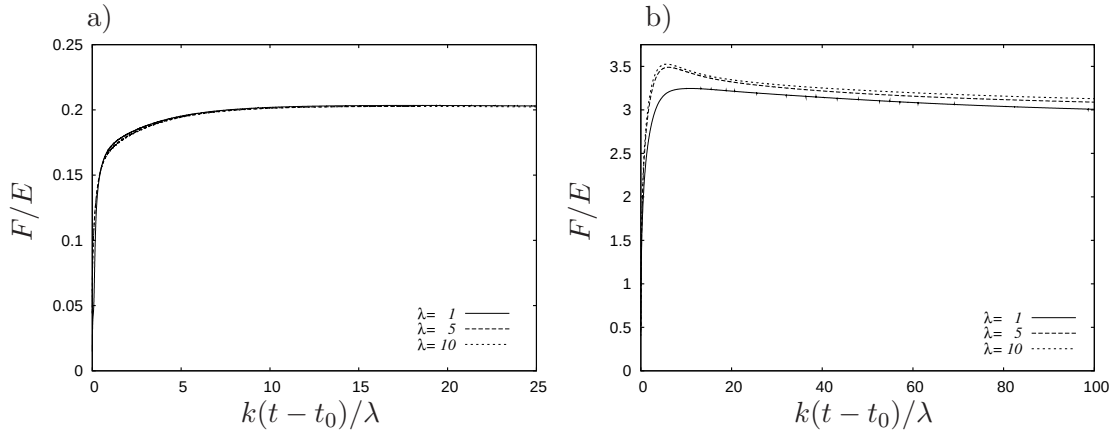

Figure 4.16: Evolution of force on tether F/E over a range of viscosity ratios for a cell of aspect ratio $a/b = 1$ at a shear rate of a) $Ca = 0.01$, and b) $Ca = 0.25$.

the tether increases with increasing viscosity ratio. The maximum force on the tether also becomes more pronounced with increasing viscosity ratio. The initial evolution of the force on the tether at low shear rates agrees qualitatively with the observations of Evans *et al.* (2005) and Heinrich *et al.* (2005). The authors of the studies postulate that the force response during tether growth exponentially relaxes to a speed-dependent plateau. However over the range of shear rates examined in this study, it was found that the force initially increases to a maximum value, and then decreases thereafter as the cell pivots about the tether point and moves closer to the wall.

The effect of varying the aspect ratio on the force evolution of a cell of viscosity ratio $\lambda = 1$ is shown in Figure 4.17. At the lower shear rate, the force on the tether decreases with decreasing aspect ratio. At the higher shear rate however, this effect is reversed, and the force increases with decreasing aspect ratio.

Figure 4.18 depicts the effect of shear rate on the maximum force acting on the

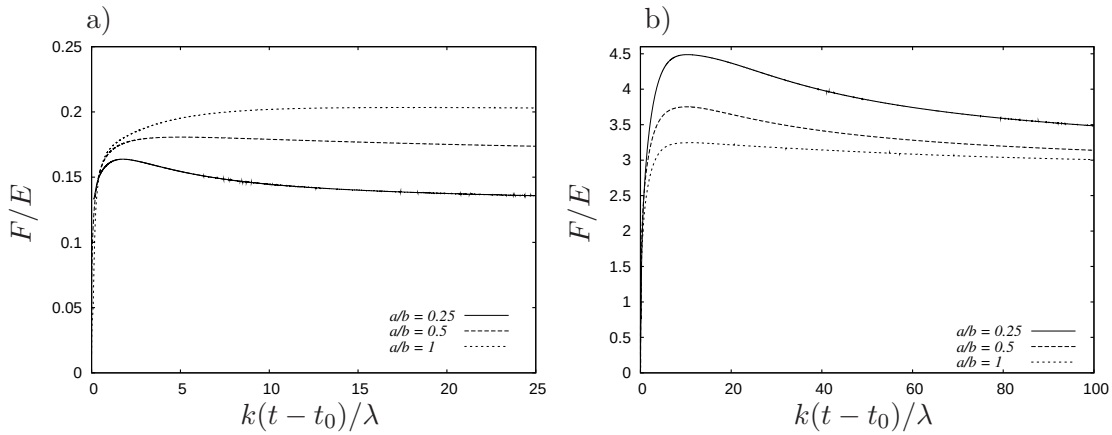

Figure 4.17: Evolution of force on tether F/E over a range of aspect ratios for a cell of viscosity ratio $\lambda = 1$ at a shear rate of a) $Ca = 0.01$, and b) $Ca = 0.25$.

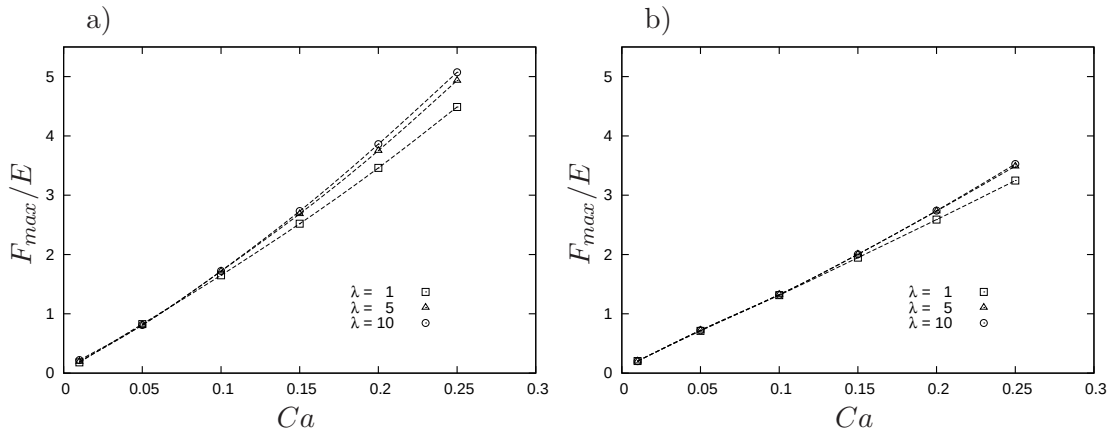

Figure 4.18: Maximum force on tether F_{max}/E as a function of shear rate for a cell with aspect ratio a) $a/b = 0.25$, and b) $a/b = 1$

tether of a cell with viscosity ratio $\lambda = 1$, and aspect ratios $a/b = 0.25$, and $a/b = 1$. For both aspect ratios, the force on the tether increases with increasing shear rate. It is also clear that the increase in force grows more rapidly as the shear rate increases. Again, the effect of varying the viscosity ratio is only evident at shear rates $Ca \gtrsim 0.1$.

4.5 Cell Velocity

The velocity of the tethered cell is shown in Figure 4.19. In this study, the velocity of the cell has been defined as the velocity of the leading edge of the cell. The velocity of the cell can also be thought of as the growth rate of the cell tether. It is clear that the cell decelerates relatively quickly after tether formation, slowing to zero forward motion in the range of $5 \leq k(t - t_0)/\lambda \leq 10$. The time to decelerate to zero velocity increases with decreasing shear rate. At higher shear rates it is evident that the cell then moves backwards at low velocity for a period before coming to a halt.

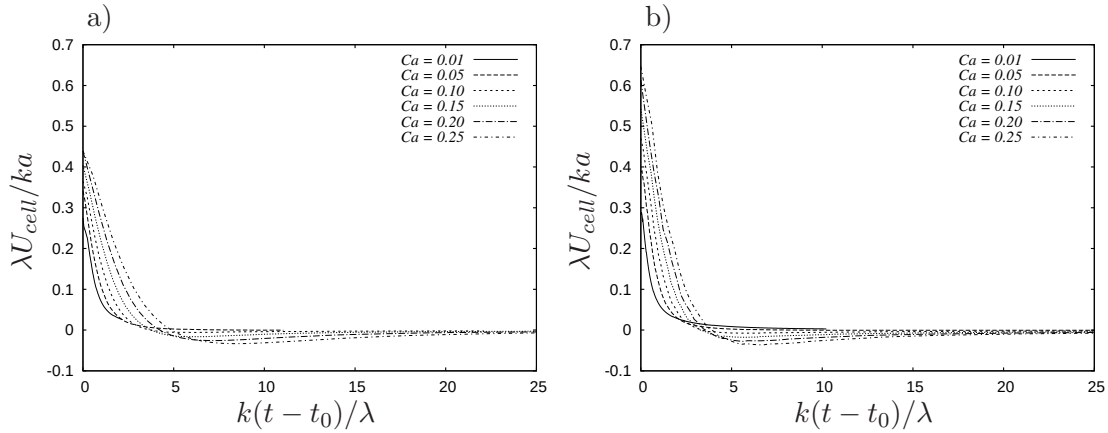

Figure 4.19: Evolution of cell velocity $\lambda U_{cell}/ka$ over a range of shear rates for a cell with aspect ratio $a/b = 1$ and viscosity ratio a) $\lambda = 1$, and b) $\lambda = 10$.

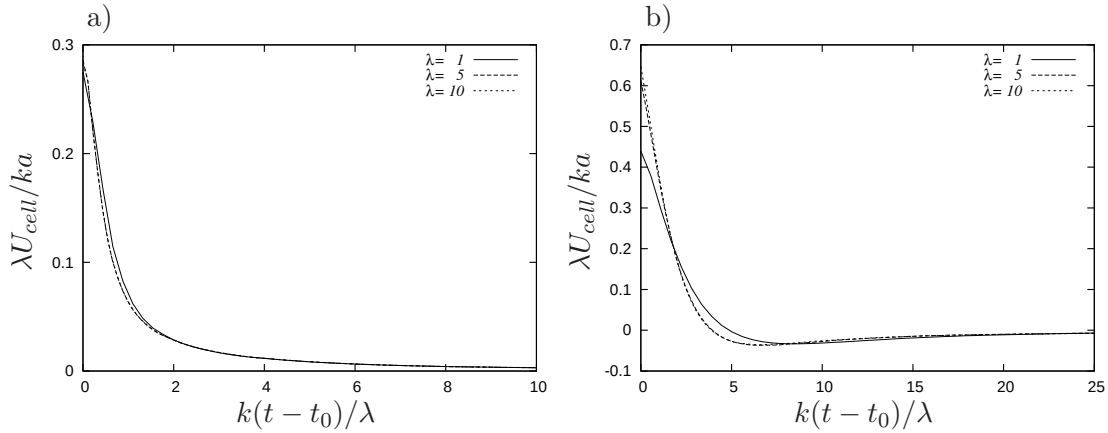

Figure 4.20: Evolution of cell velocity $\lambda U_{cell}/ka$ over a range of viscosity ratios for a cell of aspect ratio $a/b = 1$ at a shear rate of a) $Ca = 0.01$, and b) $Ca = 0.25$.

Because the relaxation time-scale is inversely proportional to the viscosity ratio λ, it follows that the velocity of the cell scales with the viscosity ratio λ. The comparison of cells of different viscosity ratios is shown in Figure 4.20 for two different shear rates $Ca = 0.01$, and $Ca = 0.25$. For the lower shear rate, the velocity nearly collapses when scaled with the viscosity ratio λ. At the higher shear rate, the velocity collapses for the two higher values of λ, but a difference can be observed with the cell of viscosity ratio $\lambda = 1$.

Figure 4.21 illustrates the effect of aspect ratio on the cell velocity. The initial cell velocity increases with aspect ratio, and the cells with lower aspect ratios take longer to slow to a halt.

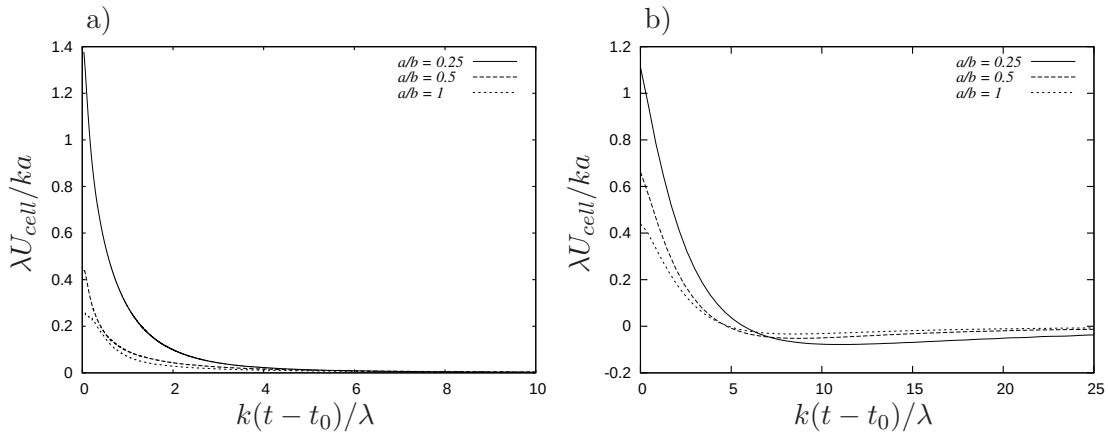

Figure 4.21: Evolution of cell velocity $\lambda U_{cell}/ka$ over a range of aspect ratios for a cell of viscosity ratio $\lambda = 1$ at a shear rate of a) $Ca = 0.01$, and b) $Ca = 0.25$.

4.6 Cell Stress

The stress distribution and corresponding cell contours are shown in Figure 4.22 for a cell with aspect ratio $a/b = 1$, viscosity ratio $\lambda = 1$, and shear rate $Ca = 0.01$. The stress distribution is plotted as a function of the monotonic parameter s used to parameterise the cell contour. The stress on the cell membrane is highest immediately after tethering, at the point of tethering ($s/s_{max} = 0$). As time evolves, the stress immediately downstream of the tether reduces dramatically. It is clear that, as time evolves, the cell pivots about the tether point and moves towards the wall. The stress in the region of the cell membrane that would contact the wall if the cell is tethered for a sufficient period of time is highlighted in red, in the range $0.25 \lesssim s/s_{max} \lesssim 0.40$. It is evident that the stress in this part of the membrane increases as the cell moves closer to the wall. The average shear stress in this region increases by 20% between $t^* = 1$ and $t^* = 20$. This increase in stress in the region that will contact the wall may provide an explanation of the observation by Ramachandran *et al.* (2004) that tether formation correlates with slower, more uniform rolling speeds. Upon tether breakage, the increase in membrane stress caused by the cell deformation in this region could lead to more ligands becoming activated, and thus a greater chance of a new tether forming as this region contacts the wall. It is also clear that the stress on the top of the cell increases as time evolves, which may increase the probability of other cells adhering to the tethered cell.

The stress on the cell membrane of the same cell in a shear flow of $Ca = 0.25$ is shown in Figure 4.22. It can be seen that the stress immediately downstream of the

a)

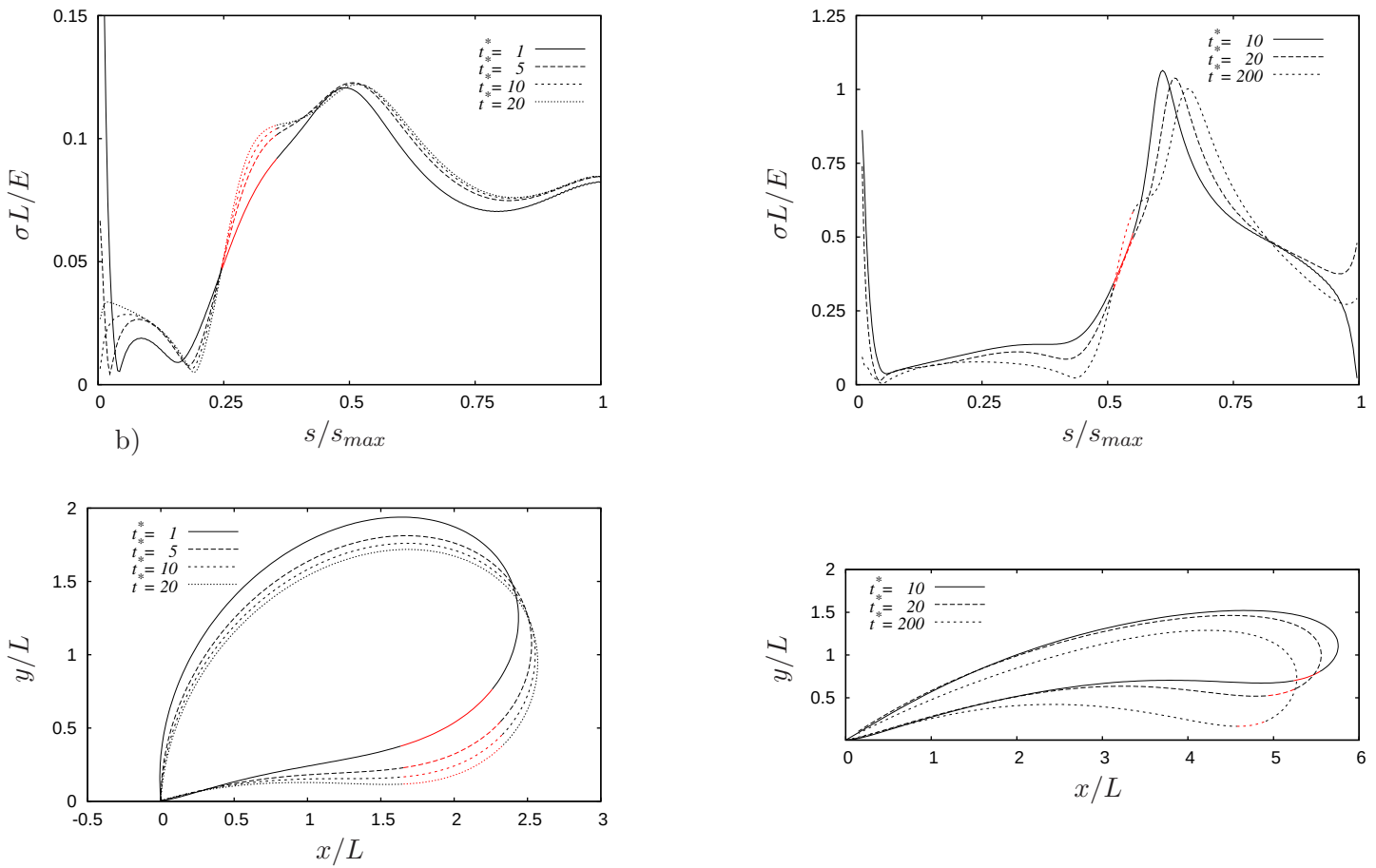

Figure 4.22: a) Principal stress distribution $\sigma L/E$ on the membrane of a cell with aspect ratio $a/b = 1$, viscosity ratio $\lambda = 1$, and shear rate of $Ca = 0.01$, at four different times, and b) corresponding cell contours. The cell contour parameter s has been normalised by its maximum value. The monotonic parameter s is zero at the tether point, increases in value in the anticlockwise direction around the cell contour and reaches a value of s_{max} back at the tether point. The regions marked in red on the stress distribution curves correspond to the regions marked in red on the cell contours.

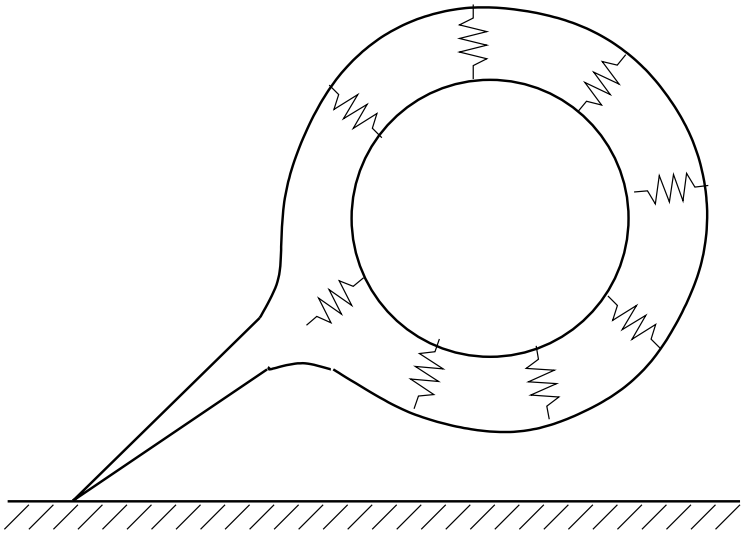

Figure 4.23: Schematic of solid body inside an elastic membrane.

tether is very high, and decreases as time evolves. The cell pivots about the tether point and approaches the wall, and the region which would come into contact increases in stress as the cell moves closer to the wall, in the range $0.5 \lesssim s/s_{max} \lesssim 0.6$. Again, a portion of the upper part of the cell contour experiences elevated levels of stress, with the average shear stress in this region increasing by 9% between $t^* = 10$ and $t^* = 200$.

4.7 Extensions to Model

To improve the physiological relevance of the tether model, several different strategies were adopted. The main drawback of the elastic fluid-filled capsule is its inability to maintain a circular shape whilst a long, thin tether is pulled from the membrane. It is reasonable to assume that the cell's internal structure plays a major role in maintaining the cell's overall shape whilst undergoing tethering. As such, an attempt was made to include the effects of an internal structure within the 2D tether model. This involved the inclusion of extra integral equations, taken from Leal & Lee (1982) and Lee & Leal (1982). The equations outlined in the study were formulated to capture the dynamics of an axisymmetric, viscous drop moving near an interface. The equations were modified in order to model a 2D solid body moving inside a closed interface (Figure 4.23). It became apparent that the size of the solid body inside the membrane was restricted to diameters of $a_{solid}/L \lesssim 0.3$. Any choice of solid body larger than this restriction severely affected the stability of the computation. The formulation of the equations was such that the membrane was attached to the wall via the tether point, and the solid

body was allowed to move freely with no forces and no torques acting on it. Thus, as the membrane deformed, the solid body eventually came into contact with the membrane. To take this model further, it will be necessary to include coupling between the elastic membrane and the solid body. This could take the form of springs connecting the two (Figure 4.23), or a repulsive force distribution on the cell membrane that acts over short distances.

Another attempt to improve the 2D tether model consisted of a cell membrane with locally varying elasticity. Evans *et al.* (2005) and Heinrich *et al.* (2005) postulate that the formation of a tether is due to membrane dissociation from the cell cytoskeleton. To try and capture this effect, a portion of the membrane was specified to have much less stiffness than the other part of the cell membrane. This can be quantified by the ratio of Young's moduli E_{tether}/E_{cell}. Very low values of this ratio resulted in prohibitively small time steps. Setting the ratio to 0.1 meant that the time step was acceptable, but the resulting membrane contour was no more physiologically consistent than the results presented in this chapter. It would be advisable to try other functions of $E(s)$, rather than the step change function used, to try and get a more physiologically consistent contour shape.

An effort was also made to implement a model of a tether with the 3D boundary-element formulation presented in Chapter 3. The unstructured formulation presented proved to be too inaccurate to allow a tether to form. It is apparent that either the resolution of the mesh or the accuracy of the method need to be improved to allow singular deformation of the cell membrane. Dynamic adaption was implemented to improve the mesh resolution in regions of high curvature. An element was split into four new elements if the quality function Q met the condition

$$Q = \kappa_{max}^2 A \geq 0.2, \tag{4.3}$$

, where κ_{max} is the maximum curvature of the six nodes on the original element, and A is the surface area of the original element. Because quadratic triangles have been used in the discretisation, the adaption of one element necessitated the adaption of all elements immediately next to the original element in order to maintain the integrity of the mesh. With this choice of quality function and threshold condition, a stable computation was not able to occur without a computationally prohibitive increase in mesh resolution. The choice of quality function Q, and the choice of threshold value, will need to be tuned in order for optimal adaption to occur and a tether to form.

4.8 Conclusions

A model of a tethered cell has been developed to investigate the effects of cell deformation, internal viscosity, and cell aspect ratio on the force, length, velocity and surface shear stress of the cell. Increasing the shear rate leads to higher overall cell deformation, longer cell lengths, larger force on the tether, and higher cell velocities, for all cells examined in the parameter space.

Immediately after tethering, the cell experiences elastic deformation and all quantities increase to a maximum value. The time taken to reach these maximum values scales inversely with the viscosity ratio λ. The elastic deformation is then damped out by the viscous response of the internal fluid of the cell, and all quantities decrease thereafter. This response is qualitatively similar to the results of the model developed by King *et al.* (2005). The cell is pulled out into the flow, and then pivots about the tether point and slowly moves towards the wall. A region of elevated shear stress has been found to occur in the part of the cell membrane that would come into contact with the wall after a sufficient period of time. This finding may in part explain the observation of Ramachandran *et al.* (2004) that membrane tether formation corresponds with cell rolling stabilisation. The ligands present on the cell membrane may become activated due to this region of elevated shear stress, increasing the chances of adhesion with the wall and subsequent tether formation at the leading edge of the cell. A region of elevated shear stress is also present on the top of the cell, which provides attractive bonding conditions for other cells to adhere to the tethered cell.

Changing the viscosity ratio of the cell was found to have negligible effect on all properties measured at low shear rates for cells with aspect ratio $a/b = 1$. Because the relaxation time-scale of the cell is proportional to $1/\lambda$, the cell velocity should scale linearly with λ. At low shear rates, $Ca \lesssim 0.05$, this was found to hold for all viscosity ratios and aspect ratios considered. At high shear rates, a difference in cell velocity can be observed at low viscosity ratios, but the difference becomes negligible as the viscosity ratio increases. At high shear rates, an increase in the cell deformation, cell length, and the force on the tether resulted from an increase in viscosity ratio. It was also found that an increase in viscosity ratio caused thinner tethers to form.

It was expected that elliptic cells would experience higher forces initially as they sit up higher into the flow, but that the force would decrease below that of a circular cell

because it would be able to lie down along the wall. At moderate to high shear rates, $Ca \gtrsim 0.05$, cells with lower aspect ratios experience greater force and deformation. At lower shear rates however, elliptic cells experience less force and deformation than circular cells, despite sitting up higher above the wall. Elliptic cells exhibited larger cell velocities than circular cells. Cells with lower aspect ratios were observed to form longer, thinner tethers, but experienced less overall deformation after long tether times. Longer tethers increase the area of the cell exposed to the wall, facilitating the formation of multiple bonds.

The model presented in this chapter is able to capture larger tether lengths and overall cell deformation consistent with experimental observations. The hypothesis tested with the model was that *the dynamics of a tethered cell are affected by the aspect ratio and the internal viscosity of the cell.* It is apparent that the aspect ratio of the cell has a marked effect on the dynamics of the cell. On the other hand, the effect of viscosity ratio appears to be minimal at viscosity ratios $\lambda > 10$. This result suggests that leukocytes, with an extremely high viscosity ratio of 10^5, would display qualitatively similar behaviour to the idealised model presented is this chapter. The only major effect of the viscosity ratio is on the time-scale of the dynamics, which appears to scale proportionally to λ.

CHAPTER 5

SINGLE CELL DYNAMICS

Previous studies have shown that cells actively change their structure during the adhesion process. Recent experiments have suggested that leukocytes undergo a shear modulus reduction of $\sim 50\%$ when activated, meaning that activated cells are more deformable than passive cells (Yap & Kamm 2005). Platelets and leukocytes have the ability to form long membrane extensions, called tethers, whilst undergoing adhesion Schmidtke & Diamond (2000), Dopheide *et al.* (2002). Ramachandran *et al.* (2004) demonstrated that the deformation of a leukocyte increased as the rolling time increased, due to the continuous forming and breaking of tethers weakening the cell structure.

Current models of cells focus mainly on cells that have already contacted the wall and initiated adhesion. As a consequence, the hydrodynamic effect of the presence of a cell in the flow on the cell itself is often neglected. The presence of a cell creates a disturbance in the flow, and this disturbance has an effect on the cell's velocity, and the velocity of the flow around it. The disturbance to the flow caused by the presence of a cell near a wall has an effect on the wall shear stress, which has implications for the activation of receptors on the vessel surface. The amount of disturbance caused by the cell is related to the amount of deformation of the cell. It is therefore of interest to quantify the effect of deformation on the cell dynamics when cells are in close proximity to a wall. In this chapter, results are presented in order to test the hypothesis that *an easily deformable cell creates hydrodynamic conditions amenable for cell adhesion.*

5.1 Solution Procedure

In this chapter, the response of the elastic membrane of the cell to the flow is described by the Skalak law (Skalak *et al.* 1973), developed to capture the mechanics of a biological

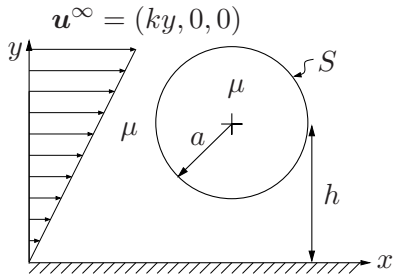

Figure 5.1: Schematic diagram of cell model above a plane wall in linear-shear flow.

membrane. Utilising the Skalak law to model the cell membrane deformation allows the amount of area dilation of the membrane to be controlled by the area dilation parameter C. A cell with a high value of area dilation parameter C resists area dilation more than a cell with a low value of C. The deformation of the cell is controlled with three independent parameters: the dimensionless shear rate, or capillary number, Ca; the area dilation parameter C; and the membrane prestress α. With a physiological wall shear-rate range of $k = 20\text{s}^{-1} - 800\text{s}^{-1}$, typical biological elastic-capillary numbers range from $Ca = 0.01 - 1$. Hence, the range of dimensionless shear rates studied in this chapter is $0.01 \leq Ca \leq 0.90$. Above $Ca = 0.90$ increased deformation results in significant mesh degradation, which could possibly be remedied by increasing the resolution of the mesh or by remeshing the interface.

The range of area dilation parameters studied in this chapter is $0.5 \leq C \leq 2.5$. Typically, a leukocyte has an area dilation parameter of $C \sim 200$. It was found that the computation time-step became prohibitively small at area dilation parameters above $C = 2.5$, dictating the range of C that could be studied. Other more accurate boundary-element formulations are only able to model values of $C \leq 10$ due to prohibitively small time-steps (Lac *et al.* 2004, Barthés-Biesel *et al.* 2002). Two values of membrane prestress are chosen, $\alpha = 0\%$ and 5%. For cells at shear rates $Ca \leq 0.10$, a stable solution cannot be reached with a membrane prestress of $\alpha = 0\%$, due to a buckling instability caused by the neglect of bending resistance (Lac *et al.* 2004).

The initially spherical cell is placed at an initial height $(h/a)_0$ above the wall, and subjected to sudden linear-shear flow at $t^* = 0$ (Figure 5.1). As time evolves the cell is allowed to deform and move away from the wall. The cell undergoes an initial, transient deformation followed by steady-state, tank-treading behaviour. Once transient effects have dissipated the velocity and other properties of the cell can be measured (Figure 5.2). The membrane moves significantly during the computation due to advection

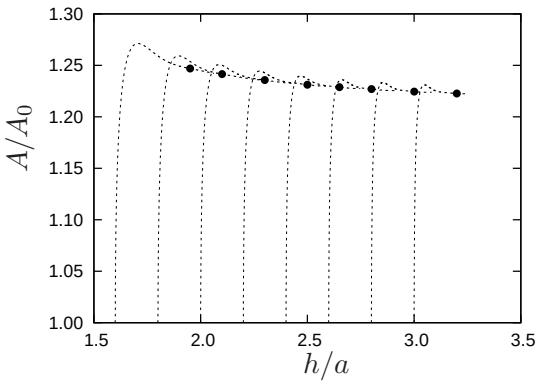

Figure 5.2: Transient evolution of surface deformation at eight different starting positions of an initially spherical neo-Hookean cell at $Ca = 0.60$. Also shown are the sampling points (●) where the area of the cell could be measured once transient effects had dissipated. A is the surface area of the deformed cell, and A_0 is the surface area of the unstressed, spherical cell. Cell height $h/a = 1$ corresponds to an undeformed spherical cell touching the wall.

and rotation about the internal fluid, leading to severe mesh degradation at $t^* \sim 15$. Because of this, the cell properties for any particular initial cell height are only able to be measured in a very narrow range of cell heights. To circumvent this problem, a range of initial cell heights is used to cover a large range of cell heights. The initial cell heights used for the results presented are $(h/a)_0 = 1.2, 1.6, 2.0, 3.0, 5.0, 7.5,$ and 10.0.

To isolate the effect of cell deformation on the cell velocity, cell shear stress and wall shear stress, another series of simulations is undertaken at a fixed cell height of $h/a = 1.25$. This ensures that the cell is kept as close to the wall as possible. The cell height can be fixed because the deformation time-scale is much smaller than the migration velocity time-scale for cells of viscosity ratio $\lambda = O(1)$ (Uijttewaal & Nijhof 1995).

5.2 Cell Deformation

Figure 5.3 shows the effect of the cell height on the reduced volume of the cell over the range of shear rates and area dilation parameters studied. The reduced volume is defined by

$$\nu = \frac{(4\pi)^{3/2}}{4\pi/3}\frac{V}{S^{3/2}}, \tag{5.1}$$

with a reduced volume of unity indicating that the cell is spherical, and a reduced volume much less than one indicating significant area dilation. For small shear rates of $Ca \leq 0.10$, very little variation from $\nu = 1$ is observed. This indicates that the cell is

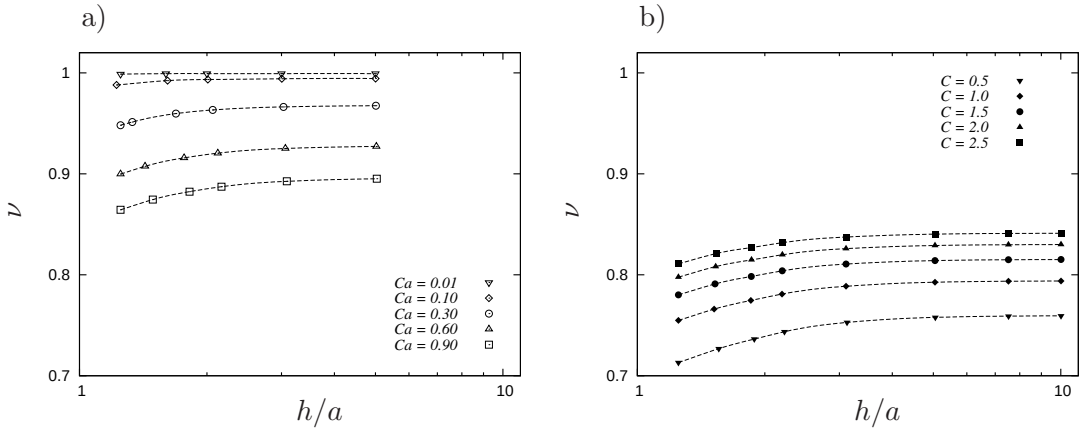

Figure 5.3: Reduced volume ν of cells as a function of cell height h/a at a) constant area dilation parameter $C = 2.5$ and membrane prestress $\alpha = 5\%$, and b) constant shear rate $Ca = 0.90$ and membrane prestress $\alpha = 0\%$. Cell height $h/a = 1$ corresponds to an undeformed spherical cell touching the wall.

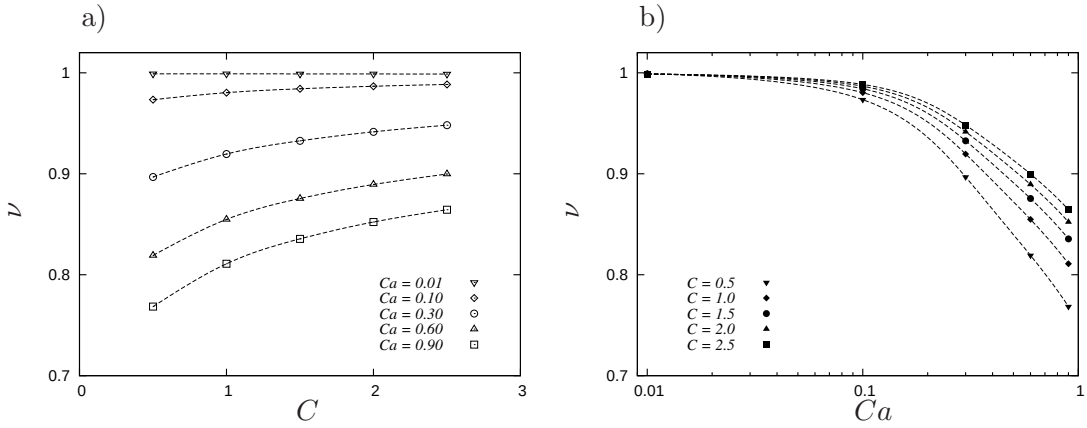

Figure 5.4: Reduced volume ν of cells with membrane prestress $\alpha = 5\%$ at a constant height $h/a = 1.25$ as a function of a) area dilation parameter C, and b) shear rate Ca.

able to retain a shape close to its reference spherical shape despite the presence of a wall in close proximity. However, at higher shear rates the cell deforms quite significantly as it moves closer to the wall. It is also apparent that a non-prestressed cell, with $\alpha = 0\%$, undergoes significantly larger deformation in comparison to a cell with a membrane prestress of $\alpha = 5\%$.

By keeping the height of the cell above the wall constant, the effect of shear rate and area dilation parameter can be elucidated further (Figure 5.4). As the shear rate increases, the effect of varying the area dilation parameter C becomes pronounced. For moderate to large shear rates of $Ca \geq 0.1$, the extent of cell deformation increases rapidly as the area dilation parameter decreases. At a shear rate corresponding to $Ca = 0.01$ however, there is virtually no measurable deformation over the range of area

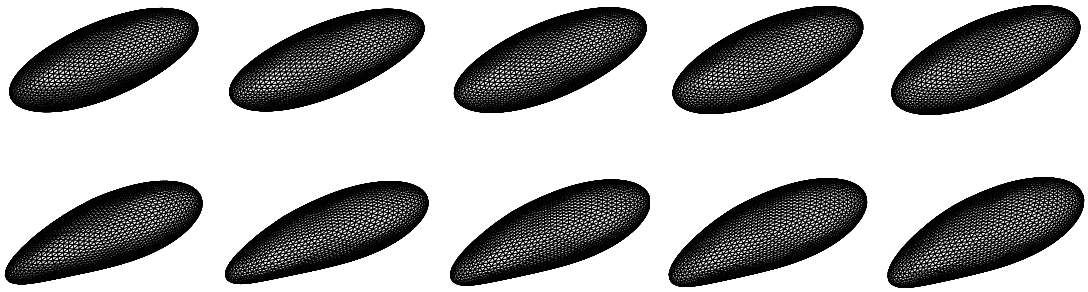

Figure 5.5: Profile of the cell in the xy plane, for a shear rate of $Ca = 0.90$ and a membrane prestress $\alpha = 0\%$, and area dilation parameters (from left to right) of $C = 0.5$, 1, 1.5, 2, and 2.5. The top row shows the cell profiles in unbounded shear flow, and the bottom row shows the cell profiles in bounded, linear shear flow at height above the wall $h/a = 1.25$. Flow is from left to right.

dilation parameters examined. The highest amount of deformation observed over the range of parameters studied was a reduced volume $\nu = 0.72$, for a non-prestressed cell with area dilation parameter $C = 0.5$ at a shear rate $Ca = 0.90$. This indicates that the cell undergoes very substantial deformation from the initial spherical shape.

The profile of a non-prestressed cell in the xy plane at a cell height of $h/a = 1.25$ is shown in Figure 5.5, for the highest shear rate of $Ca = 0.90$, and varying area dilation parameters. For comparison, the profiles of the cell in unbounded shear flow are also presented. At large cell heights the cell profile approaches the profile of the cell in unbounded shear flow. It is clear that the presence of a wall in close proximity has a significant effect on the shape of the cell. The symmetry of shape displayed by the unbounded shear flow cell profiles is broken by a narrowing of the trailing tip of the cell. This effect becomes more pronounced as the area dilation parameter decreases.

The profiles in the xy plane of cells with area dilation parameter $C = 0.5$, which allows the largest deformation, at membrane prestress $\alpha = 5\%$ and varying shear rates are shown in Figure 5.6 at a cell height of $h/a = 1.25$. It is clear that at the lowest shear rate of $Ca = 0.01$, the cell shape hardly changes from its unbounded, nearly spherical state despite the close proximity of the wall. As the shear rate increases, the distortion caused by the presence of the wall becomes increasingly pronounced, with the trailing tip of the cell becoming narrower and more elongated.

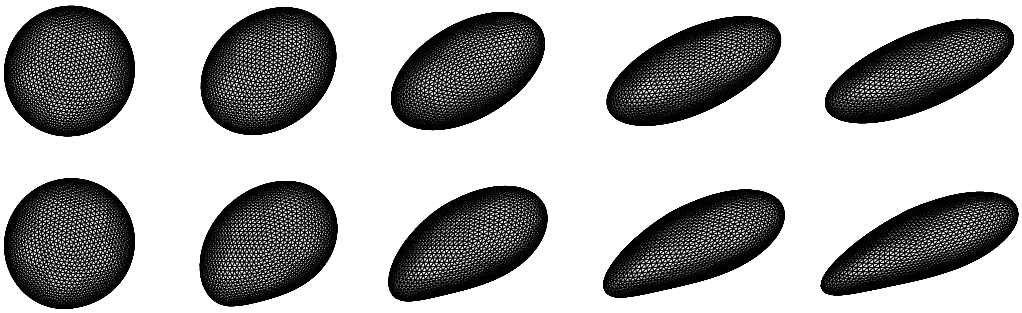

Figure 5.6: Profile of the cell in the xy plane, for an area dilation parameter of $C = 0.5$ and a membrane prestress of $\alpha = 5\%$, and shear rates (from left to right) of $Ca = 0.01$, 0.10, 0.30, 0.60, and 0.90. The top row shows the cell profiles in unbounded shear flow, and the bottom row shows the cell profiles in bounded, linear shear flow at height above the wall $h/a = 1.25$. Flow is from left to right.

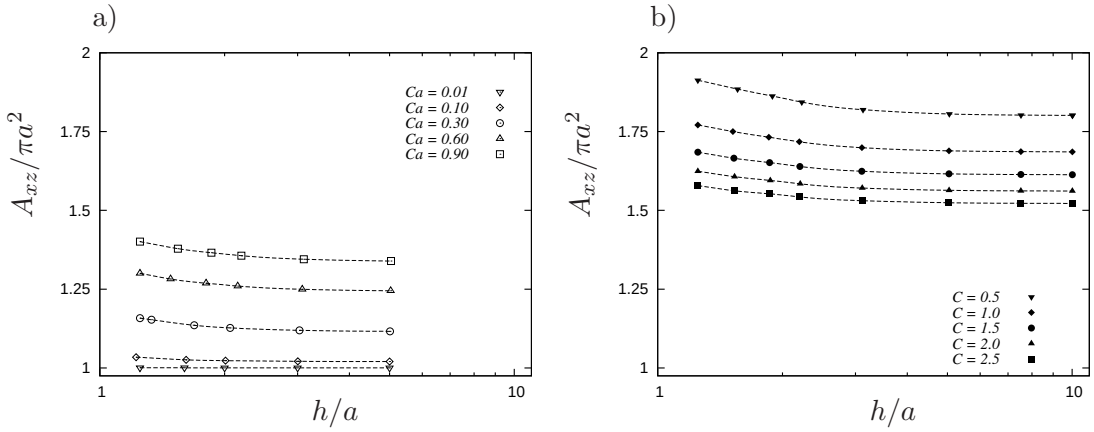

Figure 5.7: Projected area $A_{xz}/\pi a^2$ of cells in the xz plane as a function of cell height h/a at a) constant area dilation parameter $C = 2.5$ and membrane prestress $\alpha = 5\%$, and b) constant shear rate $Ca = 0.90$ and membrane prestress 0%. Cell height $h/a = 1$ corresponds to an undeformed spherical cell touching the wall.

5.2.1 Cell Footprint

An important quantity to consider when examining the effect of a wall on cell dynamics is the projected area of the cell in the xz plane, or the cell "footprint". The larger the cell footprint, the more contact area the cell exposes to the vessel wall, and therefore the cell has a greater chance of forming bonds with the vessel surface. Figure 5.7 shows the effect of cell height on the footprint of a cell over the range of shear rates, membrane prestress, and area dilation parameters studied. It is clear that the effect of cell height on the footprint of the cell is qualitatively similar to the effect on the overall cell deformation. The cell footprint increases rapidly with decreasing cell height, an effect that becomes more significant at high shear rates and low area dilation parameters (Figure 5.8). This indicates that a cell with a low shear modulus, such as an activated

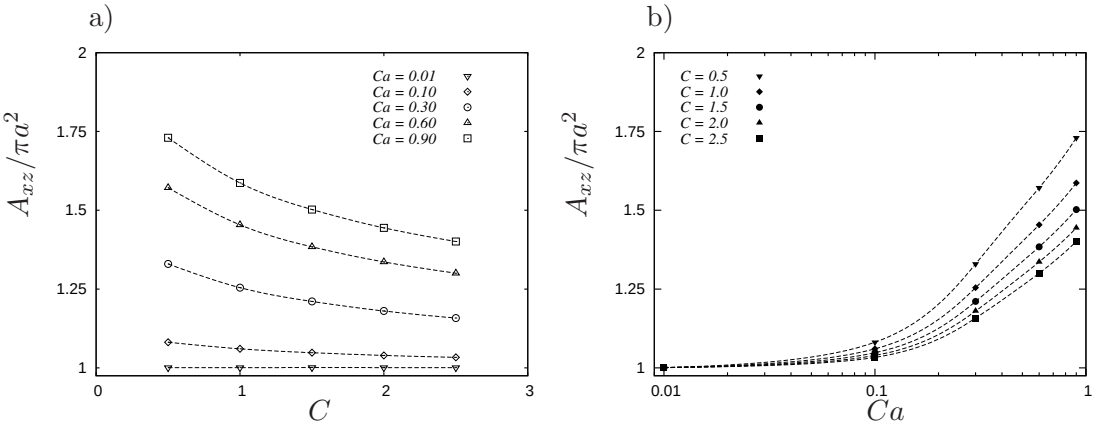

Figure 5.8: Projected area $A_{xz}/\pi a^2$ of cells in the xz plane at a constant height $h/a = 1.25$ with membrane prestress 5% as a function of a) area dilation parameter C, and b) shear rate Ca.

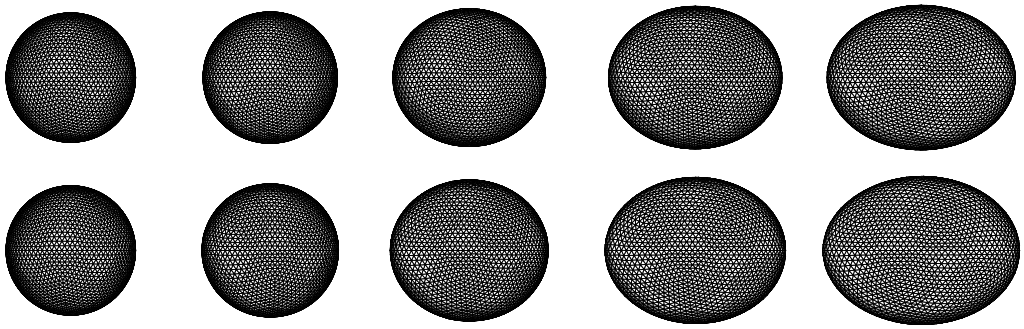

Figure 5.9: Profile of the cell in the xz plane, for an area dilation parameter of $C = 0.5$, a membrane prestress of $\alpha = 5\%$, and shear rates (from left to right) of $Ca = 0.01$, 0.10, 0.30, 0.60, and 0.90. The top row shows the cell profiles in unbounded shear flow, and the bottom row shows the cell profiles in bounded, linear shear flow at height above the wall $h/a = 1.25$. Flow is from left to right.

cell, will present a larger area to the wall, a condition beneficial to bond formation between the cell and the vessel wall. The maximum cell footprint area observed over the range of parameters studied was $\sim 95\%$ greater than that of the reference spherical shape, at a shear rate of $Ca = 0.90$, an area dilation parameter of $C = 0.5$, and a membrane prestress of $\alpha = 0\%$. As with the overall surface area, the increase in the cell footprint size is suppressed at low shear rates, and by high area dilation parameters and membrane prestressing.

Figure 5.9 shows the profiles of cells in the xy plane at varying shear rates for an area dilation parameter of $C = 0.5$, a membrane prestress of $\alpha = 5\%$, and a cell height of $h/a = 1.25$. The profiles of cells in unbounded shear flow are shown for comparison. The wall acts to increase the projected area of the cell, an effect that is most pronounced at higher shear rates. Cells at shear rate $Ca = 0.01$ display negligible

change in projected area, despite the presence of the wall. In contrast to the profiles in the xy plane, fore-aft symmetry is only minimally broken in the xz plane despite the presence of a wall.

5.3 Cell Velocity

The velocity of a cell near a plane wall is an important factor relevant to cell adhesion. Cells that move at a slower translational speed relative to the wall are more likely to form bonds with the surface. The difference between the translational velocity of the cell and the velocity of the undisturbed flow can be measured using the slip velocity, defined in equation 3.55. A large, positive slip velocity means that the cell moves more slowly relative to the wall. The cell velocity normal to the wall, or migration velocity, is also of interest.

5.3.1 Slip Velocity

The slip velocity of the cell is affected significantly by the cell height (Figure 5.10). As the cell moves closer to the wall, the cell slip velocity for all shear rates and area dilation parameters increases. As the deformation of the cell increases, the cell aligns itself with the fluid streamlines, thus offering less resistance to the flow and a smaller slip velocity results (Figure 5.11). At large cell heights, the slip velocities of all cells appear to vary inversely with the square of h/a. However, at close cell heights the rate of increase of the slip velocity decreases. This can be attributed to the changing shape of the cell: the trailing edge aligns itself with the flow, decreasing the resistance of the cell to the flow faster than the resistance of the wall on the cell. As the shear rate decreases, the cell remains closer to its reference spherical shape, and the cell slip velocity approaches the analytical solution for a solid sphere derived by Goldman *et al.* (1967) (Equation 2.10). However, even at the lowest shear rate of $Ca = 0.01$, there is still slight deviation from the analytical result. This indicates that the very slight deformation experienced by the cell at low shear rates has an effect on the velocity of the cell.

At shear rates of $Ca = 0.10$ and $Ca = 0.30$, a comparison between the slip velocity of a cell with area dilation parameter $C = 2.5$ and the slip velocity of a liquid drop is shown in Figure 5.12, using the numerical results of Uijttewaal *et al.* (1993). It is clear that over the range of cell heights studied, the cell slip velocity is higher than that of

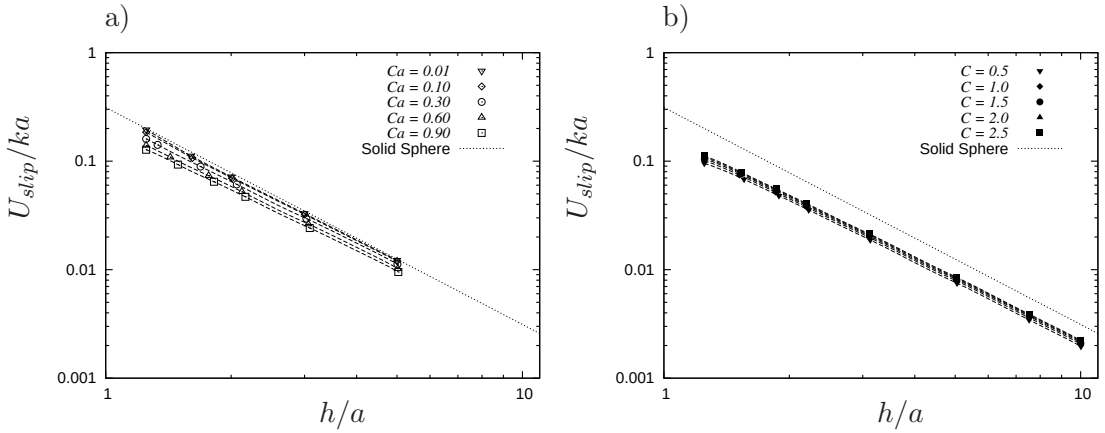

Figure 5.10: Slip velocity U_{slip}/ka of cells as a function of cell height h/a at a) constant area dilation parameter $C = 2.5$ and membrane prestress $\alpha = 5\%$, and b) constant shear rate $Ca = 0.90$ and membrane prestress $\alpha = 0\%$. The dotted line shows the analytical solution for the slip velocity of a rigid sphere derived by Goldman *et al.* (1967). Cell height $h/a = 1$ corresponds to an undeformed spherical cell touching the wall.

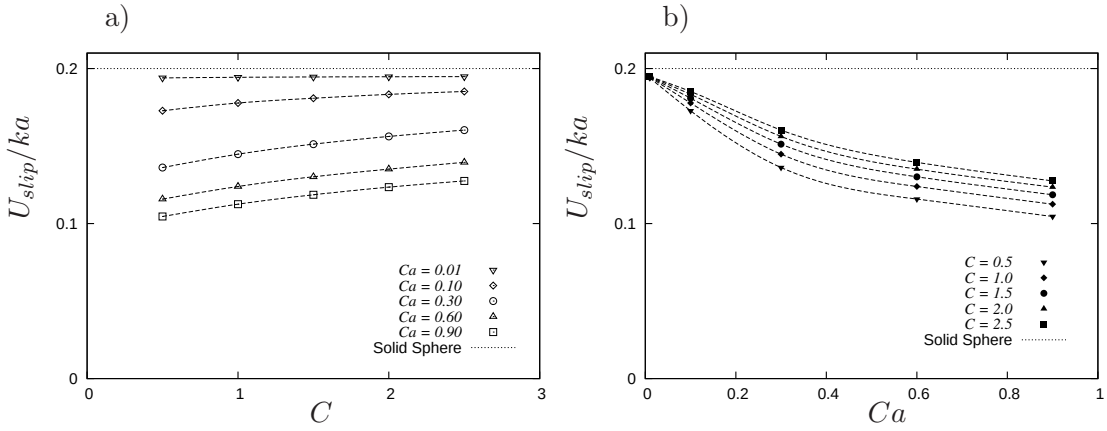

Figure 5.11: Slip velocity U_{slip}/ka of cells at a constant height $h/a = 1.25$ and membrane prestress $\alpha = 5\%$ as a function of a) area dilation parameter C, and b) shear rate Ca. The dotted line shows the analytical solution for the slip velocity of a rigid sphere derived by Goldman *et al.* (1967).

the liquid drop for both shear rates.

5.3.2 Migration Velocity

The migration velocity of the cell follows a similar trend to the slip velocity as the cell is moved closer to the wall (Figure 5.13). The migration velocity increases as the cell is moved closer to the wall for all properties, similar to the behaviour of the slip velocity. The rate of increase lessens at very small cell heights for moderate to high shear rates and all area dilation parameters, which can also be attributed to the tip that forms at the trailing edge of the cell. In contrast to the behaviour of the slip velocity of the cell, the migration velocity decreases as the deformation increases, whether by variation in

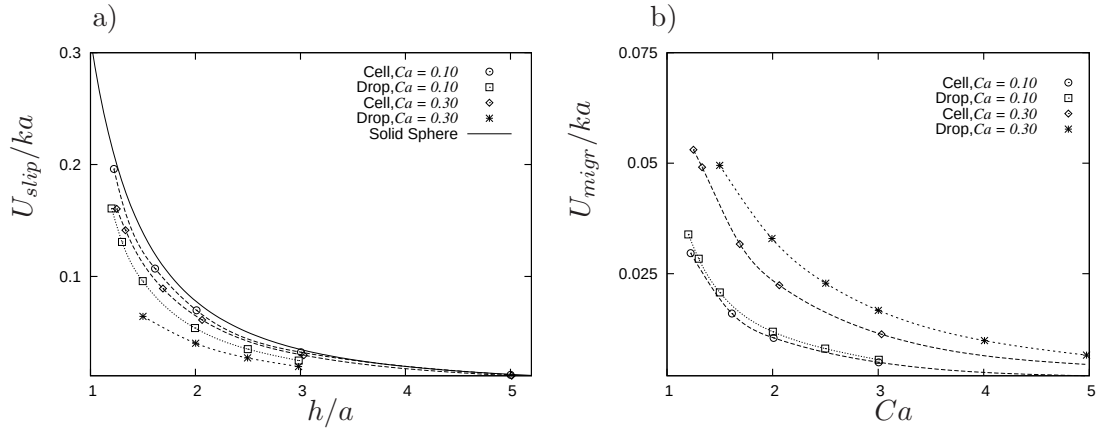

Figure 5.12: Comparison between a cell of area dilation parameter $C = 2.5$ and membrane prestress $\alpha = 5\%$, and a liquid drop of a) slip velocity U_{slip}/ka, and b) migration velocity U_{migr}. The liquid drop data is taken from the numerical results of Uijttewaal *et al.* (1993). Cell height $h/a = 1$ corresponds to an undeformed spherical cell touching the wall.

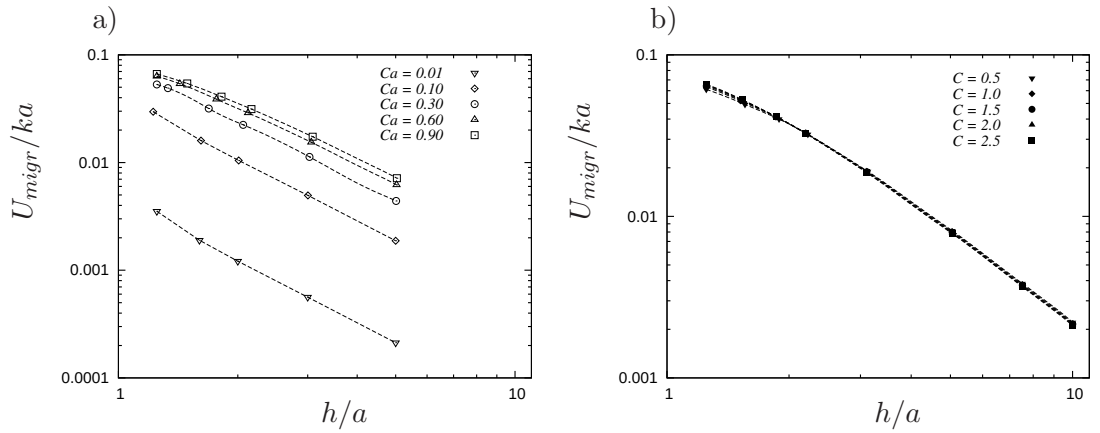

Figure 5.13: Migration velocity U_{migr}/ka of cells as a function of cell height h/a at a) constant area dilation parameter $C = 2.5$, and b) constant shear rate $Ca = 0.90$. Cell height $h/a = 1$ corresponds to an undeformed spherical cell touching the wall.

shear rate, in area dilation parameter, or in membrane prestress. (Figure 5.14). This is consistent with the expectation that as the cell shape approaches its reference spherical shape, the cell migration velocity goes to zero due to the reversibility of Stokes flow. The effect of large deformation on the migration velocity appears to be less significant than the effect on the slip velocity, with little change with a variation in either shear rate or area dilation parameter at large values of each.

A comparison can be made between the migration velocity of a cell with area dilation parameter $C = 2.5$ and membrane prestress $\alpha = 5\%$, and that of a liquid drop at shear rates $Ca = 0.10$ and $Ca = 0.30$. Over the range of cell heights examined, the migration velocity of the cell is less than that of the liquid drop at both shear rates.

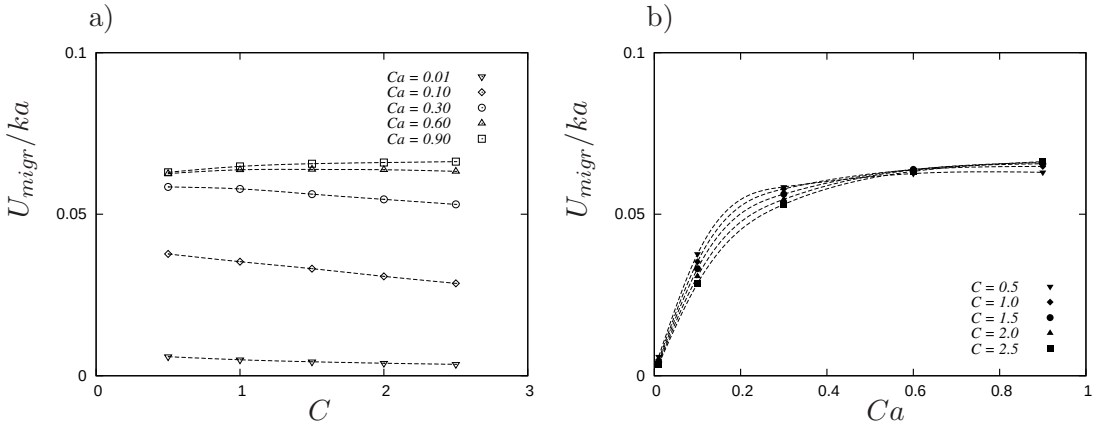

Figure 5.14: Migration velocity U_{migr}/ka of cells with membrane prestress $\alpha = 5\%$ at a constant height $h/a = 1.25$ as a function of a) area dilation parameter C, and b) shear rate Ca.

5.4 Shear Stress

A critical property mediating cell adhesion is shear stress, both on the cell surface and on the vessel wall. Receptors on both surfaces are activated over specific ranges of shear stress. As such it is important to quantify the shear stress on a cell in close proximity to a wall. It is also of interest to characterise the effect of the cell on the shear stress distribution on the vessel wall.

5.4.1 Stress on Cell

The shear stress varies widely over the surface of a cell, even in unbounded flow. The maximum shear stress is observed to occur at the trailing tip of the cell when in close proximity to the wall. The use of an unstructured boundary-element formulation in the simulations leads to noise in the shear stress distribution on the cell membrane. To minimise the effect of this numerical error, it is more accurate to consider the mean shear stress, rather than the maximum shear stress, as a measure of the stress on the cell. The change in mean shear stress on a cell as a function of cell height is shown in Figure 5.15. The change in shear stress refers to the difference in the shear stress of the deformed cell and its reference spherical shape. This only has an effect on the prestressed cells, as the reference spherical shapes of these cells are under a finite amount of stress.

It is clear that as the cell approaches the wall, the mean shear stress on the surface of the cell increases significantly at moderate to high shear rates. At a shear rate of $Ca = 0.01$, the cell experiences very little shear stress, even with a wall in close

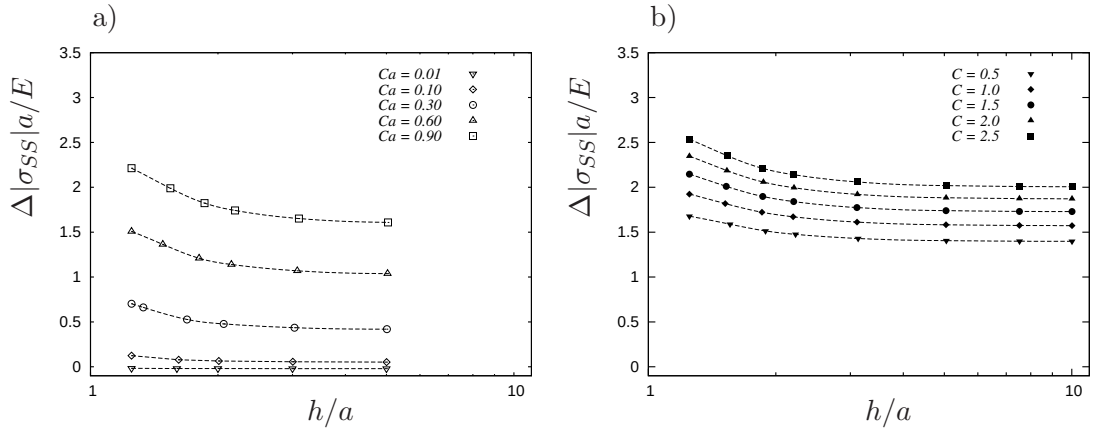

Figure 5.15: Increase in mean shear stress $\Delta|\sigma_{SS}|a/E$ on cells as a function of cell height h/a at a) constant area dilation parameter $C = 2.5$ and membrane prestress $\alpha = 5\%$, and b) constant shear rate $Ca = 0.90$ and membrane prestress $\alpha = 0\%$. $\Delta|\sigma_{SS}|a/E$ refers to the difference in mean shear stress between the deformed and reference shapes of the cell. Cell height $h/a = 1$ corresponds to an undeformed spherical cell touching the wall.

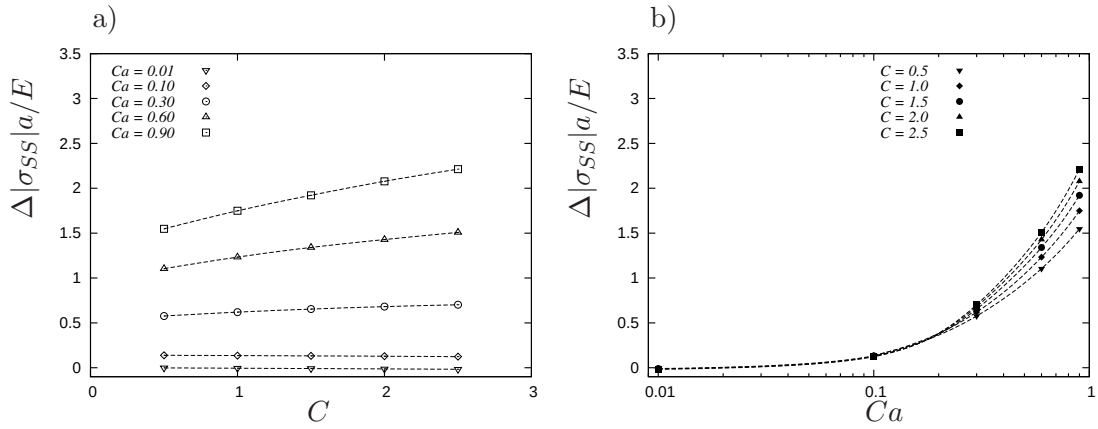

Figure 5.16: Increase in mean shear stress $\Delta|\sigma_{SS}|a/E$ on cells with membrane prestress $\alpha = 5\%$ at a constant height $h/a = 1.25$ as a function of a) area dilation parameter C, and b) shear rate Ca. $\Delta|\sigma_{SS}|a/E$ refers to the difference in mean shear stress between the deformed and reference shapes of the cell.

proximity. This is consistent with the experimental observation that cells at low shear rates do not activate due to the absence of an external shear stress trigger.

As the shear rate increases, the mean shear stress on the cell increases significantly (Figure 5.16). The significant increase with shear rate has ramifications for activated cells, which experience a reduction in shear modulus, and thus an increase in shear rate. This suggests that an activated cell will experience much higher surface shear stress than an unactivated cell, a condition amenable to cell adhesion. Interestingly, the mean shear stress on the surface of the cell decreases with decreasing area dilation parameter.

5.4.2 Stress on Wall

The presence of a cell in close proximity to a wall creates a marked effect on the shear stress distribution on the wall surface. Figure 5.17 shows the contours of principal shear stress on the wall with a cell, of area dilation parameter $C = 2.5$ and membrane prestress $\alpha = 5\%$, at a constant height $h/a = 1.25$, over the range of shear rates examined. In the absence of the cell, the wall experiences a dimensionless shear stress of 1. For all shear rates, there is a region of elevated stress upstream of the cell, a region of reduced stress immediately below the cell, and a region of elevated stress downstream of the cell. The maximum shear stress experienced by the wall occurs in the region of elevated stress upstream of the cell. The minimum and maximum shear stress on the wall decrease and increase respectively as the shear rate decreases. The existence of a region of elevated shear stress on the wall immediately downstream of the cell is beneficial for the activation of receptors on the vessel wall in preparation for cell contact with the wall. Similarly, a region of elevated shear stress upstream of the cell may in turn be beneficial for upstream cells.

At the lowest shear rate of $Ca = 0.01$, the shear stress displays symmetry in the plane perpendicular to the flow direction. The regions of elevated stress at this shear rate extend approximately 3 cell diameters upstream and downstream of the cell. As the shear rate increases, the region of influence on the shear stress upstream of the cell moves upstream and increases in size. In contrast, an increase in shear rate has a minimal effect on the size of the region of influence downstream of the cell. To illustrate this more clearly, the regions of the wall which experience levels of shear stress at least 5% greater than ambient levels are shown in Figure 5.17.

Figure 5.18 shows the distribution of wall shear stress on the flow axis immediately below the cell. Varying the shear rate has an effect on both the magnitude and position of the maximum and minimum shear stress. As the shear rate increases, the maximum shear stress position upstream of the cell moves upstream, and the minimum shear stress position moves downstream. The maximum shear stress position downstream of the cell remains largely invariant to the shear rate. The maximum shear stress upstream of the cell increases as the shear rate decreases, until $Ca = 0.10$, where it is at a maximum. Further decreasing the shear rate to $Ca = 0.01$ decreases the magnitude of the maximum stress upstream of the cell. In contrast, the minimum shear stress, and the maximum shear stress downstream of the cell, increase monotonically with decreasing shear rate.

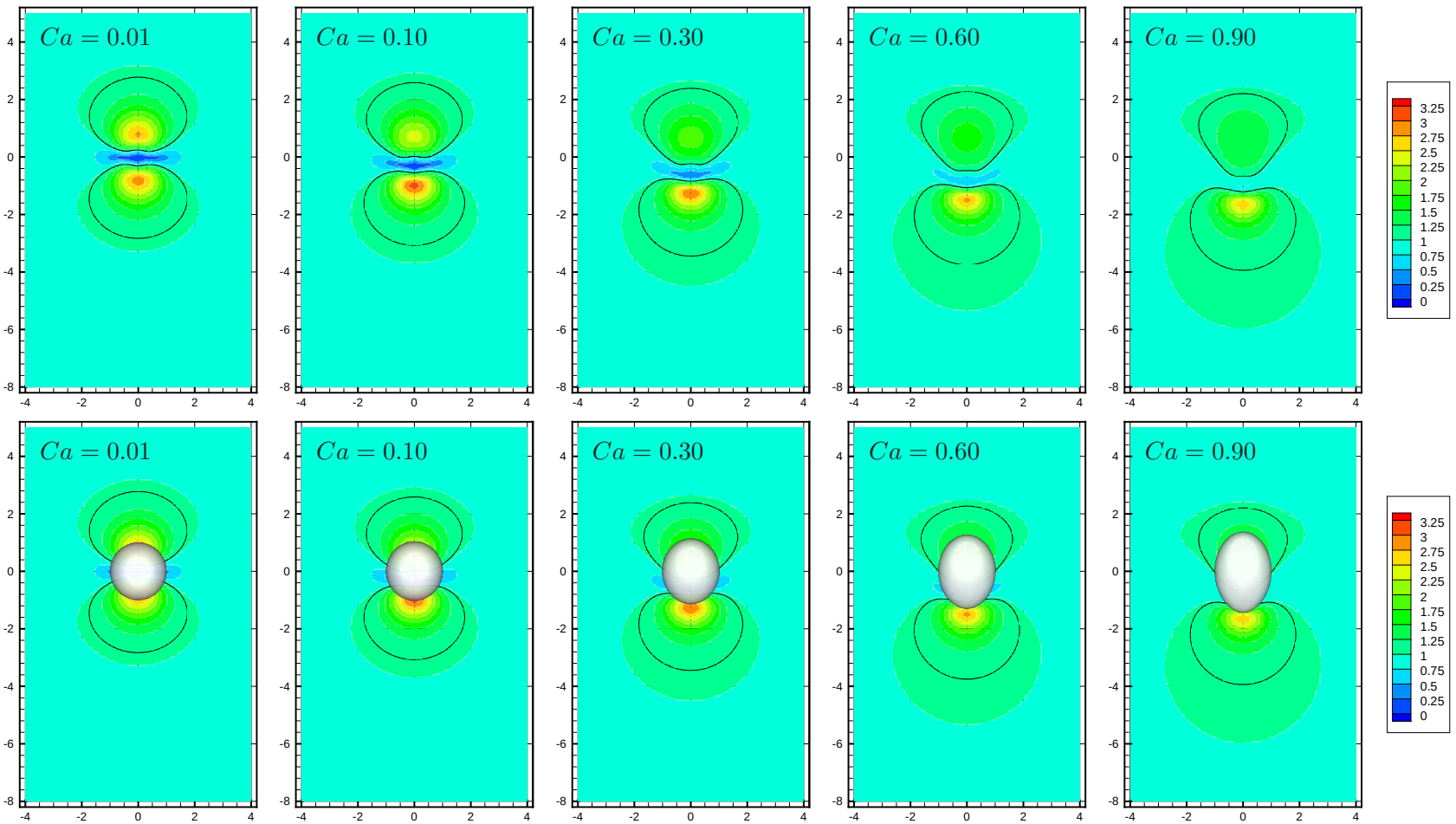

Figure 5.17: Contours of principal shear stress $\sigma_{SS}a/E$ on the wall surface at shear rates of (left to right) $Ca = 0.01$, 0.10, 0.30, 0.60, and 0.90 with a cell of area dilation parameter $C = 2.5$ and membrane prestress $\alpha = 5\%$ at height $h/a = 1.25$. The bottom row includes the cell position. The black lines indicate regions on the wall with shear stress 5% above ambient levels. Flow is from bottom to top.

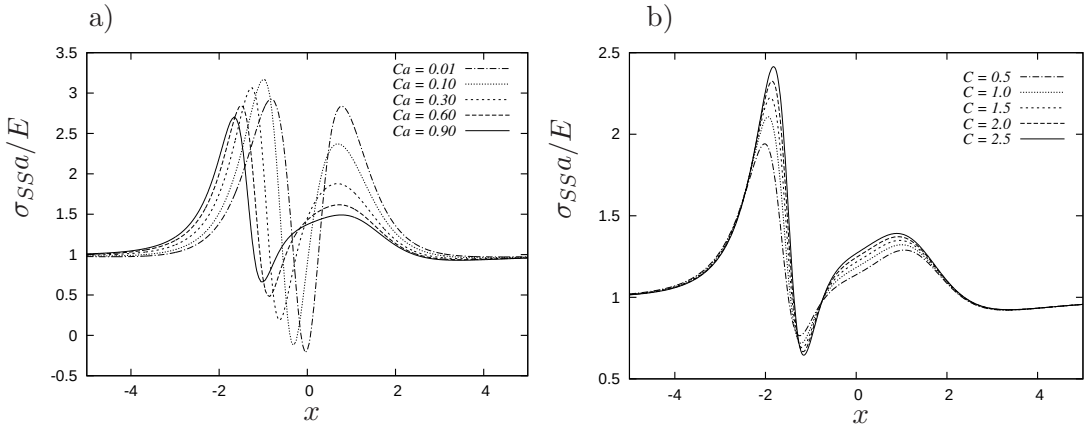

Figure 5.18: Variation in principal shear stress $\sigma_{SS}a/E$ in the flow direction x on the wall below the centre of the cell at height $h/a = 1.25$ in the flow direction x, for a) constant area dilation parameter $C = 2.5$ and membrane prestress $\alpha = 5\%$, and b) constant shear rate $Ca = 0.90$ and membrane prestress $\alpha = 0\%$.

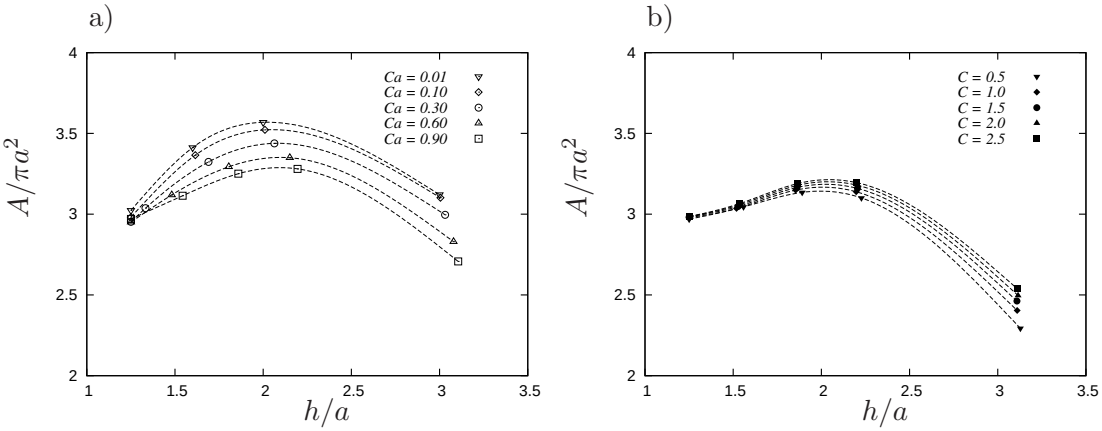

Figure 5.19: Area of wall $A/\pi a^2$ downstream of the cell exposed to a principal shear stress $\sigma_{ss}a/E$ of 5% above the ambient level as a function of cell height above the wall h/a for a cell at a) constant area dilation parameter $C = 2.5$ and membrane prestress $\alpha = 5\%$, and b) constant shear rate $Ca = 0.90$ and membrane prestress $\alpha = 0\%$. Cell height $h/a = 1$ corresponds to an undeformed spherical cell touching the wall.

Varying the area dilation parameter has no effect on the positions of the maximum and minimum stresses. The maximum stresses downstream and upstream of the cell, and the minimum stress, all increase with increasing area dilation parameter.

The area of the region of elevated shear stress downstream of the cell as a function of cell height is shown in Figure 5.19. It can be seen that the area of elevated shear stress downstream of the cell increases as the cell approaches the wall, until a maximum is reached when the cell is located at a distance $h/a \sim 2$ above the wall. As the cell moves closer to the wall, the region of influence downstream of the cell then decreases in area. When the cell is located at distance of $h/a \sim 3$ above the wall, the effect of varying

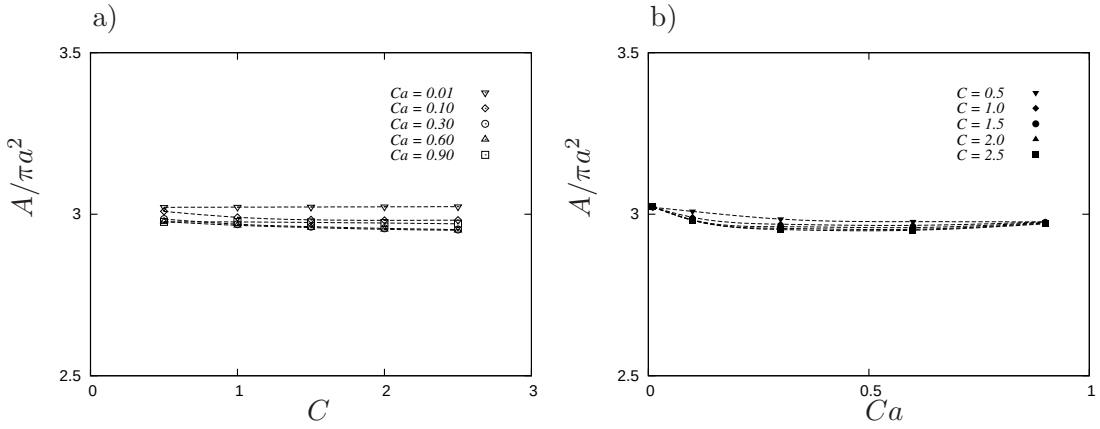

Figure 5.20: Area of wall $A/\pi a^2$ downstream of the cell exposed to a principal shear stress $\sigma_{ss}a/E$ of 5% above the ambient level for a cell at height $h/a = 1.25$ and membrane prestress $\alpha = 5\%$ as a function of a) area dilation parameter C, and b) shear rate Ca.

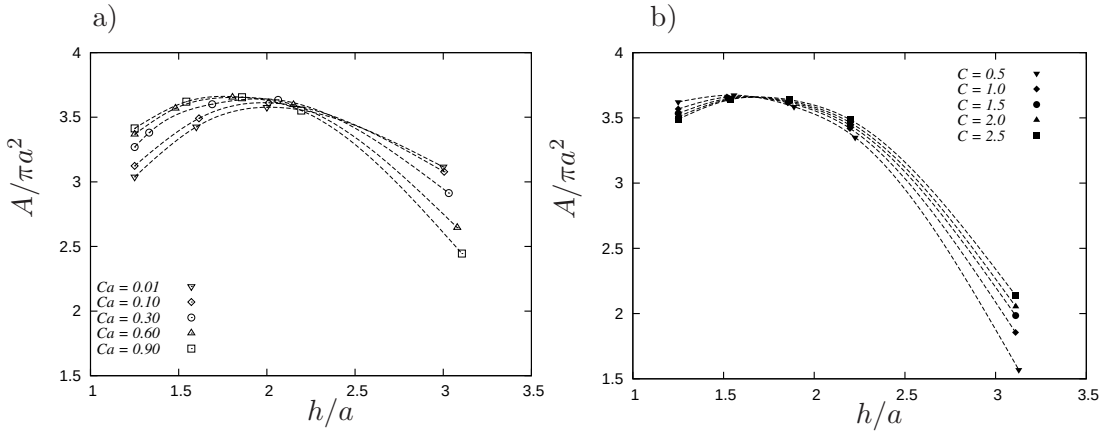

Figure 5.21: Area of wall $A/\pi a^2$ upstream of the cell exposed to a principal shear stress $\sigma_{ss}a/E$ of 5% above the ambient level as a function of cell height above the wall h/a for a cell at a) constant area dilation parameter $C = 2.5$ and membrane prestress $\alpha = 5\%$, and b) constant shear rate $Ca = 0.90$ and membrane prestress $\alpha = 0\%$. Cell height $h/a = 1$ corresponds to an undeformed spherical cell touching the wall.

shear rate and area dilation parameter is evident. At close cell heights however, the area of elevated shear stress becomes independent of either the shear rate or the area dilation parameter. This effect can be seen clearly in Figure 5.20, with little variation in area over a range of shear rates and area dilation parameters when the cell is at height $h/a = 1.25$.

Figure 5.21 shows the effect of cell height on the area of the elevated stress region upstream of the cell. The change in the area of elevated stress upstream of the cell behaves similarly to that of the area downstream of the cell. The area increases with decreasing cell height, until a maximum is reached. The area of the elevated stress

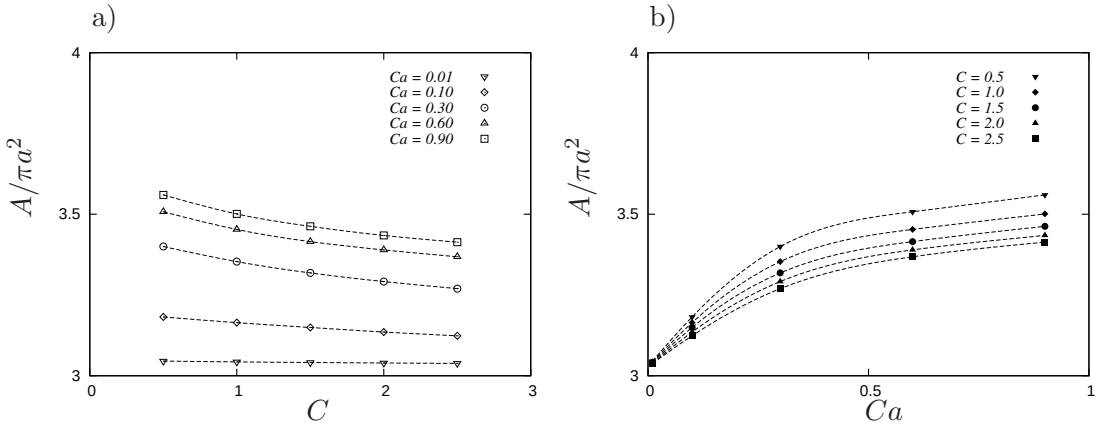

Figure 5.22: Area of wall $A/\pi a^2$ upstream of the cell exposed to a principal shear stress $\sigma_{ss}a/E$ of 5% above the ambient level for a cell at height $h/a = 1.25$ and membrane prestress $\alpha = 5\%$ as a function of a) area dilation parameter C, and b) shear rate Ca.

region then decreases as the cell height decreases further. As the shear rate increases, the position of the cell that corresponds to the maximum area of elevated stress moves closer to the wall. When the cell is at height $h/a \sim 3$ above the wall, the effect of varying both the shear rate and the area dilation parameter is significant, and the cells with less deformation affect a larger region of the wall. At closer cell heights this effect is reversed, and the cells at higher shear rates and lower area dilation parameters have a larger effect on the wall (Figure 5.22).

5.5 Extensions to Model

In order to make the 3D formulation more physiologically consistent, an attempt was made to implement bending resistance on the cell surface. The contribution of bending resistance to the surface traction Δf_b can be written as (Seifert 1999, Vlahovska & Gracia 2007)

$$\Delta \boldsymbol{f}_b = E_b(4\kappa^3 - 4\kappa H + 2\Delta_s\kappa)\boldsymbol{n}, \tag{5.2}$$

where E_b is the elastic bending modulus, κ is the mean curvature, Δ_s is the surface Laplacian operator (more generally known as the Laplace-Beltrami operator), and H is the Gaussian curvature. The Gaussian curvature of a surface can be considered constant if no topological change, such as tearing or gluing, occurs. The surface Laplacian of the mean curvature can be written as

$$\Delta\kappa = \frac{1}{\sqrt{|g|}}\partial_i\left(\sqrt{|g|}g^{ij}\partial_j\kappa\right), \tag{5.3}$$

where g^{ij} is the metric tensor of the surface, and g its determinant.

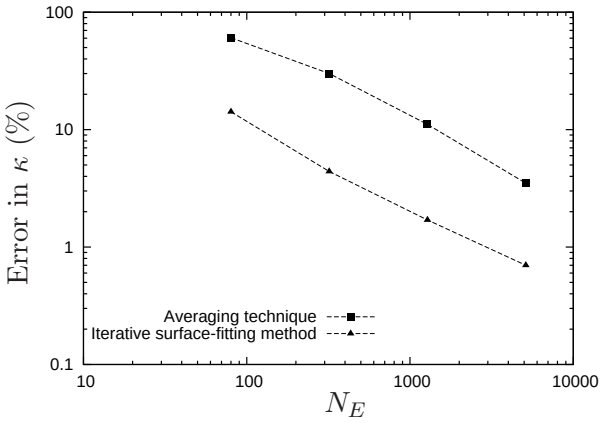

Figure 5.23: Comparison of the percentage RMS error in the calculation of curvature κ between the unstructured formulation of Ramanujan & Pozrikidis (1998) and the surface-fitting technique of Zinchenko *et al.* (1997), as a function of the number of elements N_E. Results are presented on a prolate ellipsoid with axes ratios of $b/a = 0.5$, and $c/a = 2$.

Because the surface Laplacian of the curvature is effectively a fourth-order surface derivative, it is clear that a successful implementation of bending resistance requires a very accurate estimation of the surface mean curvature. The second-order unstructured discretisation presented in Chapter 3 is not able to give an accurate description of equation 5.2. It is therefore necessary to implement an improved estimation of the surface in order to accurately model bending resistance. An improved estimation of the cell surface can be achieved by implementing an iterative surface-fitting technique developed by Zinchenko *et al.* (1997). The technique involves fitting a local quadratic surface $z' = f(x', y')$ to a node O and its immediately neighbouring nodes. Initially, the z' axis is aligned with a best guess for the normal to the surface at the node O. A suitable choice of best guess is the normal calculated at the previous time-step. A quadratic surface passing through O is then found using the least-squares method. The normal to this quadratic surface is then used as the new z' axis, and the process is repeated until the difference between successive normals falls below a threshold value. Once the iterative process is complete, an improved estimate of the surface normal and mean curvature follow. A comparison between the curvature error from the unstructured formulation presented in Chapter 3, which involves the averaging of the curvatures on elements sharing a common node, and the iterative surface-fitting method is shown in Figure 5.23. It is clear that the local surface-fitting technique gives a much more accurate approximation of the mean curvature. However, because the local surface is C_2

continuous, the surface Laplacian of the curvature in equation 5.2 cannot be computed. An attempt was made to fit a local quadratic function to the curvature at node O and its immediate neighbouring points, in the same fashion as the surface-fitting technique outlined above. This allowed equation 5.3 to be evaluated, and an approximation of equation 5.2 to be found. However, the implementation of this approximation did not lead to a stable, accurate computation. Another approach to implementing bending resistance, albeit less accurate, was outlined by Pozrikidis (2001*a*), based on the unstructured discretisation outlined in Chapter 3. An unsuccessful attempt was made to implement this alternative approach.

To implement bending resistance successfully, it is apparent that a much more accurate representation of the cell surface is required. Kessler *et al.* (2008) used a spectral boundary-element formulation to successfully capture bending resistance in an elastic capsule. The formulation of Kessler *et al.* (2008) would not however be able to cope with the large deformations apparent close to a wall, or whilst undergoing tethering. There is benefit in exploring further the implementation of bending resistance into an unstructured formulation. It may be possible to use the surface-fitting algorithm of Zinchenko *et al.* (1997) to significantly improve the accuracy of the bending-resistance approximation developed by Pozrikidis (2001*a*).

5.6 Conclusions

Results have been presented in this chapter in order to quantify the effect of cell deformation on cell dynamics near a wall. Specifically the effects of shear rate, area dilation parameter and membrane prestress on the footprint of the cell, the slip and migration velocities of the cell, and the shear stresses present on both the cell and wall have been presented. The range of shear rates examined is $0.01 \leq Ca \leq 0.90$, almost two orders of magnitude. The range of area dilation parameters examined is $0.5 \leq C \leq 2.5$, and the closest cell height above the wall studied is $h/a = 1.25$. The membrane prestresses examined are $\alpha = 0\%$ and 5%.

Over the range of parameters studied, it was found that less deformable cells offer more resistance to the flow, which leads to higher slip velocities and lower migration velocities. Both of these conditions are advantageous in terms of approach to the vessel wall. Unactivated cells would therefore be able to more easily come into close proximity to the vessel wall when compared to an activated, more deformable cell. The greater

resistance to the flow of less deformable cells leads to greater disturbance of the flow around the cell, causing significant changes to the shear stress on the wall surface. At cell heights of $h/a \gtrsim 1.25$, less deformable cells cause a larger region of elevated shear stress on the wall surface downstream of the cell. This suggests that unactivated cells also have an advantage in "preparing" the vessel wall for adhesion.

On the other hand, easily deformable cells present a much higher surface to the vessel wall. An activated cell would therefore be able to come into contact with more wall surface, thus enhancing the probability of multiple bond formation. It was also found that easily deformable cells display much higher shear stresses on the cell surface. This implies that the receptors on the activated cell surface would become activated, ready to form bonds with the vessel wall. For close cell heights of $h/a < 2$, it was observed that a larger region of elevated stress was present upstream to an easily deformable cell. This would be beneficial to other cells upstream, and enhance the probability of multiple cell adhesion. At close cell heights it can also be concluded that the region of elevated wall shear stress downstream of the cell becomes independent of the amount of cell deformation.

From the results presented, the hypothesis that *an easily deformable cell creates hydrodynamic conditions amenable for cell adhesion* has been shown to be too general a statement. It is clear that an easily deformable cell does create hydrodynamic conditions amenable for cell adhesion, but only at close cell heights. Closer to the wall, an easily deformable cell experiences higher shear stress, and presents a greater surface area to the vessel wall. At higher cell heights however, less deformable cells are able to approach the wall more easily, with a higher slip velocity and a lower migration velocity. It can be concluded that it is hydrodynamically advantageous for a cell to approach the wall in its unactivated state. However, once the cell is in close proximity to the wall, activation of the cell would then be hydrodynamically beneficial with regard to cell adhesion.

CHAPTER 6

MULTIPLE CELL DYNAMICS

There is evidence to suggest that the presence of another cell improves the cell adhesion process. King *et al.* (2001), King & Hammer (2001*a*,*b*) and Pappu & Bagchi (2008) demonstrated that slower, more uniform cell rolling existed when multiple cell adhesion was considered for both rigid and deformable cells. These studies focused on adhering cells, not on the hydrodynamic conditions in the lead up to adhesion. Previous numerical studies have examined the dynamics of two bodies in unbounded shear flow for elastic capsules (Lac *et al.* 2007), and liquid drops (Singh & Sarkar 2009). No such study exists in bounded flows. The previous chapter has shown that the presence of a wall has a non-trivial effect on the deformation and velocities of a cell. It is reasonable to assume that the presence of a wall will have a similar effect on the interaction between two cells. Therefore, the objective of this chapter is to test the hypothesis that *the presence of multiple cells creates hydrodynamic conditions amenable for cell adhesion.*

6.1 Solution Procedure

The domain of the problem is shown in Figure 6.1. The shear rate is fixed at $Ca = 0.30$, and the area dilation parameter for each cell is fixed at $C = 2.5$. Neither membrane is under prestress, and the viscosity ratio for each cell is set at $\lambda = 1$. Two heights above the wall have been chosen to determine the effect of the wall: $h/a = 2.5$, and $h/a = 1.25$. The height of each cell above the wall is held fixed for each simulation, similar to the method of Uijttewaal *et al.* (1993). Two different scenarios are investigated, with cells either side-by-side ($\Delta x/a = 0$), or in-line with the flow ($\Delta z/a = 0$). The cells are started at different initial positions of $\Delta x_0/a$ and $\Delta z_0/a$, and allowed to deform until equilibrium has been reached. The initial positions chosen for each scenario are

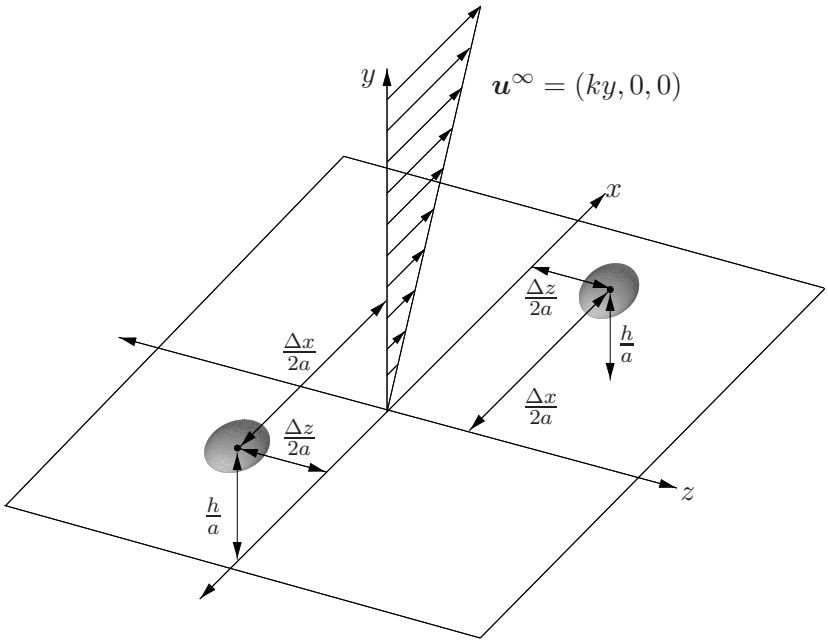

Figure 6.1: Schematic diagram of two cells suspended in linear shear flow above a plane wall. One cell is located at $(\Delta x/2a, h/a, \Delta z/2a)$, and the other at $(-\Delta x/2a, h/a, -\Delta z/2a)$. The cells are positioned either side-by-side $(\Delta x/a = 0)$, or in-line with the flow $(\Delta z/a = 0)$.

$\Delta x_0/a = 1, 2, 3, 4, 5, 7.5, 10, 20,$ and $\Delta z_0/a = 0.5, 1, 2, 3, 4, 5, 7.5, 10.$

6.2 Side-by-Side Cells

6.2.1 Cell Deformation

The reduced volume of a cell as a function of separation distance for two cell heights $h/a = 1.25$ and 2.5 is shown in Figure 6.2. Very little variation from the deformation of a single cell can be observed as the cells move closer together. At small separation distances $\Delta z/a \lesssim 5$, the reduced volume of cells at $h/a = 1.25$ increases slightly, indicating that the presence of a cell in close proximity causes marginally less deformation than a cell in isolation. The highest increase in reduced volume observed in comparison to an isolated cell is $\sim 0.6\%$.

6.2.2 Cell Velocity

The slip velocity of the cells at two different cell heights $h/a = 1.25$ and 2.5 is shown in Figure 6.3. Because the orientation of the cells is symmetric with respect to the flow plane the velocities of the cells are identical in the x and y directions. It is clear that the slip velocity of each cell is greater than that of a single cell for both cell heights

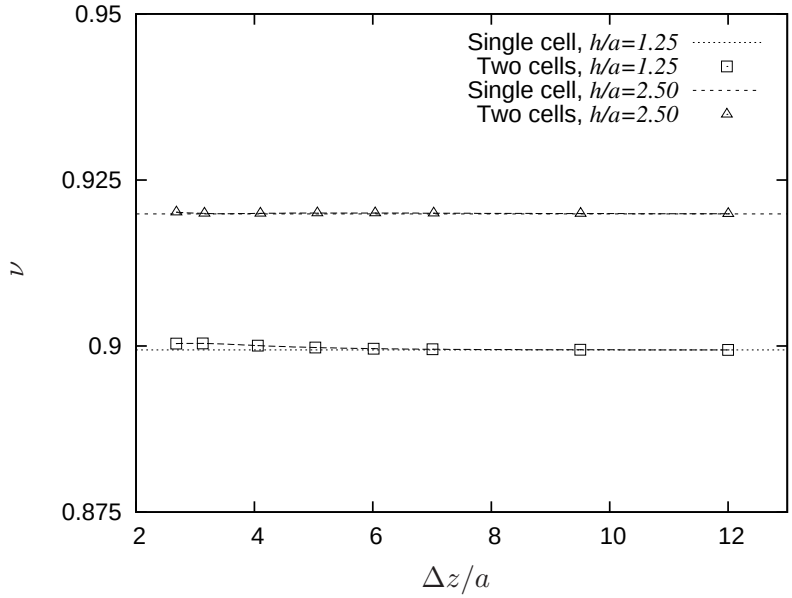

Figure 6.2: Reduced volume ν of cells as a function of separation distance $\Delta z/a$ at two different cell heights $h/a = 1.25$ and 2.5.

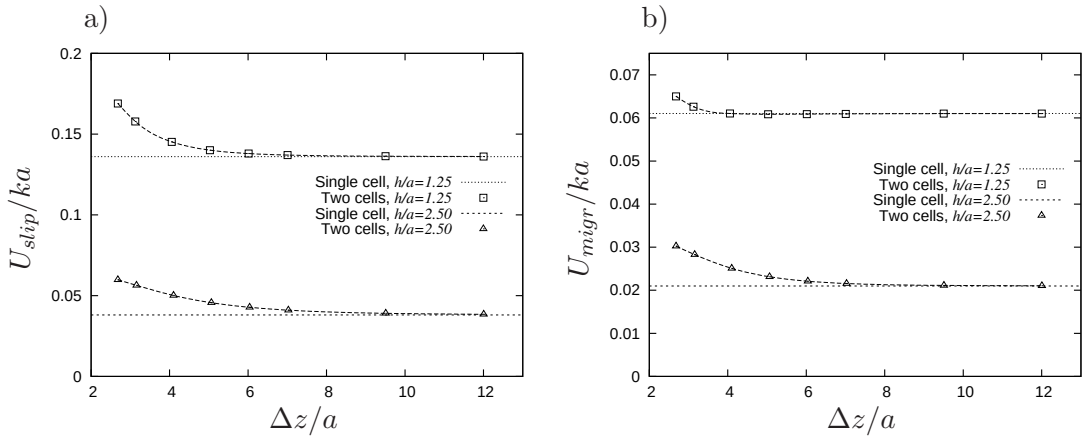

Figure 6.3: Velocity of cells separated by distance $\Delta z/a$ at two different cell heights $h/a = 1.25$ and 2.5, showing a) the slip velocity of the cells U_{slip}/ka and b) the migration velocity of the cells U_{migr}/ka.

examined. As the separation distance lessens, the slip velocity of each cell increases. At the cell height of $h/a = 1.25$, the slip velocity and the rate of increase for each cell are higher than they are for the higher cell height of $h/a = 2.5$. The separation distance at which the cells begin to have an influence on each other decreases as the cells move closer to the wall. For a cell height of $h/a = 2.5$, the slip velocity of the cells is affected for $\Delta z/a \lesssim 9.5$. For a cell height of $h/a = 1.25$, the region of influence decreases to $\Delta z/a \lesssim 7$.

The presence of multiple cells also has an effect on the migration velocity of the cells. For both heights considered the migration velocity increases above that of a single cell,

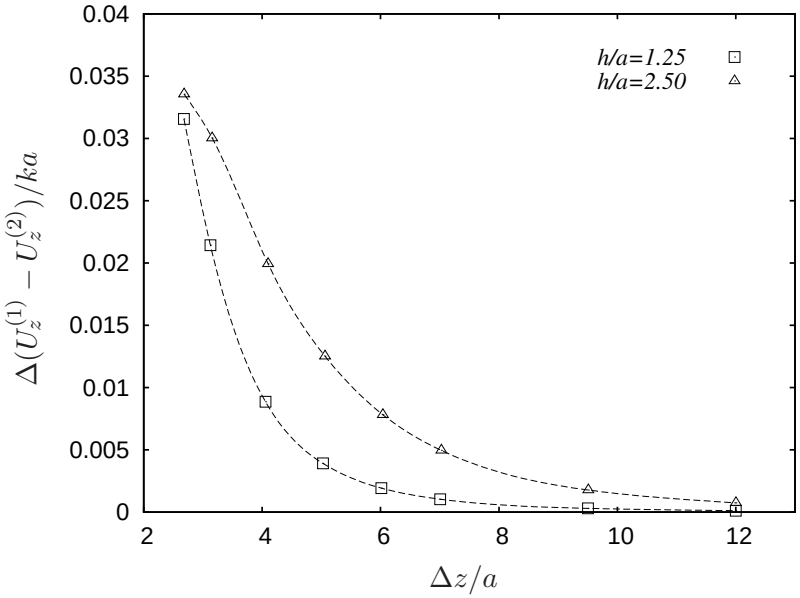

Figure 6.4: Difference in velocity of the cells in the z direction $\Delta(U_z^{(1)} - U_z^{(2)})/ka$ as a function of separation distance $\Delta z/a$ for two cell heights $h/a = 1.25$, and 2.5. The superscript $^{(1)}$ refers to the cell located at $(0, h/a, \Delta z/2a)$ while the superscript $^{(2)}$ refers to the cell located at $(0, h/a, -\Delta z/2a)$.

and the migration velocity increases as the separation distance lessens. The migration velocity appears to be less sensitive to the presence of another cell than the slip velocity, with negligible effect beyond $\Delta z/a \gtrsim 7$ for cell height $h/a = 2.5$, and $\Delta z/a \gtrsim 4$ for cell height $h/a = 1.25$.

The difference in the velocity of the cells in the z direction is shown in Figure 6.4. Due to the symmetry of the cell positions with respect to the flow, the velocity in the z direction of one cell is equal and opposite to the velocity of the other. It is apparent that the cells move away from one another, and that the magnitude of the velocity increases as the separation distance decreases. The velocity of the cells in the z direction decreases as the cell height decreases.

6.2.3 Cell Shear Stress

Figure 6.5 depicts the effect of cell separation distance on the average principal shear stress on the surface of the cell. It is clear that the separation distance has a negligible effect on the surface shear stress. At a cell height of $h/a = 2.5$, there is a slight increase of approximately 0.2% in surface shear stress in the range $2.5 \lesssim \Delta z/a \lesssim 5$. For a cell height of $h/a = 1.25$, the surface shear stress decreases by approximately 0.6% in the range of $2.5 \lesssim \Delta z/a \lesssim 7$. The marginal decrease in cell shear stress can be explained

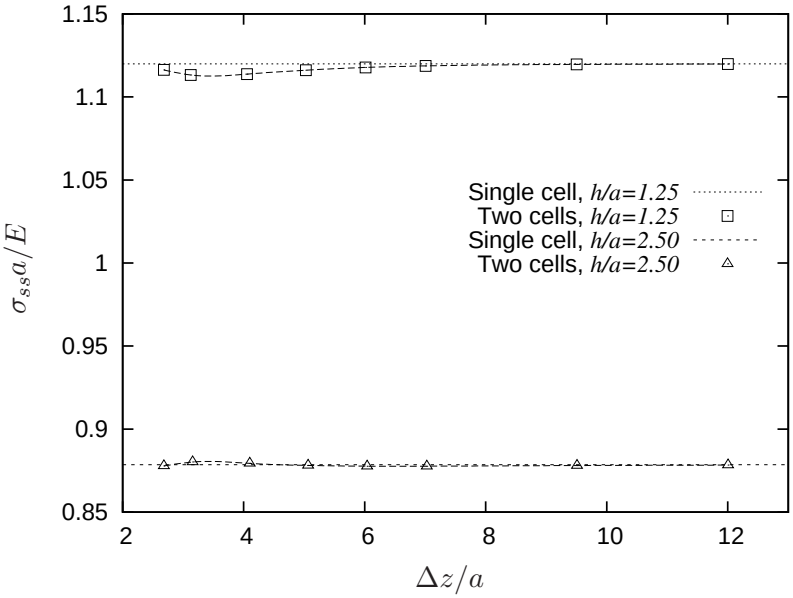

Figure 6.5: Average principal shear stress on the cell surface $\sigma_{ss}a/E$ as a function of cell separation distance $\Delta z/a$ for two cell heights $h/a = 1.25$ and 2.5.

by the corresponding increase in reduced volume of the cells (Figure 6.2).

6.2.4 Wall Shear Stress

Figure 6.6 illustrates the effect of separation distance on the principal shear stress present on the wall. The principal shear stress contours are shown at three separation distances $\Delta z/a$, with the regions of principal shear stress 5% above ambient levels indicated with solid black lines. Also shown are the regions of shear stress that fall below or exceed the shear stress range for an isolated cell. It is apparent that the main effect of two cells side-by-side on the wall shear stress is the presence of a low shear stress region between the two cells at close separation distances. At the closest separation distance of $\Delta z/a = 2.68$, there are two small regions of stress that exceed the maximum wall shear stress for an isolated cell by $\sim 4\%$. At larger cell separation distances the wall shear stress levels correspond to the wall shear stress contours of a single cell.

6.3 In-Line Cells

6.3.1 Cell Deformation

When the configuration is changed from two cells side-by-side to two cells in-line with one another, the symmetry with the respect to the flow plane is broken. Therefore

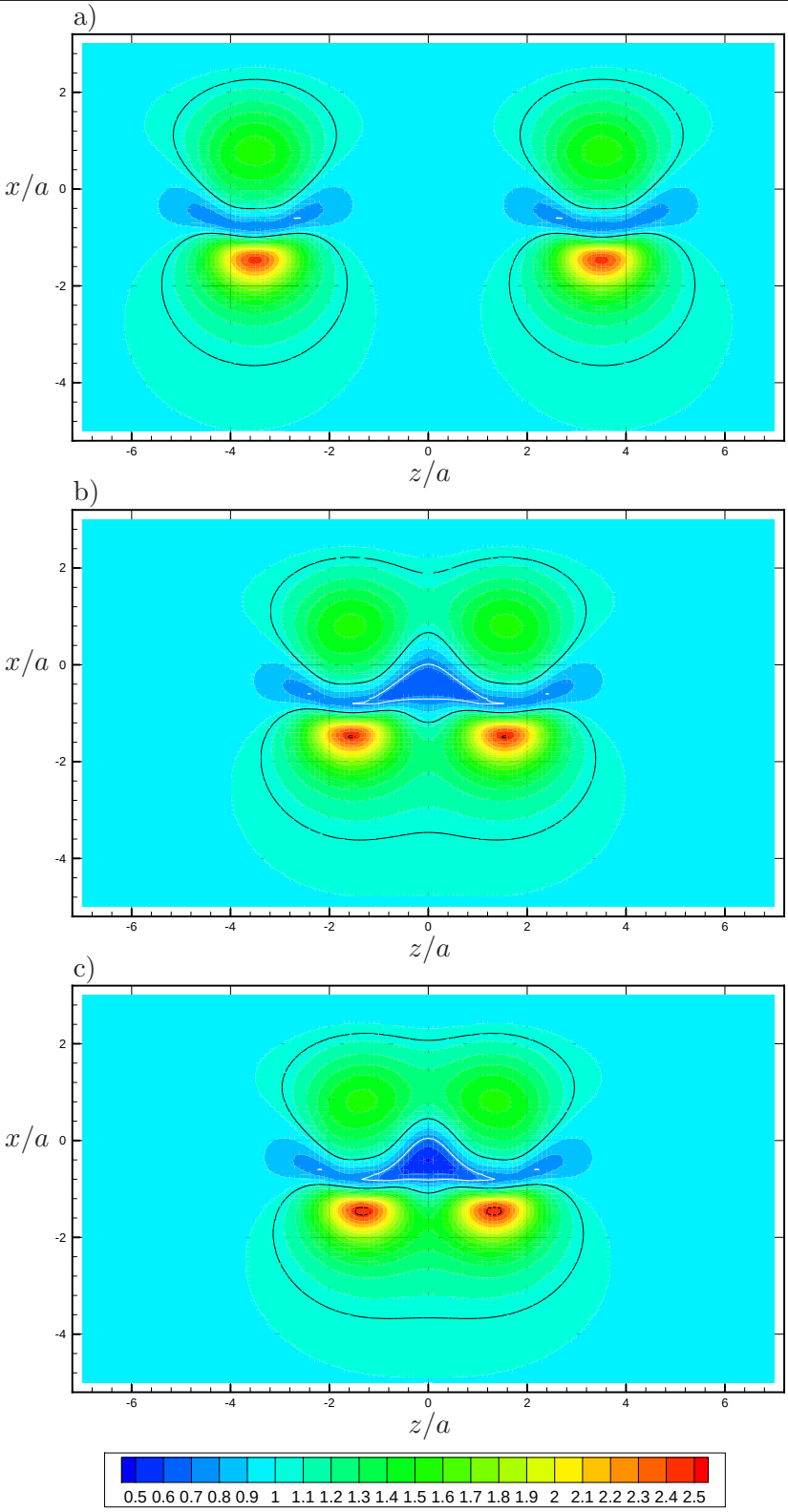

Figure 6.6: Principal wall shear stress contours $\sigma_{ss}a/E$ for various separation distances $\Delta z/a$. The separation distances shown are a) $\Delta z/a = 7.00$, b) $\Delta z/a = 3.13$, and c) $\Delta z/a = 2.68$. The solid black line indicates the region of the wall where the principal shear stress is 5% or more above ambient levels. The solid white line indicates the region of the wall where the principal shear stress falls below the minimum wall shear stress for an isolated cell. The dashed black line indicates the region of the wall where the principal shear stress exceeds the maximum wall shear stress for an isolated cell. Flow is from bottom to top.

each cell will behave differently at close separation distances $\Delta x/a$. The cell shapes at various separation distances $\Delta x/a$ are shown in Figure 6.7 for cell height $h/a = 1.25$. For large separation distances the cell shapes are indistinguishable from the shape of a single cell at the same height. However at small separation distances the upstream and downstream cell shapes differ. For the closest separation distance of $\Delta x/a = 2.65$, the membrane of each cell flattens in the region closest to the other cell. This is similar to the observations of Lac *et al.* (2007), who observed high external pressures in the gap between two crossing capsules in unbounded shear flow. The high pressure region causes a flattening of the membrane.

The reduced volume of both cells as a function of separation distance is shown in Figure 6.8. It is evident that the reduced volume of each cell increases significantly as the cell separation distance decreases. This effect becomes more significant at the closer cell height of $h/a = 1.25$. At small separation distances, the downstream cell has a lower reduced volume than the upstream cell. This increase in reduced volume means that the cells deform less than an isolated cell, due to the flattening of the membrane.

6.3.2 Cell Velocity

The slip velocities of the cells for two cell heights $h/a = 1.25$ and $h/a = 2.5$ are shown in Figure 6.9. It is apparent that the slip velocity of the downstream cell is higher than that of a single cell. The upstream cell, however, experiences a lower slip velocity than the downstream cell. This means that the cells will eventually come into contact, because the downstream cell moves slower relative to the upstream cell. As the separation distance decreases, the slip velocity of the upstream cell decreases rapidly, and the slip velocity of the downstream cell increases rapidly. The difference between the upstream and downstream cell slip velocities is depicted in Figure 6.10. The difference in velocity is positive over a large range before becoming negligible at very large separation distances $\Delta x/a \gtrsim 15$. At the cell height of $h/a = 2.5$, the slip velocity difference is greater than the lower cell height for intermediate separation distances of $\Delta x/a \gtrsim 4.5$. At closer separation distances, the cells at height $h/a = 1.25$ experience a greater difference in slip velocity.

The migration velocity of the cells is also affected by cell separation distance and cell height. For cell height $h/a = 2.5$, the migration velocity of the upstream cell is less than the migration velocity of a single cell at the same height. At intermediate wall

Figure 6.7: View of cells in the xy plane at different separation distances $\Delta x/a$. The separation distances shown are a) $\Delta x/a = 9.49$, b) $\Delta x/a = 6.96$, c) $\Delta x/a = 4.87$, d) $\Delta x/a = 3.76$, and e) $\Delta x/a = 2.65$. Flow is from left to right.

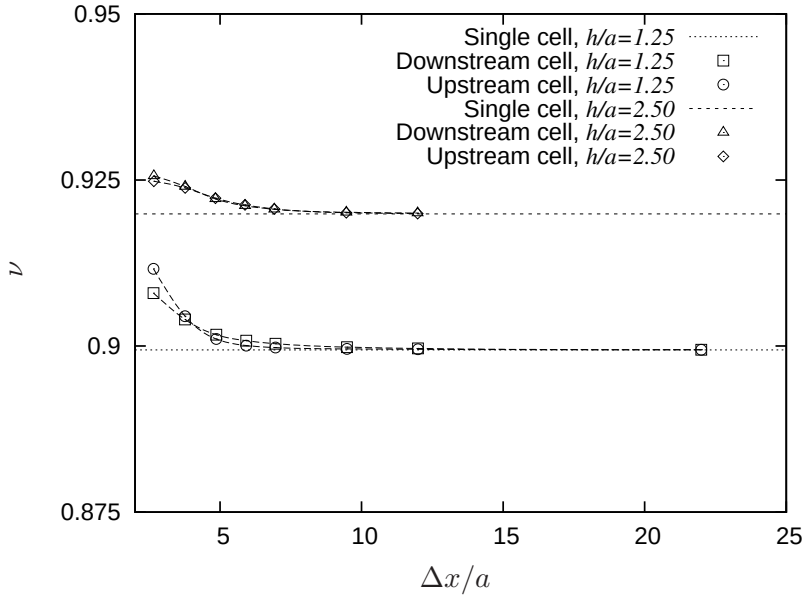

Figure 6.8: Reduced volume of cells ν as a function of separation distance $\Delta x/a$ at two different cell heights $h/a = 1.25$ and 2.5.

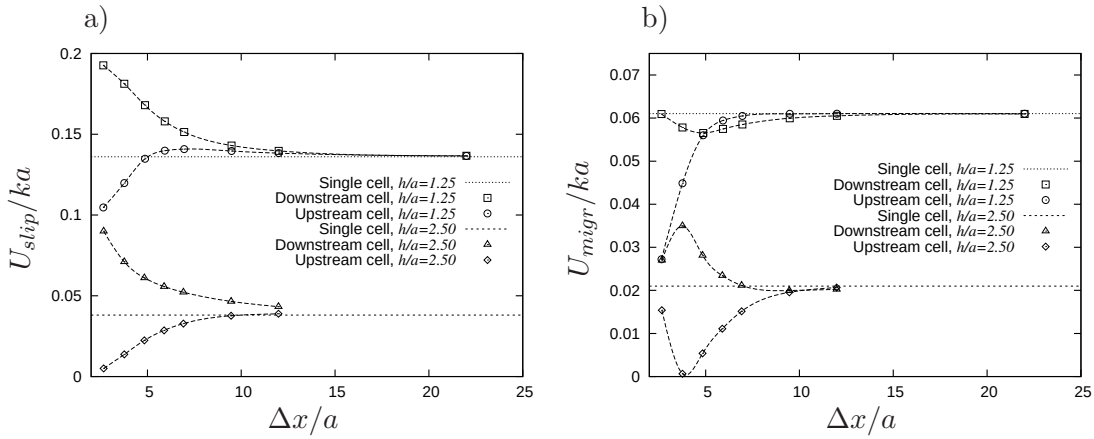

Figure 6.9: Velocity of upstream and downstream cells separated by distance $\Delta x/a$ at two different cell heights $h/a = 1.25$ and 2.5. Shown are a) the slip velocity of the cells U_{slip}/ka, and b) the migration velocity of the cells U_{migr}/ka.

heights, the migration velocity of the downstream cell falls slightly below the single cell migration velocity. For separation distances $\Delta x/a \lesssim 7$, the migration velocity of the downstream cell is greater than the migration velocity of the single cell. The rate-of-change of the migration velocity for both cells changes sign at $\Delta x/a \sim 4$. At the closer cell height of $h/a = 1.25$, the migration velocity of both cells falls below that of the single cell. The upstream cell migration velocity decreases significantly with decreasing separation distance, whereas the downstream cell migration velocity starts to increase at $\Delta x/a \sim 2$.

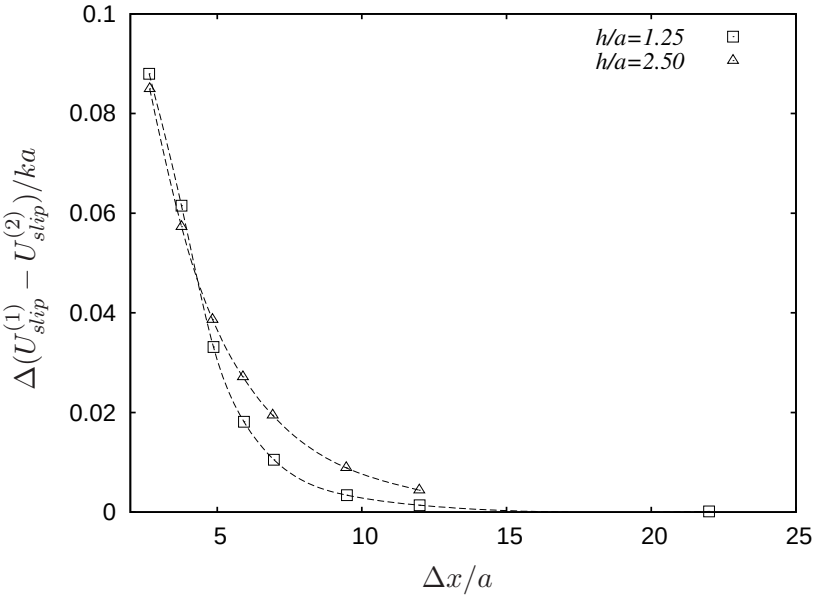

Figure 6.10: Difference in slip velocity of the cells $\Delta(U^{(1)}_{slip} - U^{(2)}_{slip})/ka$ as a function of separation distance $\Delta x/a$ for two cell heights $h/a = 1.25$, and 2.5. The superscript 1 refers to the cell located at $(\Delta x/2a, h/a, 0)$ while the superscript 2 refers to the cell located at $(-\Delta x/2a, h/a, 0)$.

6.3.3 Cell Shear Stress

The effect of separation distance on the average principal shear stress present on the cell membrane is shown in Figure 6.11. As the separation distance decreases, the average cell shear stress decreases markedly, an effect that is more pronounced at the lower cell height of $h/a = 1.25$. The decrease in cell shear stress with decreasing separation distance can be attributed to the corresponding increase in reduced volume caused by the flattening of the cell membrane (Figure 6.8). At close separation distances the upstream cell experiences less average shear stress than the downstream cell at a cell height of $h/a = 1.25$.

6.3.4 Wall Shear Stress

Figure 6.12 depicts the principal wall shear stress contours for various separation distances $\Delta x/a$. The regions of elevated shear stress 5% above ambient levels are marked with solid black lines. At large separation distances of $\Delta x/a \gtrsim 9.5$ the shear stress of the region below each cell is the same as the shear stress distribution of an isolated cell. As the separation distance decreases a region of low shear stress, below the minimum wall shear stress caused by a single cell, develops below the downstream cell. At the closest separation distance of $\Delta x/a = 2.65$, this region of low shear stress disappears.

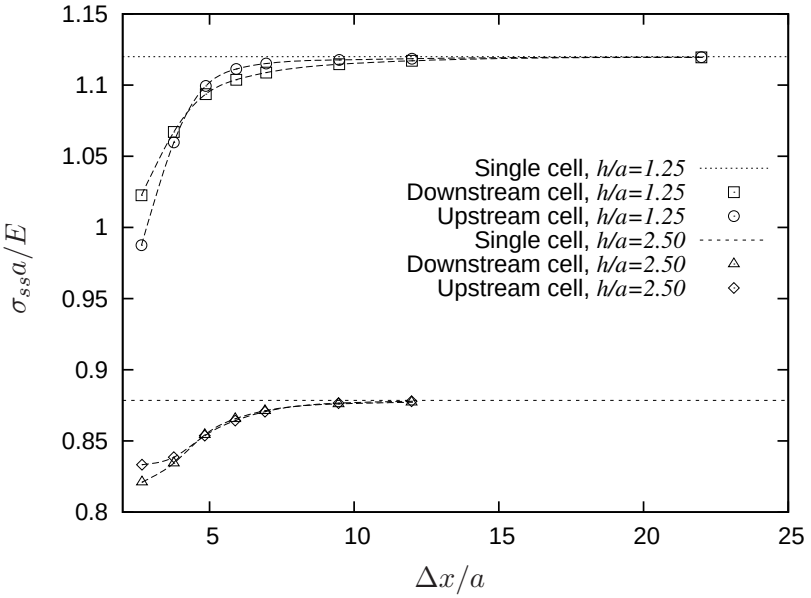

Figure 6.11: Average principal shear stress $\sigma_{ss}a/E$ on the upstream and downstream cell surfaces as a function of cell separation distance $\Delta x/a$ for two cell heights $h/a = 1.25$ and 2.5.

Instead, a region of high shear stress forms immediately behind the downstream cell, and ahead of the upstream cell. It is apparent that the upstream cell experiences a larger region of elevated shear stress ahead of it, due to the presence of the downstream cell. The region of lower shear stress immediately below the upstream cell also becomes much smaller as the separation distance decreases.

6.4 Conclusions

Results have been presented in this chapter in order to quantify the effect of cell separation distance on multiple cell dynamics near a wall in linear shear flow. The effect of one cell on another has been examined for a cell next to another cell, and for a cell behind another cell. The effect of cell height and separation distance on the slip and migration velocities of each cell, and the shear stresses present on the cells and the wall have been presented.

Side-by-side cells display very little change in deformation as the separation distance decreases. This negligible change in cell deformation means that the change in average cell shear stress with separation distance is also marginal. The presence of multiple cells also has a limited effect on the wall shear stress. The main effect of the presence of two cells is a region between the two cells of lower shear stress than that observed

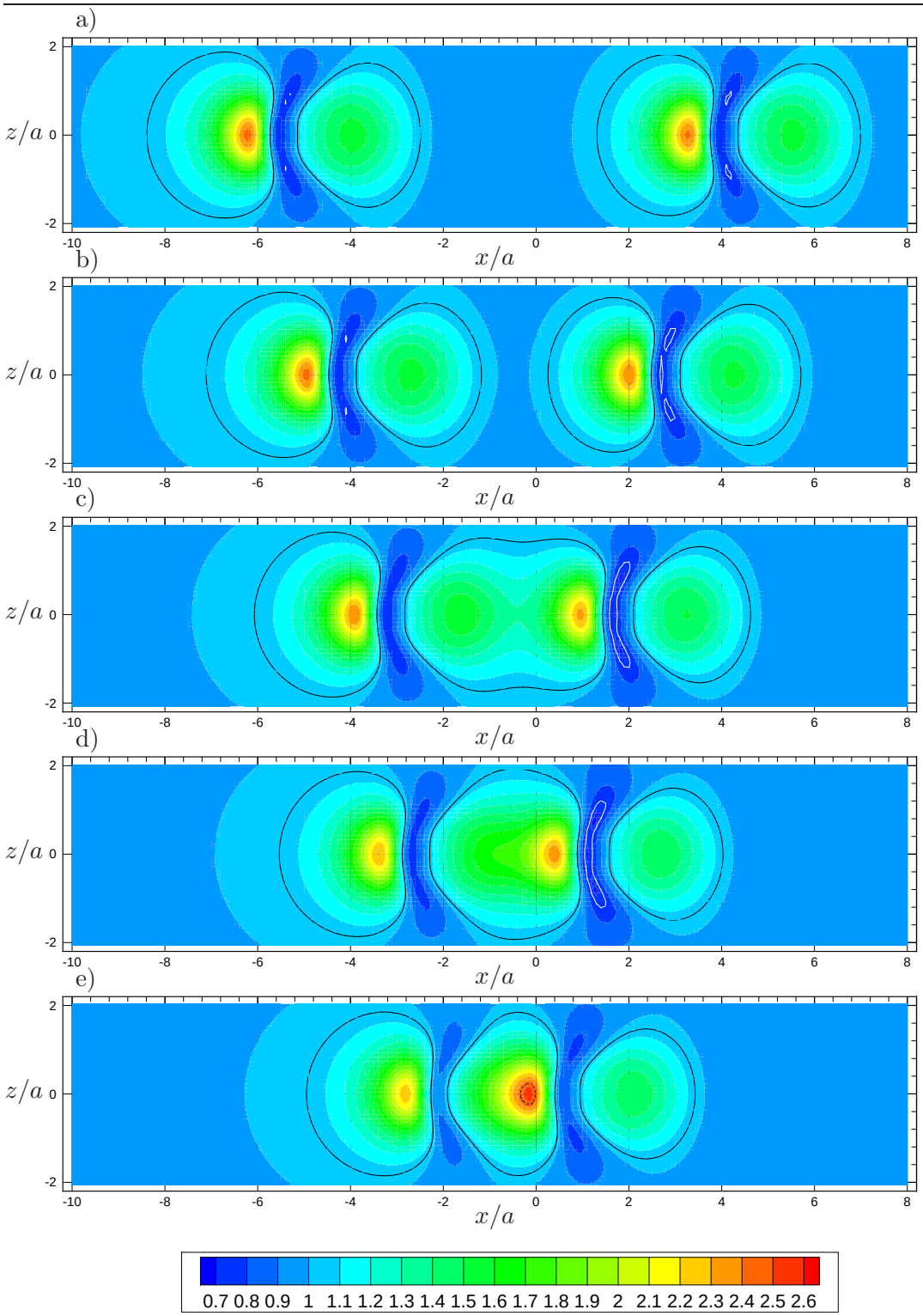

Figure 6.12: Principal wall shear stress contours $\sigma_{ss}a/E$ for various separation distances $\Delta x/a$. The separation distances shown are a) $\Delta x/a = 9.49$, b) $\Delta x/a = 6.96$, c) $\Delta x/a = 4.87$, d) $\Delta x/a = 3.76$, and e) $\Delta x/a = 2.65$. The solid black line indicates the region of the wall where the principal shear stress is 5% or more above ambient levels. The solid white line indicates the region of the wall where the principal shear stress falls below the minimum wall shear stress for an isolated cell. The dashed black line indicates the region of the wall where the principal shear stress exceeds the maximum wall shear stress for an isolated cell. Flow is from left to right.

for a single cell, a condition not ideal for increased activation of receptors on the vessel surface.

In contrast, the velocity of the cells are affected markedly as they move closer together. For both cell heights examined, the slip velocity of the cells was greater than that of a single cell at the same height. At the closest cell height of $h/a = 1.25$, the largest increase in slip velocity was 25% above that of a single cell at the same height. This increase in slip velocity as a result of the presence of another cell is highly beneficial for cell adhesion, as each cell moves slower relative to the receptors present on the vessel surface.

The migration velocity of side-by-side cells also increases above that of a single cell as the separation distance increases. This is disadvantageous to cell adhesion, as the cells spend less time in close proximity to the wall. It is evident however that this effect decreases as the cell height decreases, suggesting that the effect of the presence of multiple cells on the migration velocity is not important when the cells are very near the wall. It is also apparent that two cells side-by-side will not come into contact, because the cells have a tendency to move away from one another. This effect increases with decreasing separation distance. It is also apparent that this effect decreases with decreasing cell height.

The effect of one cell behind another on the deformation of each cell is more marked than for cells side-by-side. At close separation distances the membrane of each cell flattens in the region closest to the other cell. This causes the deformation of each cell to decrease in comparison to the deformation of a single cell at the same height. In turn, this leads to a decrease in average cell shear stress of each cell as the separation distance lessens. The in-line cell configuration also has an effect on the wall shear stress distribution. As the cell separation distance decreases, a region of higher shear stress develops behind the downstream cell, and ahead of the upstream cell.

The in-line cell configuration has a marked effect on the cell velocities. The upstream cell has a lower slip velocity than a single cell at the same cell height. Conversely, the downstream cell has a higher slip velocity, and the cells move toward one another. The migration velocity of the upstream cell is lower than that of the downstream cell for close separation distances. As a consequence, the upstream cell moves towards and below the downstream cell. This may lead to subsequent contact with both the wall and the downstream cell, increasing the probability of adhesion.

The aim of this chapter was to test the hypothesis that *the presence of multiple cells creates hydrodynamic conditions amenable for cell adhesion.* It is clear from the results presented that the hypothesis is too simplistic a statement. It is evident that the presence of multiple cells has both a positive and a negative effect on the hydrodynamic conditions relevant to cell adhesion. The presence of multiple cells has a limited effect on the wall shear stress, although the presence of a cell downstream of another cell provides a larger region of elevated shear stress on the vessel wall. It is also apparent that a cell moving behind another cell will move towards, and below the downstream cell, increasing the probability of cell-cell or cell-wall contact. The presence of another cell in the flow has an adverse effect on the cell surface shear stress, which tends to decrease with decreasing separation distance. Cells moving side-by-side with the flow experience a larger migration velocity, and tend to move further apart. Beneficially, the presence of another cell in the flow means that a cell moves slower relative to the vessel wall than an isolated cell, increasing the probability of bonds forming between the cell and the wall.

CHAPTER 7

CONCLUSIONS

7.1 Summary

This chapter presents a summary of the conclusions of the thesis. The thesis has presented the results of two numerical models developed to model blood cell dynamics near a vessel wall. The aim of the study has been to provide a more physiologically relevant model of a blood cell. Cells such as leukocytes and platelets consist of a complex internal structure immersed in a non-Newtonian cytoplasm. Current models presented in the literature rarely consider the morphological changes that cells undergo during cell adhesion. These morphological changes involve an active reorganisation of the cell cytoskeletion, and consequently the mechanical properties of the cell change significantly. Evidence of this is the observation of long, thin tethers being pulled from the surface of platelets and leukocytes moving across a surface.

In Chapter 4, results have been presented from a model of a two-dimensional tethered cell. Models of cell tethering in the literature do not consider cell deformation. The response of the cell to the flow was observed to be qualitatively similar to the results of the model developed by King *et al.* (2005). As the cell deformed, it was pulled out into the flow, and then pivoted about the tether point and slowly moved toward the wall. The region of cell membrane that would come into contact with the wall was found to correspond to a region of elevated shear stress. The ligands present on the cell membrane may become activated due to this region of elevated shear stress, increasing the chances of adhesion with the wall and subsequent tether formation at the leading edge of the cell, leading to stabilised cell rolling.

The model of a tethered cell was used to test the hypothesis that *the dynamics of a tethered cell are affected by the aspect ratio and the internal viscosity of the cell.* The effect of viscosity was found to be negligible at low shear rates, but at high shear

rates an increase in cell internal viscosity resulted in an increase in cell deformation and tether force. The increase in cell internal viscosity also caused longer, thinner tethers to form. Cells at moderate to high shear rates with lower aspect ratios were found to experience greater tether force and deformation. At low shear rates this was reversed, with higher aspect ratio cells experiencing greater tether force and deformation. Cells with lower aspect ratios were observed to form longer, thinner tethers.

Several different strategies were employed in an attempt to make the tether model more physiologically consistent. For the two-dimensional model, a membrane with locally varying elasticity was trialled in an attempt to pull a long, thin tether from the cell, with little deformation of the body of the cell. Another strategy undertaken involved modelling the cell as a solid body enclosed in a fluid-filled elastic membrane. Both of these attempts proved unsuccessful. The three-dimensional model proved to be too insufficiently resolved for a tether to form, so effort was directed at improving the accuracy of the formulation. An improved method of approximating the unit normal to the surface was implemented following the work of Zinchenko *et al.* (1997), but the formation of a tether was still not possible. Another strategy employed to make the formulation more stable was to implement dynamic adaption of the mesh, which offered more promising results but was too computationally expensive for the resources available.

In Chapter 5, results from a three-dimensional model have been presented. Current models of cells in the literature focus mainly on cells that have already contacted the wall and initiated adhesion. As a consequence, the hydrodynamic effect caused by the presence of a cell has not been quantified. Hence, it was also the aim of this thesis to quantify the effect of cell deformation on the flow properties relevant to cell adhesion. The hypothesis tested with the 3D model was that *an easily deformable cell creates hydrodynamic conditions amenable for cell adhesion.* It was found that a less deformable cell is able to approach the wall more easily due to a higher slip velocity and a smaller migration velocity. Closer to the wall however, it was observed that an easily deformable cell creates hydrodynamic conditions amenable for cell adhesion. An easily deformable cell is stressed to a larger degree, and presents a greater surface to the vessel wall. An easily deformable cell also creates a greater region of elevated wall shear stress upstream, beneficial for the adhesion of other cells present in the flow. It can be concluded that it is easier for a cell to approach the wall in its unactivated state.

Once close to the wall and activation has taken place, the cell is then more likely to initiate adhesion.

Chapter 6 presented data gathered from the 3D model in order to test the hypothesis that *the presence of multiple cells creates hydrodynamic conditions amenable for cell adhesion*. It has been found that the presence of multiple cells has both a positive and a negative effect on the hydrodynamic conditions important to cell adhesion. The wall shear stress distribution is not affected to a significant degree, although the presence of a cell downstream provides a larger region of elevated shear stress on the vessel wall for the upstream cell. The cell surface shear stress was found to decrease with decreasing cell separation distance. Cells moving side-by-side in the flow experience a larger migration velocity, and have a tendency to move away from each other. A cell moving behind another cell will move towards, and below the downstream cell, increasing the probability of cell-cell or cell-wall contact. It was also found that the presence of multiple cells in the flow increases the slip velocity of the cells significantly, heightening the probability of cell adhesion.

Although the original aim of the thesis was not fully met with regard to a more physiologically consistent model of a cell, it is clear that a significant amount of original work has been presented in this thesis. The dynamics of elastic capsules moving near or attached to a wall can be used to shed light on the effect of the hydrodynamic conditions created by a cell on the likelihood of cell adhesion. It is hoped that the models and results presented in this study can form the basis for the development of models directly applicable to physiological scenarios.

7.2 Future Work

There is considerable scope for improvement with regard to the models developed in this thesis. Presented here are a number of possibilities for future work on this topic.

For the three-dimensional model, a simple modification to allow for viscosity ratios other than unity would mean that the effect of the transition from tank-treading to tumbling of the cell on the cell velocity could be determined. A more stable formulation would also enable more detailed studies of single and multiple-cell dynamics. This could be achieved by several different modifications to the code:

- the stability and accuracy of the unstructured-mesh formulation can be improved by developing an accurate method to calculate the traction at each node, rather

than averaging over each element.

- An implementation of a structured mesh formulation would allow the simulation to be more stable for longer periods of time.

Once the stability and accuracy of the model has been improved, other studies can be carried out, such as:

- the effects of pulsatile flow,
- the effect of a vessel wall on cells in very close proximity with regard to potential contact area between the cells.

Other modifications can be implemented to widen the scope of both the 2D and 3D models:

- To improve the physiological relevance of both the 2D and 3D models, a solid body can be placed inside the cell membrane to represent the cell nucleus in the case of a leukocyte, or the microtubule band in the case of a platelet. This would necessitate the development of some sort of coupling between the solid and the membrane to prevent the solid from contacting the membrane. This could take the form of a repulsive force distribution.
- Explicit meshing of external boundaries can be implemented. This would enable studies of cells moving in vessels to be carried out, allowing the effects of thrombii or stenoses on cell dynamics to be elucidated.

APPENDIX A

2D METHOD

A.1 Governing Equations

If inertial effects are considered negligible, then the flow in the exterior and interior of the cell is governed by the Stokes flow equations (Leal 1992)

$$\mu\nabla^2\boldsymbol{u} = \boldsymbol{\nabla}p, \qquad \boldsymbol{\nabla}\cdot\boldsymbol{u} = 0, \tag{A.1}$$

$$\lambda\mu\nabla^2\hat{\boldsymbol{u}} = \boldsymbol{\nabla}\hat{p}, \qquad \boldsymbol{\nabla}\cdot\hat{\boldsymbol{u}} = 0, \tag{A.2}$$

where $\boldsymbol{u}$ and p are the velocity and pressure fields in the exterior domain Ω, $\hat{\boldsymbol{u}}$ and $\hat{p}$ are the velocity and pressure fields in the interior domain V, and λ is the viscosity ratio of the interior to exterior fluid.

The boundary conditions are such that the velocity is continuous across the interface C, and that the normal stress at the interface is balanced by elastic tensions in the membrane. The first condition gives

$$\boldsymbol{u} = \hat{\boldsymbol{u}}, \qquad x \in C. \tag{A.3}$$

The second condition can be written as (Pozrikidis 2001*b*)

$$\Delta\boldsymbol{f} = (\boldsymbol{\sigma} - \hat{\boldsymbol{\sigma}})\cdot\boldsymbol{n} = \gamma\kappa\boldsymbol{n} - \frac{\partial\gamma}{\partial l}\boldsymbol{t}, \tag{A.4}$$

where $\boldsymbol{\sigma}$ is the stress tensor, $\Delta\boldsymbol{f}$ is the stress discontinuity across the interface, $\boldsymbol{n}$ is the unit normal vector to the interface pointing into the exterior fluid, $\boldsymbol{t}$ is the unit tangent vector, l is the arc-length along the interface, κ is the curvature of the interface, and γ is the elastic tension of the membrane.

A.2 Boundary Integral Equation

The boundary integral equation is formed by seeking solutions to the singularly forced Stokes flow equations (Pozrikidis 1992)

$$\mu\nabla^2\boldsymbol{u} = \boldsymbol{\nabla}p - \boldsymbol{g}\,\delta(\boldsymbol{x}-\boldsymbol{x}_0), \qquad \boldsymbol{\nabla}\cdot\boldsymbol{u} = 0 \tag{A.5}$$

where δ is the two-dimensional delta function, $\boldsymbol{x}$ is the observation point, $\boldsymbol{x_0}$ is the source point, and $\boldsymbol{g}$ is an arbitrary constant vector. By introducing the velocity Green's function G_{ij} and the stress Green's function T_{ijk}, the solution to equation A.5 can be written as (Pozrikidis 1992):

$$u_i(\boldsymbol{x}) = \frac{1}{4\pi\mu}G_{ij}(\boldsymbol{x},\boldsymbol{x}_0)g_j \tag{A.6}$$

$$\sigma_{ik}(\boldsymbol{x}) = \frac{1}{4\pi}T_{ijk}(\boldsymbol{x},\boldsymbol{x}_0)g_j \tag{A.7}$$

Physically, equation A.6 and equation A.7 express the flow field produced by a concentrated point force of strength $\boldsymbol{g}$ located at source point $\boldsymbol{x}_0$. The form of the Green's function depends upon whether the fluid is bounded or unbounded. For an unbounded fluid, the Green's functions can be shown to be (Pozrikidis 1992):

$$G_{ij}^{FS}(\boldsymbol{x},\boldsymbol{x}_0) = -\delta_{ij}\ln r + \frac{\hat{x}_i\hat{x}_j}{r^2} \tag{A.8}$$

$$T_{ijk}^{FS}(\boldsymbol{x},\boldsymbol{x}_0) = -4\frac{\hat{x}_i\hat{x}_j\hat{x}_k}{r^4} \tag{A.9}$$

where $\hat{\boldsymbol{x}} = \boldsymbol{x}-\boldsymbol{x}_0$ and $r = |\hat{\boldsymbol{x}}|$.

Other Green's functions have been derived, including for flow in a semi-infinite domain bounded by an infinite plane wall. These are included in Appendix B.

Using equation A.6, equation A.7 and the Lorentz reciprocal relation the boundary integral representation for Stokes flow can be derived (Pozrikidis 1992):

$$u_j(\mathbf{x}_0) = -\frac{1}{2\pi\mu}\int_C G_{ij}(\mathbf{x},\mathbf{x}_0)f_i(\boldsymbol{x})\;dl(\mathbf{x}) + \frac{1}{2\pi}\int_C^{PV} u_i(\mathbf{x})T_{ijk}(\mathbf{x},\mathbf{x}_0)n_k(\mathbf{x})\;dl(\mathbf{x}) \tag{A.10}$$

where the traction $\boldsymbol{f}$ is defined as $\boldsymbol{\sigma}\cdot\boldsymbol{n}$. The first and second integrals on the RHS of equation A.10 are known as the single-layer and double-layer integrals respectively. Depending on the type of boundary conditions specified, equation A.10 can be used to either describe the disturbance velocity caused by a body of any shape that exerts a nonzero force in a fluid or to describe the hydrodynamic force acting on an arbitrarily

shaped body. Specifying the boundary distribution of the velocity $\boldsymbol{u}$ reduces equation A.10 to a Fredholm equation of the first kind for the traction $\boldsymbol{f}$. Specifying the boundary distribution of the traction $\boldsymbol{f}$ yields a Fredholm equation of the second kind for the velocity $\boldsymbol{u}$.

When considering linear shear flow past a deformable interface, equation A.10 can be used to derive the integral (Pozrikidis 1992):

$$\begin{aligned} u_j(\mathbf{x}_0) = \frac{2}{1+\lambda} u_j^{\infty}(\mathbf{x}_0) - \frac{1}{2\pi\mu_1(1+\lambda)} \int_C \Delta f_i(\mathbf{x}) G_{ij}(\mathbf{x},\mathbf{x}_0)\, dl(\mathbf{x}) \\ + \frac{1-\lambda}{2\pi(1+\lambda)} \int_C^{PV} u_i(\mathbf{x}) T_{ijk}(\mathbf{x},\mathbf{x}_0) n_k(\mathbf{x})\, dl(\mathbf{x}) \end{aligned} \tag{A.11}$$

where μ_1 is the external fluid viscosity, μ_2 is the internal fluid viscosity, and λ is the viscosity ratio μ_2/μ_1.

The type of interface is determined by the specification of the force balance at the surface, denoted by $\Delta f_i(\mathbf{x})$ in equation A.11. The derivation and calculation of the force balance is discussed in detail in section A.5.

Non-dimensionalising equation A.11 with length scale L, velocity scale kL, and stress scale E/L, leads to

$$\begin{aligned} u_j^*(\mathbf{x}_0^*) = \frac{2}{1+\lambda} u_j^{\infty *}(\mathbf{x}_0^*) - \frac{1}{2\pi(1+\lambda)Ca} \int_C \Delta f_i^*(\mathbf{x}^*) G_{ij}^*(\mathbf{x}^*,\mathbf{x_0}^*) dl^*(\mathbf{x}^*) \\ + \frac{1-\lambda}{2\pi(1+\lambda)} \int_C^{PV} u_i^*(\mathbf{x}^*) T_{ijk}^*(\mathbf{x},\mathbf{x_0}^*) n_k^*(\mathbf{x}^*) dl^*(\mathbf{x}^*) \end{aligned} \tag{A.12}$$

where Ca is the capillary number, and E is the elastic shear modulus of the membrane. The superscript * denotes a dimensionless quantity. From hereafter non-dimensionality will apply to all quantities, and the superscript will not be used.

The evolution of the cell interface is governed by the elastic capillary number Ca, representing the ratio of viscous forces to elastic forces, and the viscosity ratio λ. The Capillary number Ca can be considered as the dimensionless shear rate, and is defined as:

$$Ca = \frac{\mu k L}{E}. \tag{A.13}$$

A.3 Contour Discretisation

The initial cell interface C is described by a set of N_P marker points, and the shape of the interface is approximated by cubic spline interpolation with respect to a monotonic parameter s. A suitable choice for the monotonic parameter is

$$s_k = k, \tag{A.14}$$

where s_k is the value of s at the kth node.

The kth element is located between the kth and the $k+1$ node, and is described in parametric form by the cubic polynomials

$$x(s) = P_k(s) = a_k(s-s_k)^3 + b_k(s-s_k)^2 + c_k(s-s_k) + d_k, \tag{A.15}$$

$$y(s) = \hat{P}_k(s) = \hat{a}_k(s-s_k)^3 + \hat{b}_k(s-s_k)^2 + \hat{c}_k(s-s_k) + \hat{d}_k, \tag{A.16}$$

where $s_k \leq s \leq s_{k+1}$, and $a_k, b_k, c_k, d_k, \hat{a}_k, \hat{b}_k, \hat{c}_k$ and $\hat{d}_k$ are the coefficients of the polynomials P_k and $\hat{P}_k$.

To find the unknown coefficients a_k, b_k, c_k and d_k, smoothness and interpolation conditions can be used. The polynomials must satisfy the interpolation conditions

$$P(s_k) = x_k \quad \text{for } k = 1, ..., N_E + 1 \tag{A.17}$$

$$P_k(s_{k+1}) = P_{k+1}(s_{k+1}) \quad \text{for } k = 1, ..., N_E - 1. \tag{A.18}$$

At the interior nodes the first and second derivatives must be continuous, yielding

$$P'_k(s_{k+1}) = P'_{k+1}(s_{k+1}) \quad \text{for } k = 1, ..., N_E - 1 \tag{A.19}$$

$$P''_k(s_{k+1}) = P''_{k+1}(s_{k+1}) \quad \text{for } k = 1, ..., N_E - 1 \tag{A.20}$$

This gives $4N_E - 2$ conditions to solve for the $4N_E$ unknown coefficients a_k, b_k, c_k and d_k. Hence, two extra constraints are required at the end-points in order to calculate the unknown coefficients. The end-point constraints are discussed in subsection A.3.1.

It can be shown that the the conditions of smoothness and interpolation lead to an equation involving only the second derivatives $P''_k(s)$ of the form (Mathews & Fink 1999)

$$(x_k - x_{k-1})P''_{k-1} + 2(x_{k+1} - x_{k-1})P''_k + (x_{k+1} - x_k)P''_{k+1} = 6\left[\frac{x_{k+1} - x_k}{s_{k+1} - s_k} - \frac{x_k - x_{k-1}}{s_k - s_{k-1}}\right] \tag{A.21}$$

for $k = 2, ..., N_E$. This gives a linear system of $N_E - 1$ equations for the $N_E + 1$ unknowns P''_{k+1}. With an appropriate choice of end-point constraints the system can be solved using regular matrix methods, or with the computationally efficient Thomas' algorithm (Pozrikidis 2002).

Once the second derivatives have been determined from equation A.21, the coeffi-

cients a_k, b_k, c_k and d_k follow as

$$a_k = \frac{P''_{k+1} - P''_k}{6(s_{k+1} - s_k)}, \tag{A.22}$$

$$b_k = \frac{P''_k}{2}, \tag{A.23}$$

$$c_k = \frac{x_{k+1} - x_k}{s_{k+1} - s_k} - \frac{(s_{k+1} - s_k)(2P''_k + P''_{k+1})}{6}, \tag{A.24}$$

$$d_k = y_k. \tag{A.25}$$

The $4N_E$ unknown coefficients $\hat{a}_k, \hat{b}_k, \hat{c}_k$ and $\hat{d}_k$ can be found in exactly the same fashion.

The unit normal vector components can now be found using

$$n_1(s) = -\frac{dy}{dl} = -\frac{1}{h_k(s)}\left(3\hat{a_k}(s - s_k)^2 + 2\hat{b_k}(s - s_k) + \hat{c_k}\right), \tag{A.26}$$

$$n_2(s) = \frac{dx}{dl} = \frac{1}{h_k(s)}\left(3a_k(s - s_k)^2 + 2b_k(s - s_k) + c_k\right), \tag{A.27}$$

where the metric coefficient $h_k(s)$ is defined as

$$h_k(s) = \Big[\left(3a_k(s - s_k)^2 + 2b_k(s - s_k) + c_k\right)^2 + \left(3\hat{a_k}(s - s_k)^2 + 2\hat{b_k}(s - s_k) + \hat{c}_k\right)^2\Big]^{1/2}. \tag{A.28}$$

The unit tangent vector to the cell contour follows as

$$t_1(s) = -n_2(s) \tag{A.29}$$

$$t_2(s) = n_1(s) \tag{A.30}$$

A.3.1 End-Point Constraints

Natural Spline

When the cell contour is tethered to the wall, it is reasonable to expect that the curvature will be zero at the end-points. Thus, the two conditions necessary to solve equation A.21 are

$$P''_1(s_1) = 0 \tag{A.31}$$

$$P''_{N_E}(s_{N_E+1}) = 0 \tag{A.32}$$

Periodic Spline

When the cell is not tethered to the wall, the end-point constraints are such that the first and second derivatives of the cubic spline polynomials are continuous across the

entire cell contour. This gives the two conditions necessary to solve equation A.21 as

$$P_1'(s_1) = P_{N_E}'(s_{N_E+1}) \tag{A.33}$$

$$P_1''(s_1) = P_{N_E}''(s_{N_E+1}) \tag{A.34}$$

A.4 Discretisation of Boundary Integral Equation

Discretising equation A.12 yields:

$$\begin{aligned} u_j(\mathbf{x}_0) = \frac{2}{1+\lambda} u_j^{\infty}(\mathbf{x}_0) - \frac{1}{2\pi(1+\lambda)Ca} \sum_{m=1}^{N_E} \int_{E_m} \Delta f_i(\mathbf{x}) G_{ij}(\mathbf{x}, \mathbf{x}_0) dl(\mathbf{x}) \\ + \frac{1-\lambda}{2\pi(1+\lambda)} \sum_{m=1}^{N_E} \int_{E_m}^{PV} u_i(\mathbf{x}) T_{ijk}(\mathbf{x}, \mathbf{x}_0) n_k(\mathbf{x}) dl(\mathbf{x}) \end{aligned} \tag{A.35}$$

Equation A.35 can be solved to yield the velocity of each marker point, once the traction discontinuity $\Delta \boldsymbol{f}$ and the integrals over each element have been computed. The definition and calculation of the traction discontinuity follow in section A.5. The singularities that occur when $\boldsymbol{x}$ and $\boldsymbol{x}_0$ are equal need to be dealt with in both the single and double layer integrals. The methods for dealing with both regular and singular integrals are outlined in section A.6.

A.5 Elastic Tension

A.5.1 Definition

The traction discontinuity can be calculated from Equation A.4 once the membrane tension γ is known. The membrane tension γ can be determined from the deformation of the cell interface using a constitutive equation. For small deformations, the membrane tension can be written as (Breyiannis & Pozrikidis 2000)

$$\gamma = E(\omega - 1), \tag{A.36}$$

where E is the shear elastic modulus, and ω is the stretch ratio defined as

$$\omega = \frac{\partial l(t)}{\partial l_0}, \tag{A.37}$$

where $l(t)$ is the arc-length of the interface at time t, and l_0 is the arc-length of the interface in its undeformed state.

A.5.2 Calculation

The elastic stress in the membrane can be calculated by fitting a cubic spline to the arc-length of the contour, using the arc-length of the reference shape as the monotonic parameter. The stretch ratio ω is then calculated using

$$\omega(l_0) = \frac{\partial l}{\partial l_0} = 3a_l(l_0 - l_{0,k})^2 + 2b_l(l_0 - l_{0,k}) + c_l. \tag{A.38}$$

The result of equation A.38 can then be used in equation A.36 to give the membrane tension γ.

The membrane tension γ at each node is then fitted with a cubic spline, using the arc-length l as the monotonic parameter. The last term of equation A.4 can then be calculated using

$$\frac{\partial \gamma}{\partial l} = 3a_\gamma(l - l_k)^2 + 2b_\gamma(l - l_k) + c_\gamma. \tag{A.39}$$

A.6 Integration

A.6.1 Non-Singular Integrals

When the source point $\boldsymbol{x_0}$ does not lie on the element E_m, the integrals are non-singular and can be calculated using Gauss-Legendre quadrature (Pozrikidis 2002)

$$\begin{aligned}\int_{E_m} f(\boldsymbol{x})\ \mathrm{d}l(\boldsymbol{x}) &= \int_{s_k}^{s_{k+1}} f(\boldsymbol{x}(s))h_k(s)\ \mathrm{d}s \\ &= \frac{s_{k+1} - s_k}{2}\int_{-1}^{1} f(\boldsymbol{x}(\xi))h_k(\xi)d\xi = \frac{s_{k+1} - s_k}{2}\sum_{m=1}^{N_Q} f[\boldsymbol{x}(\xi_m)]h_k(\xi_m)w_m,\end{aligned} \tag{A.40}$$

where $f(\boldsymbol{x})$ is the function being integrated, N_Q is the number of quadrature base points, and w_m is the integration weight corresponding to the mth base point. The parameter ξ is defined as

$$s = \frac{1}{2}(s_k + s_{k+1}) + \frac{1}{2}(s_{k+1} - s_k)\xi, \tag{A.41}$$

A.6.2 Singular Integrals

Single-Layer Integral

When the source point $\boldsymbol{x_0}$ lies on the element E_m, the integrand G_{ij} exhibits a singularity of $O(\ln r)$. The singularity prevents the accurate use of Gauss-Legendre quadrature. To isolate the singularity, the integral over an element can be written as

$$\int_{E_m} G_{ij}(\boldsymbol{x}, \boldsymbol{x}_0)\ \mathrm{d}l(\boldsymbol{x}) = \int_{E_m} (G_{ij}(\boldsymbol{x}, \boldsymbol{x}_0) + \delta_{ij}\ln r)\ \mathrm{d}l(\boldsymbol{x}) - \int_{E_m} \delta_{ij}\ln r\ \mathrm{d}l(\boldsymbol{x}), \tag{A.42}$$

where the logarithmic singularity has been removed from the first integral on the RHS of equation A.42. This integral can now be calculated with Gauss-Legendre quadrature. The second integral on the RHS of equation A.42 can be dealt with by writing it as the sum of two integrals

$$-\int_{E_m} \delta_{ij} \ln r \; \mathrm{d}l(\boldsymbol{x}) = -\int_{s_k}^{s_{k+1}} \delta_{ij} \ln \frac{r}{|s-s_0|} h_k(s)\, ds - \int_{s_k}^{s_{k+1}} \delta_{ij} \ln |s-s_0|\, h_k(s)\, ds, \tag{A.43}$$

where s_0 is the position of the source point. The first integral on the RHS of equation A.43 is non-singular, and can be computed using Gauss-Legendre quadrature. The second integral on the RHS of equation A.43 can also be written as the sum of two integrals

$$\begin{aligned} &-\int_{s_k}^{s_{k+1}} \delta_{ij} \ln |s-s_0|\, h_k(s)\, ds \\ &\qquad = -\int_{s_k}^{s_0} \delta_{ij} \ln |s-s_0|\, h_k(s)\, ds - \int_{s_0}^{s_{k+1}} \delta_{ij} \ln |s-s_0|\, h_k(s)\, ds. \end{aligned} \tag{A.44}$$

Choosing auxilliary dummy variables of $\eta = s_0 - s$ and $\hat{\eta} = s - s_0$, equation A.44 can be rewritten as

$$\begin{aligned} &-\int_{s_k}^{s_0} \delta_{ij} \ln |s-s_0|\, h_k(s)\, ds - \int_{s_0}^{s_{k+1}} \delta_{ij} \ln |s-s_0|\, h_k(s)\, ds \\ &\qquad = -\int_0^{s_0-s_k} \delta_{ij} \ln(\eta) h_k(s_0-\eta)\, d\eta - \int_0^{s_{k+1}-s_0} \delta_{ij} \ln(\hat{\eta}) h_k(s_0+\hat{\eta})\, d\hat{\eta} \end{aligned} \tag{A.45}$$

Both the integrals on the RHS of equation A.45 can be dealt with in the same manner. Considering only the first integral on the RHS of equation A.45, it can be written as

$$\begin{aligned} &-\int_0^{s_0-s_k} \delta_{ij} \ln(\eta) h_k(s_0-\eta)\, d\eta \\ &\qquad = -(s_0-s_k) \int_0^1 \delta_{ij} \ln[\xi(s_0-s_k)] h_k[s_0-\xi(s_0-s_k)]\, d\xi \\ &\qquad = -(s_0-s_k) \int_0^1 \delta_{ij} \ln(\xi) h_k[s_0-\xi(s_0-s_k)]\, d\xi \\ &\qquad - (s_0-s_k) \ln(s_0-s_i) \int_0^1 h_k \delta_{ij}[s_0-\xi(s_0-s_k)]\, d\xi \end{aligned} \tag{A.46}$$

The second integral in the last expression can be computed using Gauss-Legendre quadrature. The first integral can be computed using a quadrature formulated to deal with logarithmic singularities. This allows the integral to be computed using

$$\int_0^1 \delta_{ij} \ln(\xi) h_k[s_0-\xi(s_0-s_i)]\, d\xi = \sum_{m=1}^{N_Q} \delta_{ij} h_m[s_0-\xi(s_0-s_m)] w_m \tag{A.47}$$

The values of ξ_m and w_m are available in Pozrikidis (2002).

Double-Layer Integral

The integrand of the 2D double-layer integral is non-singular and can be computed using Gauss-Legendre quadrature.

A.7 Matrix Inversion

If the viscosity ratio is not equal to one, the velocities of the marker points cannot be found explicitly. As a consequence a linear set of $2N_P$ equations need to be solved. The LAPACK routine *dgesv* can be used to solve the linear set of equations using LU decomposition to yield the velocities of the marker points.

A.8 Time-stepping

Once the velocities of the particle have been found via the solution of the boundary-integral equations, a time-stepping routine needs to be employed to determine the new position and shape of the cell membrane. The differential equation to be solved to determine the new position of the membrane is given by

$$\frac{d\boldsymbol{x}_i}{dt} = \boldsymbol{u}_i \tag{A.48}$$

To solve equation A.48, the Runge-Kutta-Fehlberg (RKF45) method is used (Mathews & Fink 1999). In the RKF45 method, Equation A.48 is solved using a 4th order Runge-Kutta method. Based on the local truncation error, the time step for the next integration is adjusted to ensure optimal time step size. An approximation of the local truncation error is obtained by comparing the solution given by the 4th order Runge-Kutta method to that given by a 5th order Runge-Kutta method. Each time step requires six velocity evaluations, given by

$$\begin{aligned}
k_1 =& u\left(t^{(n)}, x^{(n)}\right)\Delta t,\\
k_2 =& u\left(t^{(n)} + \frac{1}{4}\Delta t, x^{(n)} + \frac{1}{4}k_1\right)\Delta t,\\
k_3 =& u\left(t^{(n)} + \frac{3}{8}\Delta t, x^{(n)} + \frac{3}{32}k_1 + \frac{9}{32}k_2\right)\Delta t,\\
k_4 =& u\left(t^{(n)} + \frac{12}{13}\Delta t, x^{(n)} + \frac{1932}{2197}k_1 - \frac{7200}{2197}k_2 + \frac{7296}{2197}k_3\right)\Delta t,\\
k_5 =& u\left(t^{(n)} + \Delta t, x^{(n)} + \frac{439}{216}k_1 - 8k_2 + \frac{3680}{513}k_3 - \frac{845}{4104}k_4\right)\Delta t,\\
k_6 =& u\left(t^{(n)} + \frac{1}{2}\Delta t, x^{(n)} - \frac{8}{27}k_1 + 2k_2 - \frac{3544}{2565}k_3 + \frac{1859}{4104}k_4 - \frac{11}{40}k_5\right)\Delta t.
\end{aligned} \tag{A.49}$$

The solution to equation A.48 can then be obtained using a 4th order Runge-Kutta method

$$x^{(n+1)} = x^{(n)} + \frac{25}{216}k_1 + \frac{1408}{2565}k_3 + \frac{2197}{4101}k_4 - \frac{1}{5}k_5. \tag{A.50}$$

Another solution can be obtained using a 5th order Runge-Kutta method

$$\hat{x}^{(n+1)} = x^{(n)} + \frac{16}{135}k_1 + \frac{6656}{12825}k_3 + \frac{28561}{56430}k_4 - \frac{9}{50}k_5 + \frac{2}{55}k_6, \tag{A.51}$$

in order to obtain an estimate of the local truncation error.

The time step size Δt can then be controlled using the quantity

$$s = \left(\frac{\frac{1}{2}\epsilon}{\left|\hat{x}^{(n+1)} - x^{(n+1)}\right|} \right)^{\frac{1}{4}} \tag{A.52}$$

where ϵ is the specified error control tolerance on the time step size, and the denominator is the local truncation error estimate. If s is greater than 1.5, then the time step is doubled. If s is less than 0.75, the time step is halved. The error control tolerance used in all simulations was $\epsilon = 10^{-6}$.

A.9 Cell Metric Definitions

A.9.1 Taylor Deformation Parameter

A common measure of deformation used is the Taylor deformation parameter D_{12}, which is defined as

$$D_{12} = \frac{|l_1 - l_2|}{l_1 + l_2}, \tag{A.53}$$

where l_i denotes the semi-axis length in the ith direction of an ellipse with the same inertia tensor as the cell. The inertia tensor of the cell is defined as

$$\boldsymbol{I} = \int_S \rho \begin{bmatrix} x^2 & -xy \\ -xy & y^2 \end{bmatrix} dA = \rho \int_C \begin{bmatrix} \frac{1}{3}x^3 n_x & -\frac{1}{4}xy(xn_x + yn_y) \\ -\frac{1}{4}xy(xn_x + yn_y) & \frac{1}{3}y^3 n_y \end{bmatrix} dl, \tag{A.54}$$

where n_i is the ith component of the unit normal vector on the interface of the cell, and ρ is the density. The surface integral in equation A.54 has been converted to a line integral using the divergence theorem. The inertia tensor of an ellipse is given by

$$\begin{bmatrix} \frac{1}{4}\rho A l_1^2 & 0 \\ 0 & \frac{1}{4}\rho A l_2^2 \end{bmatrix} \tag{A.55}$$

The semi-axis lengths l_1, and l_2 can be calculated by finding the eigenvalues of the cell inertia tensor and equating them to the eigenvalues of the ellipse inertia tensor. The Taylor deformation parameter can then be calculated using Equation A.53.

A.9.2 Force on Tether

The force on the cell tether can be calculated using

$$\boldsymbol{F} = \int_C \Delta \boldsymbol{f}\, dl. \tag{A.56}$$

APPENDIX B

WALL-BOUNDED FLOW GREEN'S FUNCTIONS

B.1 Two-Dimensional Green's Function

The two-dimensional Green's function for a point source bounded by an infinite plane wall at $y = w$ is given by

$$\boldsymbol{G^W}(\boldsymbol{x}, \boldsymbol{x}_0) = \boldsymbol{G^{FS}}(\boldsymbol{x}, \boldsymbol{x_0}) - \boldsymbol{G^{FS}}(\boldsymbol{x}, \boldsymbol{x_0^{IM}}) \tag{B.1}$$

$$+ 2h_0^2 \boldsymbol{G^D}(\boldsymbol{x}, \boldsymbol{x_0^{IM}}) - 2h_0 \boldsymbol{G^{SD}}(\boldsymbol{x}, \boldsymbol{x_0^{IM}}), \tag{B.2}$$

where $h_0 = y_0 - w$, $\boldsymbol{x}_0^{IM} = (x_0, 2w - y_0)$, and $\boldsymbol{G^{FS}}$ is the free-space Green's function defined in equation A.8. The point $\boldsymbol{x}_0^{IM}$ is the image of the source point $\boldsymbol{x}_0$ with respect to the wall. The potential dipole $\boldsymbol{G^D}$ and the Stokeslet doublet $\boldsymbol{G^{SD}}$ are defined as

$$G_{ij}^D(\boldsymbol{x}, \boldsymbol{x_0}) = \pm \left(\frac{\delta_{ij}}{r^2} - 2\frac{\hat{x}_i \hat{x}_j}{r^4} \right), \tag{B.3}$$

$$G_{ij}^{SD}(\boldsymbol{x}, \boldsymbol{x_0}) = \hat{x}_2 G_{ij}^D(\boldsymbol{x}, \boldsymbol{x_0}) \pm \frac{\delta_{j2}\hat{x}_i - \delta_{i2}\hat{x}_j}{r^2}, \tag{B.4}$$

where $\hat{\boldsymbol{x}} = \boldsymbol{x} - \boldsymbol{x}_0$ and $r = |\hat{\boldsymbol{x}}|$. Equation B.3 and equation B.4 are positive for $j = 1$ and negative for $j = 2$.

The two-dimensional stress tensor is given by

$$\boldsymbol{T^W}(\boldsymbol{x}, \boldsymbol{x}_0) = \boldsymbol{T^{FS}}(\boldsymbol{x}, \boldsymbol{x_0}) - \boldsymbol{T^{FS}}(\boldsymbol{x}, \boldsymbol{x_0^{IM}}) \tag{B.5}$$

$$+ 2h_0^2 \boldsymbol{T^D}(\boldsymbol{x}, \boldsymbol{x_0^{IM}}) - 2h_0 \boldsymbol{T^{SD}}(\boldsymbol{x}, \boldsymbol{x_0^{IM}}), \tag{B.6}$$

where $\boldsymbol{T^{FS}}$ is the free-space stress tensor defined in equation A.9. The tensors $\boldsymbol{T^D}$ and $\boldsymbol{T^{SD}}$ are defined as

$$T_{ij}^D(\boldsymbol{x}, \boldsymbol{x_0}) = \frac{\partial G_{ij}^D}{\partial x_k} + \frac{\partial G_{kj}^D}{\partial x_i}, \tag{B.7}$$

$$T_{ij}^{SD}(\boldsymbol{x}, \boldsymbol{x_0}) = -2\delta_{ik}\frac{\hat{x}_j}{r^2} + \frac{\partial G_{ij}^{SD}}{\partial x_k} + \frac{\partial G_{kj}^{SD}}{\partial x_i}. \tag{B.8}$$

B.2 Three-Dimensional Green's Function

The three-dimensional Green's function for a point source bounded by an infinite plane wall at $y = w$ is given by

$$\boldsymbol{G^W}(\boldsymbol{x}, \boldsymbol{x}_0) = \boldsymbol{G^{FS}}(\boldsymbol{x}, \boldsymbol{x_0}) - \boldsymbol{G^{FS}}(\boldsymbol{x}, \boldsymbol{x_0^{IM}}) \tag{B.9}$$

$$+ 2h_0^2 \boldsymbol{G^D}(\boldsymbol{x}, \boldsymbol{x_0^{IM}}) - 2h_0 \boldsymbol{G^{SD}}(\boldsymbol{x}, \boldsymbol{x_0^{IM}}) \tag{B.10}$$

where $h_0 = y_0 - w$, $\boldsymbol{x}_0^{IM} = (x_0, 2w - y_0, z_0)$, and $\boldsymbol{G^{FS}}$ is the free-space Green's function defined in equation 3.11. The point $\boldsymbol{x}_0^{IM}$ is the image of the source point $\boldsymbol{x}_0$ with respect to the wall. The potential dipole $\boldsymbol{G^D}$ and the Stokeslet doublet $\boldsymbol{G^{SD}}$ are defined as

$$G_{ij}^D(\boldsymbol{x}, \boldsymbol{x_0}) = \pm \left(\frac{\delta_{ij}}{r^3} - 3\frac{\hat{x_i}\hat{x_j}}{r^5} \right) \tag{B.11}$$

$$G_{ij}^{SD}(\boldsymbol{x}, \boldsymbol{x_0}) = x_2 G_{ij}^D(\boldsymbol{x}, \boldsymbol{x_0}) \pm \frac{\delta_{j2}x_i - \delta_{i2}x_j}{r^3} \tag{B.12}$$

where $\hat{\boldsymbol{x}} = \boldsymbol{x} - \boldsymbol{x}_0$ and $r = |\hat{\boldsymbol{x}}|$. Equation B.3 and equation B.4 are positive for $j = 1$ and 3, and negative for $j = 2$.

The three-dimensional stress tensor is given by

$$\boldsymbol{T^W}(\boldsymbol{x}, \boldsymbol{x}_0) = \boldsymbol{T^{FS}}(\boldsymbol{x}, \boldsymbol{x_0}) - \boldsymbol{T^{FS}}(\boldsymbol{x}, \boldsymbol{x_0^{IM}}) \tag{B.13}$$

$$+ 2h_0^2 \boldsymbol{T^D}(\boldsymbol{x}, \boldsymbol{x_0^{IM}}) - 2h_0 \boldsymbol{T^{SD}}(\boldsymbol{x}, \boldsymbol{x_0^{IM}}), \tag{B.14}$$

where $\boldsymbol{T^{FS}}$ is the free-space stress tensor defined in equation A.9. The tensors $\boldsymbol{T^D}$ and $\boldsymbol{T^{SD}}$ are defined as

$$T_{ij}^D(\boldsymbol{x}, \boldsymbol{x_0}) = \pm \left(-\frac{\delta_{ik}x_j + \delta_{ij}x_k + \delta_{kj}x_i}{r^5} + 5\frac{x_i x_j x_k}{r^7} \right) \tag{B.15}$$

$$T_{ij}^{SD}(\boldsymbol{x}, \boldsymbol{x_0}) = x_2 T_{ijk}^D(\boldsymbol{x}, \boldsymbol{x_0}) \pm 6 \left(\frac{\delta_{ik}x_j x_2 - \delta_{j2}x_i x_k}{r^5} \right) \tag{B.16}$$

BIBLIOGRAPHY

Aarts, P., van den Broek, S., Prins, G., Kuiken, G., Sixma, J. & Heethaar, R. 1988 Blood platelets are concentrated near the wall and red blood cells in the center in flowing blood. *Arteriosclerosis, Thrombosis, and Vascular Biology* **8**, 819 824.

Abkarian, M., Faivre, M. & Viallat, A. 2007 Swinging of red blood cells under shear flow. *Physical Review Letters* **98** (18), 188302.

Abkarian, M. & Viallat, A. 2005 Dynamics of vesicles in a wall–bounded shear flow. *Biophysical Journal* **89**, 1055–1066.

Bagchi, P. 2007 Mesoscale simulation of blood flow in small vessels. *Biophysical Journal* **92** (6), 18581877.

Barthés-Biesel, D. 1980 Motion of a spherical microcapsule freely suspended in a linear shear-flow. *Journal of Fluid Mechanics* **100**, 831–853.

Barthés-Biesel, D., Diaz, A. & Dhenin, E. 2002 Effect of constitutive laws for two–dimensional membranes on flow–induced capsule deformation. *Journal of Fluid Mechanics* **460**, 211–222.

Barthés-Biesel, D. & Rallison, J. M. 1981 The time–dependent deformation of a capsule freely suspended in a linear shear flow. *Journal of Fluid Mechanics* **113**, 251–267.

Begent, N. & Born, G. 1970 Growth rate in vivo of platelet thrombi, produced by iontophoresis of ADP, as a function of mean blood flow velocity. *Nature* **227**, 926–930.

Bell, G. I. 1978 Models for the specific adhesion of cells to cells. *Science* **200** (4342), 618–627.

Berlin, C., Bargatze, R., Campbell, J., von Andrian, U., Szabo, M., Hasslen, S., Nelson, R., Berg, E., Erlandsen, S. & Butcher, E. 1995 $\alpha 4$ integrins mediate lymphocyte attachment and rolling under physiologic flow. *Cell* **80** (3), 413422.

Bhatia, S. K., King, M. R. & Hammer, D. A. 2003 The state diagram for cell adhesion mediated by two receptors. *Biophysical Journal* **84** (4), 2671–2690.

Bretherton, F. P. 1962 The motion of rigid particles in a shear flow at low Reynolds number. *Journal of Fluid Mechanics* **14** (2), 284–304.

Breyiannis, G. & Pozrikidis, C. 2000 Simple shear flow of suspensions of elastic capsules. *Theoretical and Computational Fluid Dynamics* **13**, 327–347.

Byars, S. 1999 Study points to role for nitric oxide in sickle cell anemia. http://clinicalcenter.nih.gov/about/news/newsletter/1999/nov99/index.html, accessed 23rd November, 2009.

Caputo, K. E. & Hammer, D. A. 2005 Effect of microvillus deformability on leukocyte adhesion explored using adhesive dynamics simulations. *Biophysical Journal* **89** (1), 187–200.

Caputo, K. E., Lee, D., King, M. R. & Hammer, D. A. 2007 Adhesive dynamics simulations of the shear threshold effect for leukocytes. *Biophysical Journal* **92** (3), 787–797.

Chaffey, C., Brenner, H. & Mason, S. 1967 Particle motions in sheared suspensions XXI I. Wall migration (theoretical). *Rheological Acta* **4**, 64–75.

Chan, P. C.-H. & Leal, L. G. 1979 The motion of a deformable drop in a second-order fluid. *Journal of Fluid Mechanics* **92** (131).

Chang, K. C., Tees, D. F. J. & Hammer, D. A. 2000 The state diagram for cell adhesion under flow: Leukocyte rolling and firm adhesion. *Proceedings of the National Academy of Sciences of the United States of America* **97** (21), 11262–11267.

Chang, K. S. & Olbricht, W. L. 1993 Experimental studies of the deformation and breakup of a synthetic capsule in steady and unsteady simple shear-flow. *Journal of Fluid Mechanics* **250**, 609–633.

Chapman, G. B. & Cokelet, G. R. 1996 Model studies of leukocyte-endothelium-blood interactions - the fluid flow drag force on the adherent leukocyte. *Biorheology* **33** (2), 119–138.

Chapman, G. B. & Cokelet, G. R. 1997 Model studies of leukocyte-endothelium-blood interactions. *Biorheology* **34** (1), 37–56.

Chapman, G. B. & Cokelet, G. R. 1998 Flow resistance and drag forces due to multiple adherent leukocytes in postcapillary vessels. *Biophysical Journal* **74** (6), 3292–3301.

Coulliette, C. & Pozrikidis, C. 1998 Motion of an array of drops through a cylindrical tube. *Journal of Fluid Mechanics* **358**, 1–28.

Cozens-Roberts, C., Lauffenburger, D. A. & Quinn, J. A. 1990 Receptor–mediated cell attachment and detachment kinetics. I. Probabilistic models and analysis. *Biophysical Journal* **58**, 841–856.

Crawford, N. & Taylor, D. G. 1977 Biochemical aspects of platelet behaviour. *British Medical Bulletin* **33** (3), 199–206.

Dembo, M., Torney, D. C., Saxman, K. & Hammer, D. 1988 The reaction–limited kinetics of membrane–to–surface adhesion and detachments. *Proceedings of the Royal Society of London Series B Biological Sciences* **234**, 55–83.

Diaz, A., Pelekasis, N. & Barthés-Biesel, D. 2000 Transient response of a capsule subjected to varying flow conditions: Effect of internal viscosity and membrane elasticity. *Physics of Fluids* **12** (5).

Doddi, S. K. & Bagchi, P. 2008 Lateral migration of a capsule in a plane Poisueille flow in a channel. *International Journal of Multiphase Flow* **34**, 966–986.

Doddi, S. K. & Bagchi, P. 2009 Three-dimensional computational modeling of multiple deformable cells flowing in microvessels. *Physical Review E* **79** (4), 046318.

Dong, C., Cao, J., Struble, E. J. & Lipowsky, H. H. 1999 Mechanics of leukocyte deformation and adhesion to endothelium in shear flow. *Annals of Biomedical Engineering* **27**, 298–312.

Dong, C. & Lei, X. X. 2000 Biomechanics of cell rolling: Shear flow, cell–surface adhesion and cell deformability. *Journal of Biomechanics* **33**, 35–43.

Dong, C. & Skalak, R. 1992 Leukocyte deformability - finite-element modeling of large viscoelastic deformation. *Journal of Theoretical Biology* **158** (2), 173–193.

Dopheide, S. M., Maxwell, M. J. & Jackson, S. P. 2002 Shear–dependent tether formation during platelet translocation on von Willebrand factor. *Blood* **99** (1), 159–167.

Drury, J. L. & Dembo, M. 1999 Hydrodynamics of micropipette aspiration. *Biophysical Journal* **76** (1), 110–128.

Dupin, M., I, H., Alboul, C. C. L. & Munn, L. 2007 Modeling the flow of dense suspensions of deformable particles in three dimensions. *Physical Review E* **75** (6), 066707.

Eggleton, C. D. & Popel, A. S. 1998 Large deformation of red blood cell ghosts in a simple shear flow. *Physics of Fluids* **10** (8), 1834–1845.

Evans, E., Heinrich, V., Leung, A. & Kinoshita, K. 2005 Nano- to microscale dynamics of P-selectin detachment from leukocyte interfaces. I. Membrane separation from cytoskeleton. *Biophysical Journal* **88**, 2288–2298.

Evans, E. & Yeung, A. 1989 Apparent viscosity and cortical tension of blood granulocytes determined by micropipet aspiration. *Biophysical Journal* **56** (1), 151–160.

Finger, E., Puri, K., Alon, R., Lawrence, M., von Andrian, U. & Springer, T. 1996 Adhesion through L-selectin requires a threshold hydrodynamic shear. *Nature* **379**, 266–269.

Fåhræus, R. 1929 The suspension stability of the blood. *Physiological Reviews* **9**, 241274.

Fåhræus, R. & Lindqvist, T. 1931 The viscosity of the blood in narrow capillary tubes. *American Journal of Physiology* **96**, 562568.

Fruend, J. B. 2007 Leukocyte margination in a model microvessel. *Physics of Fluids* **19** (023301).

Fung, Y., Tsang, W. & Patitucci, P. 1981 High-resolution data on the geometry of red blood cells. *Biorheology* **18**, 369385.

Gaver, D. P. & Kute, S. M. 1998 A theoretical model study of the influence of fluid stresses on a cell adhering to a microchannel wall. *Biophysical Journal* **75**, 721733.

Goldman, A. J., Cox, R. G. & Brenner, H. 1967 Slow viscous motion of a sphere parallel to a plane wall–II. Couette flow. *Chemical Engineering Science* **22**, 653–660.

Goldsmith, H., Cokelet, G. & Gaehtgens, P. 1989 Robin Fåhræus: Evolution of his concepts in cardiovascular physiology. *American Journal of Physiology Heart and Circulatory Physiology* **257** (3), H1005H1015.

Goldsmith, H. & Mason, S. G. 1962 The flow of suspensions through tubes. Part I. Single spheres, rods and disks. *Journal of Colloid Science* **17**, 448.

Goldsmith, H. & Mason, S. G. 1967 The microrheology of suspensions. *Rheology* **4** (85).

de Haas, K. H., Blom, C., van den Ende M. H. G. Duits, D. & Mellema, J. 1997 Deformation of giant lipid bilayer vesicles in shear flow. *Physical Review E* **56** (6), 7132–7137.

Haga, J. H., Beaudoin, A. J., White, J. G. & Strony, J. 1998 Quantification of the passive mechanical properties of the resting platelet. *Annals of Biomedical Engineering* **26** (2), 268277.

Hammer, D. A. & Apte, S. M. 1992 Simulation of cell rolling and adhesion on surfaces in shear flow: General results and analysis of selectin–mediated neutrophil adhesion. *Biophysical Journal* **63**, 35–56.

Heinrich, V., Leung, A. & Evans, E. 2005 Nano- to microscale dynamics of P-selectin detachment from leukocyte interfaces. II. Tether flow terminated by P-selectin dissociation from PSGL-1. *Biophysical Journal* **88**, 22992308.

Hochmuth, R., Evans, E., Wiles, H. & McCown, J. 1983 Mechanical measurement of red-cell membrane thickness. *Science* **220** (4592), 101102.

Hsu, R. & Secomb, T. 1989 Motion of nonaxisymmetric red-blood-cells in cylindrical capillaries. *Journal of Biomechanical Engineering-Transactions of the ASME* **111** (2), 147151.

Hwang, W. & Waugh, R. 1997 Energy of dissociation of lipid bilayer from the membrane skeleton of red blood cells. *Biophysical Journal* **72**, 26692678.

Jackson, S. 2007 The growing complexity of platelet aggregation. *Blood* **109**, 50875095.

Jadhav, S., Eggleton, C. D. & Konstantopoulos, K. 2005 A 3–D computational model predicts that cell deformation affects selectin–mediated leukocyte rolling. *Biophysical Journal* **88**, 96–104.

Jeffery, G. B. 1922 The motion of ellipsoidal particle immersed in a viscous fluid. *Proceedings of the Royal Society of London. Series A, Containing Papers of a Mathematical and Physical Character* **102** (715), 161–179.

Kan, H.-C., Shyy, W., Udaykumar, H. S., Vigneron, P. & Tran-Son-Tay, R. 1999*a* Effects of nucleus on leukocyte recovery. *Annals of Biomedical Engineering* **27** (5), 648–655.

Kan, H.-C., Shyy, W., Udaykumar, H. S., Vigneron, P. & Tran-Son-Tay, R. 1999*b* Numerical analysis of the deformation of an adherent drop under shear flow. *Journal of Biomechanical Engineering-Transactions of the ASME* **121** (2), 160–169.

Kan, H.-C., Udaykumar, H. S., Shyy, W. & Tran-Son-Tay, R. 1998 Hydrodynamics of a compound drop with application to leukocyte modeling. *Physics of Fluids* **10** (4), 760–774.

Kantsler, V. & Steinberg, V. 2005 Orientation and dynamics of a vesicle in tank-treading motion in shear flow. *Physical Review Letters* **95** (25), 258101.

Kantsler, V. & Steinberg, V. 2006 Transition to tumbling and two regimes of tumbling motion of a vesicle in shear flow. *Physical Review Letters* **96** (3), 036001.

Katnik, C. & Waugh, R. 1990 Alterations of the apparent area expansivity modulus of red blood cell membrane by electric fields. *Biophysical Journal* **57**, 877882.

Keller, S. & Skalak, R. 1982 Motion of a tank-treading ellipsoidal particle in a shear-flow. *Journal of Fluid Mechanics* **120**, 27.

Kessler, S., Finken, R. & Seifert, U. 2008 Swinging and tumbling of elastic capsules in shear flow. *Journal of Fluid Mechanics* **605**, 207–226.

Khismatullin, D. B. & Truskey, G. A. 2004 A 3D numerical study of the effect of channel height on leukocyte deformation and adhesion in parallel–plate flow chambers. *Microvascular Research* **68**, 188–202.

Khismatullin, D. B. & Truskey, G. E. 2005 Three–dimensional numerical simulation of receptor–mediated leukocyte adhesion to surfaces: Effects of cell deformability and viscoelasticity. *Physics of Fluids* **17** (3), 031505.

King, M. R. & Hammer, D. A. 2001*a* Multiparticle adhesive dynamics: Hydrodynamic recruitment of rolling leukocytes. *Proceedings of the National Academy of Sciences of the United States of America* **98**, 14919–14924.

King, M. R. & Hammer, D. A. 2001*b* Multiparticle adhesive dynamics. Interactions between stably rolling cells. *Biophysical Journal* **81**, 799–813.

King, M. R., Heinrich, V., Evans, E. & Hammer, D. A. 2005 Nano-to-micro scale dynamics of P-selectin detachment from leukocyte interfaces. III. Numerical simulation of tethering under flow. *Biophysical Journal* **88** (3), 1676–1683.

King, M. R., Rodgers, S. D. & Hammer, D. A. 2001 Hydrodynamic collisions suppress fluctuations in the rolling velocity of adhesive blood cells. *Langmuir: The ACS Journal of Surfaces and Colloids* **17** (14).

Korn, C. B. & Schwarz, U. S. 2008 Dynamic states of cells adhering in shear flow: From slipping to rolling. *Physical Review E* **77** (4), 041904.

Kroll, M. H., Hellums, J. D., McIntire, L. V., Schaefer, A. I. & Moake, J. L. 1996 Platelets and shear stress. *The Journal of the American Society of Hematology* **88** (5), 1525–1541.

Lac, E. & Barthés-Biesel, D. 2005 Deformation of a capsule in simple shear flow: Effect of membrane prestress. *Physics of Fluids* **17** (072105).

Lac, E. & Barthés-Biesel, D. 2008 Pairwise interaction of capsules in simple shear flow: Three-dimensional effects. *Physics of Fluids* **20** (4), 040801.

Lac, E., Barthés-Biesel, D., Pelekasis, N. A. & Tsamopoulos, J. 2004 Spherical capsules in three–dimensional unbounded Stokes flows: Effect of the membrane constitutive law and onset of buckling. *Journal of Fluid Mechanics* **516**, 303–334.

Lac, E., Morel, A. & Barthés-Biesel, D. 2007 Hydrodynamic interaction between two identical capsules in simple shear flow. *Journal of Fluid Mechanics* **573**, 149–169.

Lawrence, M., Kansas, G., Kunkel, E. & Ley, K. 1997 Threshold levels of fluid shear promote leukocyte adhesion through selectins (cd62l,p,e). *Journal of Cell Biology* **136** (3), 717727.

Lawrence, M. B. & Springer, T. A. 1991 Leukocytes roll on a selectin at physiological flow rates: Distinction from and prerequisite for adhesion through integrins. *Cell* **65**, 859–973.

Leal, L. G. 1980 Particle motions in a viscous fluid. *Annual Review of Fluid Mechanics* **12**, 435–476.

Leal, L. G. 1992 *Laminar Flow and Convective Transport Processes: Scaling Principles and Asymptotic Analysis*. Massachusetts, USA: Butterworth-Heinemann.

Leal, L. G. 2007 *Advanced Transport Phenomena*. Cambridge University Press.

Leal, L. G. & Lee, S. H. 1982 Particle motion near a deformable interface. *Advances in Colloid and Interface Science* **17**, 61–81.

Lee, S. H. & Leal, L. G. 1982 The motion of a sphere in the presence of a deformable interface II. A numerical study of the translation of a sphere normal to an interface. *Journal of Colloid and Interface Science* **87** (1), 81–106.

Lei, X. X., Lawrence, M. R. & Dong, C. 1999 Influence of cell deformation on leukocyte rolling adhesion in shear flow. *Journal of Biomechanical Engineering-Transactions of the ASME* **121**, 636–643.

Li, X. Z., Barthés-Biesel, D. & Helmy, A. 1988 Large deformations and burst of a capsule freely suspended in an elongational flow. *Journal of Fluid Mechanics* **187**, 179–196.

Liu, X. H. & Wang, X. 2004 The deformation of an adherent leukocyte under steady shear flow: A numerical study. *Journal of Biomechanics* **37** (7), 1079–1085.

Marshall, B. T., Long, M., Piper, J. W., Yago, T., McEver, R. P. & Zhu, C. 2003 Direct observation of catch bonds involving cell–adhesion molecules. *Nature* **423**, 190–193.

Mathews, J. H. & Fink, K. D. 1999 *Numerical methods using MATLAB*, chap. 9, p. 466. Prentice Hall.

Maxwell, M. J., Dopheide, S. M., Turner, S. J. & Jackson, S. P. 2006 Shear induces a unique series of morphological changes in translocating platelets: Effects of morphology on translocation dynamics. *Arteriosclerosis, Thrombosis and Vascular Biology* **26** (3), 663–669.

Melder, R., Yuan, J., Munn, L. & Jain, R. 2000 Erythrocytes enhance lymphocyte rolling and arrest in vivo. *Microvascular Research* **59**, 316.

Michelson, A. D. 2002 *Platelets*. Academic Press.

Misbah, C. 2006 Vacillating breathing and tumbling of vesicles under shear flow. *Physical Review Letters* **96** (2), 028104.

Mody, N. A. & King, M. R. 2005 Three–dimensional simulations of a platelet–shaped spheroid near a wall in shear flow. *Physics of Fluids* **17** (11), 3302–1–3302–12.

Mody, N. A. & King, M. R. 2007 Influence of brownian motion on blood platelet flow behavior and adhesive dynamics near a planar wall. *Langmuir* **23** (11), 6321–6328.

Mody, N. A. & King, M. R. 2008*a* Platelet adhesive dynamics. Part I: Characterization of platelet hydrodynamic collisions and wall effects. *Biophysical Journal* **95** (5), 2539–2555.

Mody, N. A. & King, M. R. 2008*b* Platelet adhesive dynamics. Part II: High shear-induced transient aggregation via GPIb alpha-vWF-GPIb alpha bridging. *Biophysical Journal* **95** (5), 2556–2574.

Mody, N. A., Lomakin, O., Doggett, T. A., Giacovo, T. G. & King, M. R. 2005 Mechanics of transient platelet adhesion to von Willebrand factor under flow. *Biophysical Journal* **88** (2), 1432–1443.

N'Dri, N. A., Shyy, W. & Tran-Son-Tay, R. 2003 Computational modeling of cell adhesion and movement using a continuum–kinetics approach. *Biophysical Journal* **85**, 2273–2286.

Needham, D. & Hochmuth, R. 1992 A sensitive measure of surface stress in the resting neutrophil. *Biophysical Journal* **61**, 16641670.

Nesbitt, W. S., Westein, E., Tovar-Lopez, F. J., Tolouei, E., Mitchell, A., Fu, J., Carberry, J., Fouras, A. & Jackson, S. P. 2009 A shear gradient-dependent platelet aggregation mechanism drives thrombus formation. *Nature Medicine* **15** (6), 665U146.

Olla, P. 1997*a* The lift on a tank-treading ellipsoidal cell in a shear flow. *Journal de Physique II* **30** (1), 317329.

Olla, P. 1997*b* The role of tank-treading motions in the transverse migration of a spheroidal vesicle in a shear flow. *Journal of Physics A - Mathematical and General* **7** (10), 15331540.

Pappu, V. & Bagchi, P. 2008 3D computational modeling and simulation of leukocyte rolling adhesion and deformation. *Computers in Biology and Medicine* **38** (6), 738–753.

Pappu, V., Doddi, S. K. & Bagchi, P. 2008 A computational study of leukocyte adhesion and its effect on flow pattern in microvessels. *Journal of Theoretical Biology* **254** (2), 483–498.

Pawar, P., Jadhav, S., Eggleton, C. D. & Konstantopoulos, K. 2008 Roles of cell and microvillus deformation and receptor-ligand binding kinetics in cell rolling. *American Journal of Physiology-Heart and Circulatory Physiology* **295** (4), H1439–H1450.

Peterson, D. & Bronzino, J., ed. 2008 *Biomechanics: Principles and Applications*. CRC Press.

Phibbs, R. 1966 Distribution of leukocytes in blood flowing through arteries. *American Journal of Physiology* **210**, 919.

Pozrikidis, C. 1990 The axisymmetric deformation of a red blood cell in uniaxial straining Stokes flow. *Journal of Fluid Mechanics* **216**, 231–254.

Pozrikidis, C. 1992 *Boundary Integral and Singularity Methods for Linearized Viscous Flow*. Cambridge, UK: Cambridge University Press.

Pozrikidis, C. 1995 Finite deformation of liquid capsules enclosed by elastic membranes in simple shear-flow. *Journal of Fluid Mechanics* **297**, 123–152.

Pozrikidis, C. 2001*a* Effect of membrane bending stiffness on the deformation of capsules in simple shear flow. *Journal of Fluid Mechanics* **440**, 269–291.

Pozrikidis, C. 2001*b* Interfacial dynamics for Stokes flow. *Journal of Computational Physics* **169**, 250–301.

Pozrikidis, C. 2002 *A Practical Guide to Boundary Element Methods with the Software Library BEMLIB*. Chapman & Hall/CRC.

Pozrikidis, C., ed. 2003*a* *Modeling and Simulation of Capsules and Biological Cells*. Francis & Taylor/CRC Press.

Pozrikidis, C. 2003*b* Numerical simulation of the flow-induced deformation of red blood cells. *Annals of Biomedical Engineering* **31**, 11941205.

Pozrikidis, C. 2005 Axisymmetric motion of a file of red blood cells through capillaries. *Physics of Fluids* **17** (3).

Pozrikidis, C. 2005*a* Computation of Stokes flow due to the motion or presence of a particle in a tube. *Annals of Biomedical Engineering* **53**.

Pozrikidis, C. 2005*b* Numerical simulation of cell motion in tube flow. *Annals of Biomedical Engineering* **33** (2).

Pozrikidis, C. 2005*c* Orbiting motion of a freely suspended spheroid near a plane wall. *Journal of Fluid Mechanics* **541**, 105–114.

Pozrikidis, C. 2006 Flipping of an adherent blood platelet over a substrate. *Journal of Fluid Mechanics* **568**, 161–172.

Ramachandran, V., Williams, M., Yago, T., Schmidtke, D. W. & McEver, R. P. 2004 Dynamics alterations of membrane tethers stabilize leukocyte rolling on P–selectin. *Proceedings of the National Academy of Sciences of the United States of America* **101** (37), 13519–13524.

Ramanujan, S. & Pozrikidis, C. 1998 Elastic capsules in shear flow. *Journal of Fluid Mechanics* **361**, 117–143.

Ratner, B. D., Hoffman, A. S., Schoen, F. J. & Lemons, J. E., ed. 1996 *Biomaterials science: An introduction to materials in medicine*. Elsevier Science.

Ross, P. & Minton, A. 1977 Hard quasispherical model for the viscosity of hemoglobin solutions. *Biochemical and Biophysical Research Communications* **76**, 971976.

Savage, B., Saldivar, E. & Ruggeri, Z. M. 1996 Initiation of platelet adhesion by arrest onto fibrinogen or translocation on von Willebrand factor. *Cell* **84**, 289–297.

Schmid-Schönbein, G. W., Sung, K. L., Tözeren, H., Skalak, R. & Chien, S. 1981 Passive mechanical properties of human leukocytes. *Biophysical Journal* **36** (1), 243–256.

Schmid-Schönbein, G. W., Usami, S., Skalak, R. & Chien, S. 1980 The interaction of leukocytes and erythrocytes in capillary and postcapillary vessels. *Microvascular Research* **19**, 4570.

Schmid-Schönbein, H. & Wells, R. 1969 Fluid drop-like transition of erythrocytes under shear. *Science* **165** (3890), 288–291.

Schmidtke, D. W. & Diamond, S. L. 2000 Direct observation of membrane tethers formed during neutrophil attachment to platelets or P–selectin under physiological flow. *Journal of Cell Biology* **149** (3), 719–729.

Secomb, T., Skalak, R., Ozkaya, N. & Gross, J. 1986 Flow of axisymmetrical red-blood-cells in narrow capillaries. *Journal of Fluid Mechanics* **163**, 405423.

Secomb, T. W. 1992 Red blood cell mechanics and capillary blood rheology. *Cell Biophysics* **18** (231).

Secomb, T. W., Styp-Rekowska, B. & Pries, A. R. 2007 Two-dimensional simulation of red blood cell deformation and lateral migration in microvessels. *Annals of Biomedical Engineering* **35** (5), 755–765.

Segre, G. & Silberberg, A. 1962*a* Behavior of macroscopic rigid spheres in Poiseuille flow part I. *Journal of Fluid Mechanics* **14** (1), 115–135.

Segre, G. & Silberberg, A. 1962*b* Behavior of macroscopic rigid spheres in Poiseuille flow part II. *Journal of Fluid Mechanics* **14** (1), 136–157.

Seifert, U. 1999 Fluid membranes in hydrodynamic flow fields: Formalism and an application to fluctuating quasispherical vesicles in shear flow. *European Physical Journal B* **8**, 405–415.

Shapira, M. & Haber, S. 1990 Low Reynolds number motion of a droplet in shear flow including wall effects. *International Journal of Multiphase Flow* **16** (305).

Singer, S. J. & Nicolson, G. L. 1972 Fluid mosaic model of structure of cell–membranes. *Science* **175** (4023), 720–731.

Singh, R. K. & Sarkar, K. 2009 Effects of viscosity ratio and three dimensional positioning on hydrodynamic interactions between two viscous drops in a shear flow at finite inertia. *Physics of Fluids* **21** (10), 103303.

Skalak, R., Özkaya, N. & Skalak, T. C. 1989 Biofluid mechanics. *Journal of Fluid Mechanics* **21**, 167204.

Skalak, R., Tozeren, A., Zarda, R. P. & Chien, S. 1973 Strain energy function of red blood cell membranes. *Biophysical Journal* **13**, 245–264.

Skotheim, J. M. & Secomb, T. W. 2007 Red blood cells and other nonspherical capsules in shear flow: Oscillatory dynamics and the tank-treading-to-tumbling transition. *Physical Review Letters* **98** (7), 078301.

Sukumaran, S. & Seifert, U. 2001 Influence of shear flow on vesicles near a wall: A numerical study. *Physical Review E* **64** (011916).

Sun, C., Migliorini, C. & Munn, L. 2003 Red blood cells initiate leukocyte rolling in postcapillary expansions: A lattice Boltzmann analysis. *Biophysical Journal* **85**, 208222.

Sun, C. & Munn, L. 2005 Particulate nature of blood determines macroscopic rheology: A 2D lattice Boltzmann analysis. *Biophysical Journal* **88**, 16351645.

Ting-Beall, H., Needham, D. & Hochmuth, R. 1993 Volume and osmotic properties of human neutrophils. *Blood* **81**, 27742780.

Tran-Son-Tay, R., Kan, H.-C., Udaykumar, H. S., Damay, E. & Shyy, W. 1998 Rheological modelling of leukocytes. *Medical & Biological Engineering & Computing* **36** (2), 246–250.

Uijttewaal, W. S. & Nijhof, E.-J. 1995 The motion of a droplet subjected to linear shear flow including the presence of a plane wall. *Journal of Fluid Mechanics* **302**, 45–63.

Uijttewaal, W. S., Nijhof, E.-J. & Heethaar, R. M. 1993 Droplet migration, deformation, and orientation in the presence of a plane wall: A numerical study compared with analytical theories. *Physics of Fluids A* **5**.

Vlahovska, P. M. & Gracia, R. S. 2007 Dynamics of a viscous vesicle in linear flows. *Physical Review E* **75**, 016313.

Wagner, D. D. & Frenette, P. S. 2008 The vessel wall and its interactions. *Blood* **111** (11).

Walter, A., Rehage, H. & Leonhard, H. 2001 Shear induced deformation of microcapsules: Shape oscillations and membrane folding. *Colloids and Surfaces A-Physicochemical and Engineering Aspects* **183** (Sp. Iss. SI), 123–132.

Waugh, R. & Evans, E. 1979 Thermoelasticity of red blood cell membrane. *Biophysical Journal* **26**, 115132.

Wetzel, B. & Schaefer, H. 1982 National Cancer Institute visuals online. http://visualsonline.cancer.gov/details.cfm?imageid=2129, accessed 23rd November, 2009.

White, J. G. & Rao, G. G. R. 1998 Microtubule coils versus the surface membrane cytoskeleton in maintenance and restoration of platelet discoid shape. *The American Journal of Pathology* **152** (2), 597–609.

Yap, B. & Kamm, R. 2005 Mechanical deformation of neutrophils into narrow channels induces pseudopod projection and changes in biomechanical properties. *Journal of Applied Physiology* **98**, 19301939.

Yeung, A. & Evans, E. 1989 Cortical shell-liquid core model for passive flow of liquid-like spherical cells into micropipets. *Biophysical Journal* **56** (1), 139–149.

Yu, Y. & Shao, J. Y. 2007 Simultaneous tether extraction contributes to neutrophil rolling stabilization: A model study. *Biophysical Journal* **92** (2), 418–429.

Yuan, Y., Kulkarni, S., Ulsemer, P., Cranmer, S. L., Yap, C. L., Nesbitt, W. S., Harper, I., Mistry, N., Dopheide, S. M., Hughan, S. C., Williamson, D., de la Salle, C., Salem, H. H., Lanza, F. & Jackson, S. P. 1999 The von Willebrand factor–glycoprotein Ib/V/IX interaction induces actin polymerization and cytoskeletal reorganization in rolling platelets and glycoprotein Ib/V/IX–transfected cells. *The Journal of Biological Chemistry* **274** (51), 36241–36251.

Zhang, J. F., Johnson, P. C. & Popel, A. S. 2007 An immersed boundary lattice Boltzmann approach to simulate deformable liquid capsules and its application to microscopic blood flows. *Physical Biology* **4** (4), 285–295.

Zhelev, D., Needham, D. & Hochmuth, R. 1994 Role of the membrane cortex in neutrophil deformation in small pipets. *Biophysical Journal* **67**, 696705.

Zhou, C., Yue, P. T. & Feng, J. J. 2008 Deformation of a compound drop through a contraction in a pressure-driven pipe flow. *International Journal of Multiphase Flow* **34** (1), 102–109.

Zhou, C. F., Yue, P. T. & Feng, J. J. 2007 Simulation of neutrophil deformation and transport in capillaries using Newtonian and viscoelastic drop models. *Annals of Biomedical Engineering* **35** (5), 766–780.

Zhou, H. & Pozrikidis, C. 1995 Deformation of liquid capsules with incompressible interfaces in simple shear-flow. *Journal of Fluid Mechanics* **283**, 175–200.

Zhu, C. 2000 Kinetics and mechanics of cell adhesion. *Journal of Biomechanics* **33** (1), 23–33.

Zinchenko, A. Z., Rother, M. A. & Davis, R. H. 1997 A novel boundary-integral algorithm for viscous interaction of deformable drops. *Physics of Fluids* **9**, 1493–1511.